Probing the Buckling of Thin-Shell Space Structures

Thesis by
Fabien Royer

In Partial Fulfillment of the Requirements for the
Degree of
Doctor of Philosophy in Space Engineering

CALIFORNIA INSTITUTE OF TECHNOLOGY
Pasadena, California

2021
Defended May 14, 2021

Fabien Royer
ORCID: 0000-0003-2452-2893

ACKNOWLEDGEMENTS

Many people at Caltech and around the world supported me during the completion of this work, and their help made this success possible. First and foremost, I would like to thank my advisor, Professor Sergio Pellegrino. If my life at Caltech could be modelled as a (nonlinear) thin-shell structure, Prof. Pellegrino managed to apply the right number of constraints while releasing enough degrees of freedom to make my experience isostatic, and therefore free of self-stress. From a less technical point of view, I am extremely thankful for his guidance, expertise and patience throughout my PhD. I know that I am not the most diplomatic student he has had, and I am grateful for his great support and for sharing his passion for research with me. I would also like to thank Professor John W. Hutchinson for his help, guidance and patience. Through the time he spent with me sharing his invaluable knowledge of thin shell structures, as well as his passion, he dramatically pushed my research forward. I would also like to thank the members of my candidacy and defense committees for their help and all the useful feedback they shared with me, Prof. Dan Meiron, Prof. Chiara Daraio, Prof. Ravi Ravichandran, and Prof. Soon-Jo Chung.

In addition to conducting my research work, I had the chance to be involved in The Space Solar Power Project. I really believe in the impact this project will have in the energy market of tomorrow, and I consider myself extremely lucky to have been able to work on this ambitious and visionary endeavour. I would like to thank all past and present members of this collaborative effort, particularly Prof. Harry Atwater and Prof. Ali Hajimiri. I would also like to acknowledge the financial support from Northrop Grumman and the Space Solar Power Project.

I would like to thank Tom Prince and everyone at the Keck Institute for Space Studies for welcoming me into their family and giving me the unique opportunity to see the Space scene from within. In addition, the Keck Institute for Space Studies financially supported my first year of studies and were instrumental in the creation and success of the Caltech Space Challenge. I want to give a special thank you to Michele Judd, who was one of my greatest supporter throughout my time at Caltech. I wish I would be as organized and efficient as she is at some point in my life.

I had the chance to be supported by multiple mentors throughout the years, that pushed me to become a better researcher, engineer, and person. Specifically, I would like to thank Dr. Gregory Davis, Dr. Daniel Scharf, Dr. Anthony Freeman and John

Baker for their invaluable advices during the AAReST project. I would like to thank Prof. Charles Elachi for his wisdom and support, even before applying to Caltech. I would like to acknowledge past and present members of the Space Structures Laboratory for their support. They are brilliant and are more than colleagues to me: Brayden Aller, Manan Arya, Miguel Bessa, Stephen Bongiorno, Federico Bosi, Gianfranco Canales, Luke Chen, Sahangi Dassanayake, Mélanie Delapierre, Charles Dorn, Serena Ferraro, Terry Gdoutos, Ashish Goel, Armanj Hasanyan, Christophe Leclerc, Andrew Lee, Yang Li, Wen Luo, Michael Marshall, John Pederson, Antonio Pedivellano, Harsha Reddy, Maria Sakovsky, Charles Sommer, Thibaud Talon, Daniel Turk, Alan Truong, Uba Kanthasamy Ubamanyu, Yuchen Wei and Alexander Wen. These people made going into the lab a celebration, and I wish we will stay friends for a very long time.

I had the chance to be the co-chair of the 2019 Caltech Space Challenge. I would like to thank the amazing Simon Toedtli with whom I have organized the event and shared this unforgettable experience, and our advisors Prof. Dan Meiron, Prof. Charles Elachi, Dr. Morgan Cable, our student experts Emile Oshima, Uba Kanthasamy Ubamanyu, Jean Sebastien Spratt, every past chair, everyone at Caltech and JPL who helped organizing this challenge, our sponsors, and of course, all the participants who made the event incredible.

Everyone at the Graduate Aerospace Laboratories (GALCIT) has been a great part of my experience at Caltech. I specifically want to thank Petros Arakelian, Kate Jackson, Peggy Blue, Jamie Sei and Christine Ramirez.

My time at Caltech wouldn't have been without the support from many friends: my colleagues during the first year in GALCIT; and all my adventure friends with who I had the chance to explore every corners of California. I have incredible memories of our crazy hikes and I am glad you were there to share them with me, and did not let me get lost in the desert. I will always be grateful to my parents, Benedicte and Pascal, who supported me since the very beginning, for pushing me to follow my passions, and for being always there for me. It is a big sacrifice for them to let me go so far away from home, but their unconditional support made my success possible. I will always be thankful to my brother Florian, with who I had some crazy experiences in the mountains and in the ocean. You push me to live my life to the fullest and I would always admire your free spirit and determination to make the world better, step by step. I want to thank my grandparents, Christian and Jacqueline, who are following closely my research and are providing me with

incredible support. And lastly, I would like to express my deepest gratitude to my better half, Sherry, who always encouraged me, and supported my grumpiness and frustration when my experiments were not working. Her support was invaluable, and I will always be thankful.

ABSTRACT

The overarching goal of the research presented in this dissertation is to apply and extend a newly developed methodology to understand the buckling of complex thin shell structures. This methodology enables the determination of tighter buckling criteria and paves the way to the development of more efficient structures, used closer than ever to their buckling load and even beyond. It would result in dramatically lighter structures to be built and has the potential to enable new applications, such as extremely large aperture satellites.

We first analyze the stability of open section thin shell structures under a pure bending moment, through simulations. These structures are composed of longitudinal thin-shell elements connected transversely by thin rods, and inspired by real spacecraft structures. The present study applies and extends recent work on the stability of cylindrical and spherical shells. The role of localization in the buckling of these structures is investigated and early transitions into the post-buckling regime are unveiled using a probe that locally displaces the structure. The probing method enables the computation of the energy input needed to transition early into a post-buckling state, which is central to determining the critical buckling mechanism for the structure. We show that the structure follows stability landscapes also found in cylindrical and spherical shell buckling problems. This initial computational study is the basis for the first ever probing experiment on a complex structure.

In order to test these new structures under bending, a new bending apparatus is designed and implemented. The boundary conditions are chosen such that the apparatus is statically determinate (isostatic), and no state of self stress can develop in the sample during its mounting and testing. This feature is especially desirable in the study of thin shell structures and their elastic instabilities, for which imperfection sensitivity plays a crucial role in the buckling transition and the post-buckling regime. The accuracy of the isostatic bending machine is first assessed through the testing of rods, and its imperfection insensitive behavior is then highlighted in experiments on tape springs, and through numerical studies of the same structures.

The new bending machine is complemented by a probing apparatus, and the stability of the open section thin-shell structures subjected to a pure bending moment is studied experimentally. The experiment confirms that localization of deformations plays a paramount role in the structure's nonlinear post-buckling regime and is

extremely sensitive to imperfections. This characteristic is investigated through probing experiments. The range of moments for which the early buckling of the structure can be triggered using this probe perturbation is determined, as well as the energy barrier separating the pre-buckling and post-buckling states. The stability of the local buckling mode is then illustrated by an experimental stability landscape of shell buckling, and probing is then extended to the entire structure to reveal alternate buckling modes disconnected from the structure's fundamental path. These results can be used to elaborate efficient buckling criteria for this type of structures, through the use of transition diagrams determined experimentally.

Finally, the buckling and post-buckling behavior of ultralight ladder-type coilable structures is investigated. These specific structures are used in the Space Solar Power Project at Caltech and are referred to as strips. Similarly to the previous studies, the stability of strip structures loaded by normal pressure is computationally studied by applying controlled perturbations through localized probing. The probing technique is generalized to higher-order bifurcations along the post-buckling path, and low-energy escape paths into buckling that cannot be predicted by a classical eigenvalue formulation are identified. It is shown that the stability landscape for a pressure-loaded strip is similar to the landscape for classical shells, and the open section thin shell structure studied initially in this thesis. While classical shell structures buckle catastrophically, strip structures feature a large stable post-buckling range. Probing enables the full characterization of the structure's unstable behavior, which paves the way to extend its operation closer than ever to the buckling load, and even in the post-buckling regime. It would enable the design of more efficient structures by dramatically reducing their mass, therefore enabling new large spacecraft to be built.

PUBLISHED CONTENT AND CONTRIBUTIONS

[1] F. Royer, J. W. Hutchinson, and S. Pellegrino. "Probing the Stability of Thin Shell Structures Under Bending". (in preparation). *F. Royer conducted the research, and wrote the manuscript.*

[2] F. Royer and S. Pellegrino. "Buckling Sensitivity of Ultralight Ladder-Type Coilable Space Structures". (submitted). *F. Royer conducted the research, and wrote the manuscript.*

[3] F. Royer and S. Pellegrino. "Experimental Probing of the Buckling of Thin Shell Structures Under Pure Bending". (in preparation). *F. Royer conducted the research, and wrote the manuscript.*

[4] F. Royer et al. "Isostatic Pure Bending Machine for the Testing of Imperfection Sensitive Non-Linear Structures". (in preparation). *F. Royer designed and analyzed the bending machine (simulations and experiments), and wrote the manuscript.*

[5] F. Royer and S. Pellegrino. "Buckling of Ultralight Ladder-type Coilable Space Structures". In: *AIAA Scitech Forum* (2020). *F. Royer conducted the research, and wrote the manuscript.* DOI: 10.2514/6.2020-1437.

[6] F. Royer and S. Pellegrino. "Ultralight Ladder-type Coilable Space Structures". In: *AIAA Spacecraft Structures Conference* (2018). *F. Royer conducted the research, and wrote the manuscript.* DOI: 10.2514/6.2018-1200.

TABLE OF CONTENTS

Chapter 1

INTRODUCTION

1.1 Motivation

Shell structures are ubiquitous in nature and in engineering applications. From egg shells to large structural architectures, their high load bearing capabilities and very low mass, make them some of the most efficient structural components available. Most of their stiffness is derived from geometry, rather than material and thickness. Thin shells have been instrumental in the development of aerospace applications and vehicles throughout the twentieth century, where the reduction of structural mass is paramount. They are the main components of airplane fuselages and rockets. In some cases, a complex balance of membrane forces allows their thickness to be reduced dramatically. It is for instance the case of the pressurized main fuel tank of the Space Shuttle which featured a shell thickness of 2.5 mm at its thinnest, or the fuselage of a Boeing 757, as thin as 0.99 mm.

In the past decade, the field of satellite structures witnessed a growing use of thin shells, as they enable large deployable structures to be built. They allow for the extremely efficient packaging of large systems which would be impossible to launch otherwise. These recent advances have been fostered by the development of deployable booms, for which the cross-section can be elastically deformed, flattened, and rolled into a tight volume. They are often used to deploy and support large aperture systems such as antennas, photovoltaic cells, and large membranes used in solar sails. Examples of such spacecraft designs are shown in Figure 1.1. The low magnitude of loading encountered in space enables designs in which the shell thickness is dramatically decreased [50].

In the Space Solar Power Project (SSPP) conducted at Caltech, new spacecraft architectures capable of collecting sunlight, converting it into microwaves, and sending it back to Earth are developed. These new designs depart significantly from previous large area deployable structures in which a membrane is tensioned by deployable booms. In the SSPP design, thin shell longerons form bending-stiff strips, which provide a support for functional elements [3]. Many of these strips are assembled to form a large square structure measuring up to 60 m $\times$ 60 m. The longerons are open cross-section components inspired by previously developed

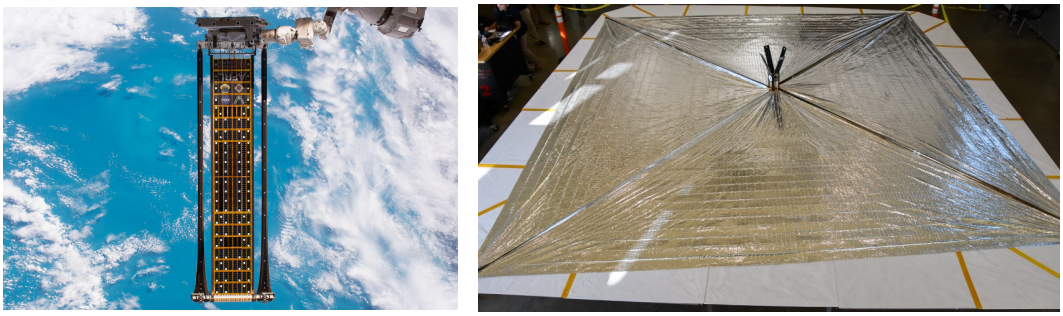

(a) (b)

Figure 1.1: (a) Roll-Out Solar Array (ROSA), deployed outside the International Space Station in 2019 (Credit: NASA). Two thin shell deployable booms (in black) are used to deploy and tension a photovoltaic blanket. (b) Lightsail 2 spacecraft successfully launched in 2015 (Credit: The Planetary Society).

deployable booms and their thickness ranges from 50 μm to 100 μm. They enable the entire structure to be flattened, coiled and deployed using the longerons's stored strain energy [18]. The SSPP concept and a small scale prototype are shown in Figure 1.2.

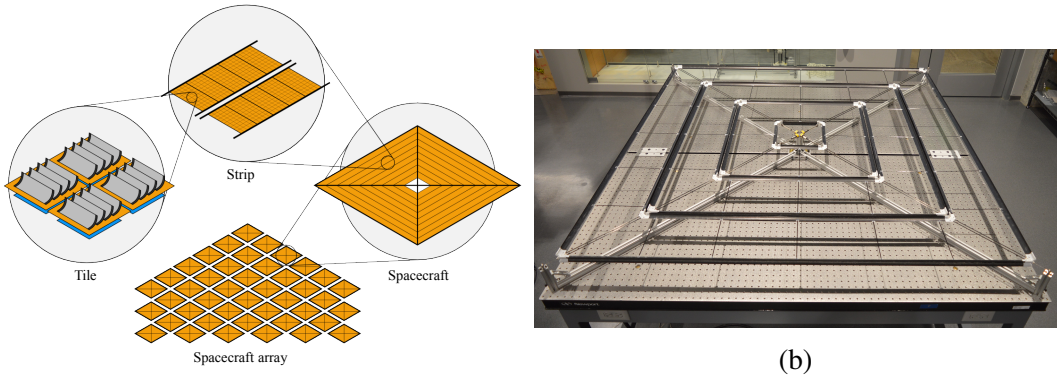

(a) (b)

Figure 1.2: (a) Space Solar Power Project architecture overview [3] and (b) 2 m prototype of a module, composed of deployable strips [19].

In most cases, increasing the size of the structure also increases its capabilities, which for SSPP is crucial to make the concept economically viable. However, the range of operations for thin shell structures is most of the time bounded by buckling. As thin shell components become lighter and thinner, predicting the load at which a structure will buckle becomes more and more challenging, as the stochastic nature of the instability is exacerbated. Therefore using structures close to their buckling load is often deemed unsafe. In this thesis, we explore the use of a newly developed

method, probing, to characterize the buckling of complex thin shell structures. Increasing the knowledge of the structure's behavior close to buckling, paves the way to the design of safer and more efficient structures, by using tighter buckling criteria, tailored to specific applications.

1.2 Thin shell buckling

This section aims to present a short review of the large body of work on thin shell buckling. Here, we only focus on the background necessary to understand the broader goal of the dissertation. Thorough reviews can be found in literature [12, 39, 43, 74], and each chapter introduction provides additional literature review on specific aspects of shell buckling. Throughout the twentieth century, the rapid development of planes and rockets motivated extensive studies of cylindrical and spherical shells, and their buckling behavior. Early experiments showed that these shells were failing earlier than their theoretical linear buckling load, with experimental buckling loads as low as 20% of their theoretical counterparts. In 1941, pioneer work by Von Kármán and Tsien at GALCIT showed that there exists a very unstable falling post-buckling path (sub-critical) starting at the bifurcation point, and that this path eventually restabilizes at dramatically lower loads [82]. They attributed the discrepancy between theoretical and experimental buckling loads to the presence of initial imperfections in the structure. In 1950, Donnell and Wan conducted experiments on cylindrical shells with known dominant imperfections and confirmed this hypothesis [13]. The post-buckling paths for the perfect and imperfect shell are shown in Figure 1.3a. In the Netherlands in 1945, Koiter theorized the role imperfections play in the buckling behavior, in his doctoral thesis [44]. Based on an analysis of the structure's total potential energy, he showed that a geometric imperfection taking the shape of the first buckling eigenvector can lead to dramatically reduced buckling loads, and his results are summarized in Figure 1.3b. He also provided an approximation of the falling post-buckling path. Later, Babcock [6] reconciled theory and experiments on buckling of cylindrical shells through the use of exceedingly closely toleranced shells obtained by an electroplating process, as well as the control of the shell's boundary conditions.

In practice, the design of compressed cylindrical shells used in rockets, for instance, relies heavily on the so-called knockdown-factor method. It accounts for the effect of imperfections in the shell's initial geometry. It provides a lower bound on the statistical load reduction observed in a large number of experiments, for various shell radii to thickness ratios. The widely used NASA SP-8007 [62] knockdown

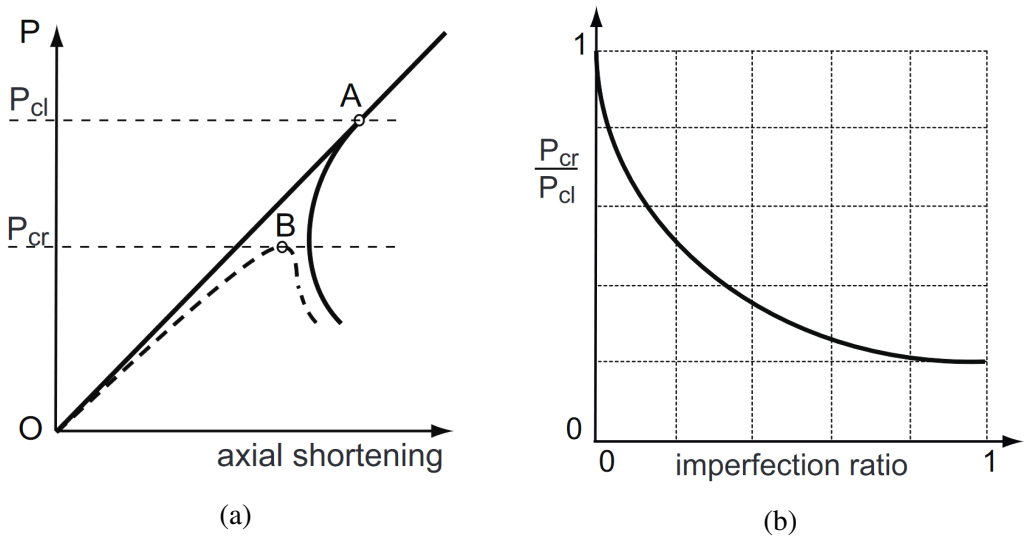

(a) (b)

Figure 1.3: Figures taken from [58]. (a) Sketch of the pre- and post-buckling paths for a perfect (solid line, from [82]) and imperfect (dashed line, from [13]) cylindrical shell under compression. (b) Sketch of the influence of an initial imperfection on the buckling load, from [44]. The imperfection ratio corresponds here to the imperfection amplitude divided by the shell thickness.

factor is presented in Figure 1.4. Even if this method proved to yield safe designs for cylindrical shells, it is now seen as very conservative since it takes into account the most severe type of imperfection, and was derived for steel shells. The use of new materials, precise manufacturing techniques and well characterized boundary conditions required an update of the NASA standard knockdown factor. In particular, the recent development in the Shell Buckling Knockdown Factor (SBKF) project aims to develop more efficient buckling criteria, in phase with today's advances in shell structures [29].

Another complication arising in thin shells is the localization of buckling deformations. After the bifurcation point is exceeded, the deformed shape observed on the post-buckling path is most of the time different from the buckling eigenmodes, and features highly localized deformations. This is the result of a highly non-linear process in which the structure's real imperfections bias the structure to form buckles at specific locations. This phenomenon has been observed and thoroughly studied for the compressed cylindrical shell [36] as well as the spherical shell under pressure [38]. The nature of localization itself generates a large number of post-buckling solutions, often referred to as spatial chaos [80]. A more complete review and analysis of localization is provided in section 2.1, and throughout the thesis.

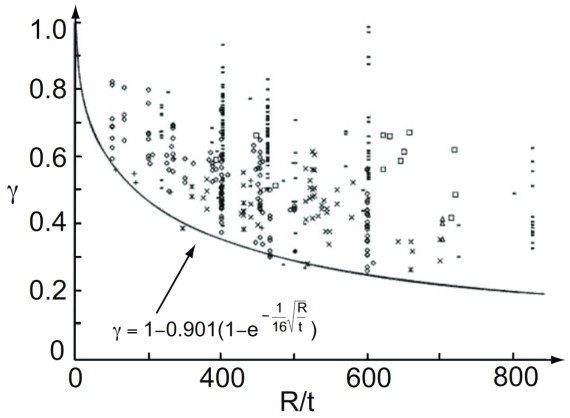

Figure 1.4: Figures taken from [58]. Lower bound used by NASA on experimental knockdown factor, as a function of the cylindrical shell radius to thickness ratio [43].

In recent years, an experimental methodology has been developed to characterize the onset of buckling, and offers a new way to establish buckling criteria for thin shell structures. This new methodology, referred to here as probing, is described next.

1.3 Probing methodology

Recent work on thin cylindrical and spherical shells has focused on the stability of the buckling phenomenon and its sensitivity to disturbances. Rather than seeing buckling purely as a bifurcation problem, these new contributions have studied in more detail the meta-stability of the structure's unbuckled path and the early transition into adjacent post-buckling paths requiring a small energy barrier to be overcome [41, 75, 79]. It has been shown recently, for the cylindrical shell, that the onset of buckling corresponds to the formation of a single dimple in the structure [32]. The single dimple can evolve to more and more complex post-buckling deformations through a series of destabilizations and restabilizations, until the cylinder is fully populated by dimples [23, 45]. The goal of the probing methodology is to characterize the formation of this single dimple by locally displacing the shell using a probe. Such experiments have been realized for the cylindrical [81] and spherical [53] shells and are described in Figure 1.5a-b. Plotting the reaction force as a function of the probe displacement and main loading forms a stability landscape of shell buckling, which describes the single dimple behavior close to buckling. Such a stability landscape is sketched in Figure 1.5c. Its features are described in details in Chapter 2 and Chapter 5. The landscape reveals that the single dimple can be formed earlier than the buckling load if a small amount of energy is brought to the

system as a perturbation. This energy barrier is sketched in Figure 1.5d. Most importantly, it has been shown that the load at which the dimple can first be found in equilibrium in the structure provides an excellent lower bound to experimental buckling loads. Therefore the methodology provides a unique opportunity to derive tighter buckling criteria [20]. In addition, the experimental method is non destructive and can therefore be applied to the final structure, without having to conduct statistical studies on a large number of test articles.

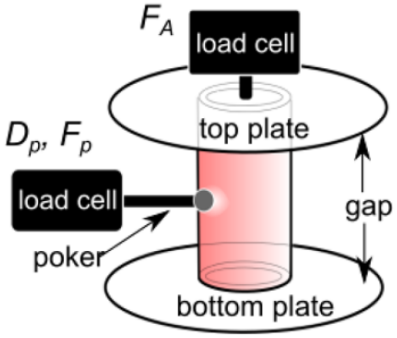

(a)

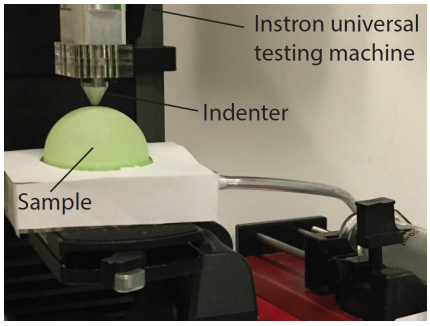

(b)

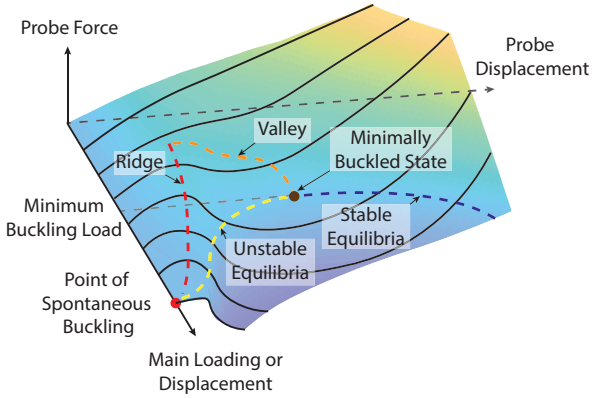

(c)

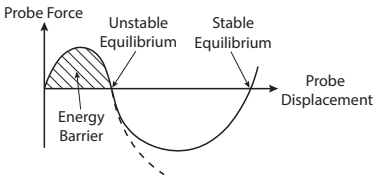

(d)

Figure 1.5: (a) Probing experiment on compressed soda cans, taken from [81]. (b) Probing experiment on pressurized hemispheres, taken from [53]. (c) Schematic of thin-shell buckling stability landscape, inspired from [81]. (d) Energy barrier formed between pre-buckled and post-buckled state, at a given level of loading.

1.4 Research objective and outline

The overarching goal of the research presented in this dissertation is to apply and extend the newly developed probing methodology to complex thin shell structures. While the original probing experiments showed great promises, their scope was

restricted to canonical problems and they suffered limitations when tackling practical engineering applications. The present work aims to push the probing methodology into the realm of real engineering structures and their design process. In particular, probing is applied to open section thin shell assemblies, subjected to bending. These structures are similar to the spacecraft components used in the Space Solar Power Project at Caltech. Probing is used to unveil new buckling phenomena specific to these structures, and shows that it can efficiently characterize their unpredictable buckling mechanisms. Throughout the dissertation, we thus demonstrate that the probing methodology can be harnessed to bring order into the stochastic nature of shell buckling, and can yield tighter and more deterministic buckling criteria. It provides the opportunity to develop more efficient structures, used closer than ever to their buckling load and even beyond. It would result in dramatically lighter structures and has the potential to enable new applications, such as extremely large aperture satellites. Professor Pedro Reis highlighted recently that structural instabilities can be harnessed to create new functionalities in mechanisms and meta-materials, and talked about a shift in thinking, "from buckliphobia to buckliphilia" [67]. Our hope is to slowly be able to shift the field of spacecraft structures towards buckliphilia as well.

The dissertation consists of six chapters. After the introduction, Chapter 2 presents probing simulations for an open section thin shell assembly, inspired by real spacecraft structures. Buckling localization is unveiled, and probing is used to identify critical buckling modes arising from spatial chaos. Simulations highlight that even if these structures and their loading are very different from the compressed cylindrical shell and the pressurized spherical shell, their buckling follows a similar stability landscape. The methodology is then extended to multiple probe locations and directions, and reveals buckling phenomena that have never been observed before. This computational analysis proves that probing is a powerful tool for the study of such structures.

Motivated by the findings of Chapter 2, a probing experiment for the open section thin shell structure is envisioned. However, it requires the design of a new bending apparatus suitable for the testing of extremely imperfection-sensitive structures. Chapter 3 presents the design and implementation of such a machine. It employs a set of air bearings and counterweights to provide statically determinate support conditions to the test structure, therefore guaranteeing that no self-stress can develop during testing. The new bending machine is realized and validated using tests

on linear and nonlinear structures. It is the first isostatic bending apparatus ever developed, and the only one able to applying strict pure bending conditions in a structure of arbitrary geometry.

Chapter 4 presents probing experiments enabled by the newly developed bending machine. A probing apparatus is added to the bending machine, and the behavior of a similar structure to the one in Chapter 1 is in investigated. Probing revealed that many localized buckled configurations can be found in the structure before the buckling load is attained. Experimental stability landscapes as well as transition diagrams are created to characterize the pre-buckling meta-stability and the competition between main and alternate buckling modes in the post-buckling regime.

The computational work of Chapter 2 and the experimental work of Chapter 4 reinforce our confidence in the use of probing in real engineering problems. Chapter 5 focuses on probing simulations for such a problem, the ultralight ladder-type coilable space structure under pressure loading. The structure features a long and stable post-buckling regime which can be utilized on orbit. Probing and its associated stability landscapes are used in the post-buckling regime to identify key paths and characteristics of the structure, such as the maximum post-buckling pressure. Sensitivity to geometric imperfections and the structure's size is also investigated. The simulations establish that probing can dramatically improve our understanding of such structures, and that the results found for the cylindrical and spherical shells can be extended to complex problems. Finally, Chapter 6 concludes the dissertation and discusses promising research directions.

The chapters in this dissertation (excluding 1 and 6) are research articles in preparation for submission. As such, they can be read independently from each other and are self-contained. Each chapter introduces the basis for the work presented in it, and gives the necessary technical background and literature review. Since these four publications are part of one single research effort, some necessary information is repeated between the chapter introductions and conclusions.

Chapter 2

THIN-SHELL STRUCTURES UNDER BENDING: COMPUTATIONAL STUDY

2.1 Introduction

Thin-shell structures are used extensively in engineering applications. In the aerospace sector, they are enabling light weight air and space vehicles to be built. While their use dramatically reduces the structural mass, their mode of failure is often governed by buckling, which is hard to predict. Buckling of thin-shell structures is characterized by a sub-critical bifurcation, which means that the structure exhibits a falling unstable post-buckling path right after the bifurcation point is reached. This sudden drop in load-carrying capabilities leads to a dramatic collapse if the post-buckling path never regains stability. Buckling is to be avoided at all cost in these cases. However, in recent adaptive structures and materials, buckling is no longer seen as failure but as a key shape-changing mechanism, which enables switching among multiple functional configurations [33, 54]. Whether buckling is used or to be avoided, understanding its cause and predicting its occurrence is crucial, and this has been the subject of numerous research studies over the past one hundred years. From the early 1920s, many shell buckling experiments were conducted, and experimental buckling loads were consistently observed to be lower than linearized classical buckling predictions. This discrepancy was later linked to the presence of initial imperfections in the shell geometry [13, 44, 82]. Indeed, for sub-critical bifurcations, there exists a range of loading for which the structure's fundamental (unbuckled) state is meta-stable, which makes the transition into post-buckling extremely sensitive to imperfections and disturbances. On the upside, this can also offer opportunities to build complex meta-stable structures [88] by using buckled thin-shells as the main building blocks. In order to deal with the extremely sensitive behavior of buckling in engineering applications, the design process thus relies heavily on buckling knockdown factors applied to the classical buckling load. Determining the adequate knockdown factor, unique for each structure/load combination, is of utter importance. It led to the NASA space vehicle design criteria for the buckling of thin-walled circular cylinders (NASA SP-8007) [62]. These criteria, widely seen as very conservative, are now being revisited by NASA's Shell Buckling Knockdown Factor (SBKF) Project established in 2007, which focuses

on testing shells with known imperfections and non-uniformities in loading and boundary conditions [29]. It has been shown that knowing accurately the structure's initial geometry enables the accurate prediction of the buckling event [51]. However, in many applications, measuring the shape of the structure before use can be both expensive and in some cases impossible, and the traditional buckling and post-buckling predictions rely on seeding a linear combination of the first buckling modes as imperfections [66, 68].

Another complication arising from unstable bifurcations is the localization of buckling deformations. This is observed for instance for beams on elastic foundations [83] but more importantly for thin-shell structures such as the compressed cylindrical shell [36] as well as the spherical shell under pressure [38]. The nature of localization itself generates a large number of post-buckling solutions even for a small set of classical buckling modes, since the deformations can localize at many different locations on the structure. This is referred to as spatial chaos [80]. Localization can arise on post-buckling branches determined by the buckling modes, as observed in the spherical shell under pressure [4, 40]. In addition, localization can also appear on post-buckling paths disconnected from the fundamental path while running asymptotically close to it [23].In both cases, localized buckling can be triggered earlier than the first buckling load if a small amount of energy is input into the structure. It has been shown, for the compressed cylindrical shell, that a single localized dimple forming in the middle of the structure constitutes the lowest escape into buckling [32] and may therefore be the critical buckling mechanism. This mode is not a bifurcation per se, but rather a mode "broken away" from the fundamental path. The single dimple state sits on a ridge in the total energy of the system between the pre-buckling well and local post-buckling well and corresponds to the lowest mountain pass between these two states in the energy landscape [32]. For the cylinder, the single dimple can evolve to more and more complex post-buckling deformations through a series of destabilizations and restabilizations, until the cylinder is fully populated by dimples [23, 45]. This process is called snaking and adds additional complexity to the full post-buckling sequence resolution.

For all the reasons mentioned above, predicting buckling is extremely difficult for shell structures and often relies on a case by case approach. Recent work has focused on the sensitivity of the buckling phenomenon to disturbances in thin cylindrical and spherical shells. A non-destructive experimental method has been proposed in 2013 to study the meta-stability of the fundamental path. It focuses on

determining the energy barrier separating the fundamental path and critical localized post-buckling states [41, 75, 79]. The search for the critical buckling mechanism is carried out by imposing a local radial displacement in the middle of the structure using a probe. This method effectively quantifies the resistance of shell buckling against the single dimple mode mentioned earlier. The method has been successfully applied to cylindrical shells [81] and to pressurized hemispherical shells [53]. These experiments quantified in particular the onset of meta-stability, often referred to as "shock sensitivity" [76] and a comparison with historical test data has shown that this specific loading can serve as an accurate lower bound for experimental buckling loads [20, 23].

In this chapter, we wish to apply these recent breakthroughs to more complex thin-shell structures, inspired by recent advances in spacecraft design which use thin-shell components to build large space systems. In particular, we are currently investigating structural architectures for ultralight, coilable space structures suitable for large, deployable, flat spacecrafts [3, 22] in the Space-based Solar Power Project (SSPP) at Caltech. In the deployed configuration, each spacecraft measures up to 60 m $\times$ 60 m in size and is loaded by solar pressure. The main building block is a ladder-type structure made of two triangular rollable and collapsible (TRAC) [57] longerons, connected transversely by rods (battens). This structure is shown in Figure 2.1 and scaled laboratory prototypes have been built [18, 19]. Previous analysis showed that local buckling plays a key role in the structural behavior [69] and motivates the need to conduct experimental buckling characterization. However, the size of the structure together with the complexity of its components and the peculiarity of its non-uniform bending moment, makes experiments very challenging. In order to address these limitations, the behavior of a simpler structure under pure bending is studied. This new structure is shown in Figure 2.2, and is made of longerons and battens like the previously described structure, but the longeron's TRAC cross-section is abandoned for an open-circular cross-section. While the structure and loading are different, it enables us to draw more general conclusions on the buckling of structures with thin-shell open cross-sections. The computational analysis presented here investigates the buckling behavior of such a structure and assesses if and when early transitions into post-buckling can occur, using the novel probing methodology. It also serves as a proof of concept for the experiment of Chapter 4.

The chapter is structured as follows. Section 2.2 describes in more detail the

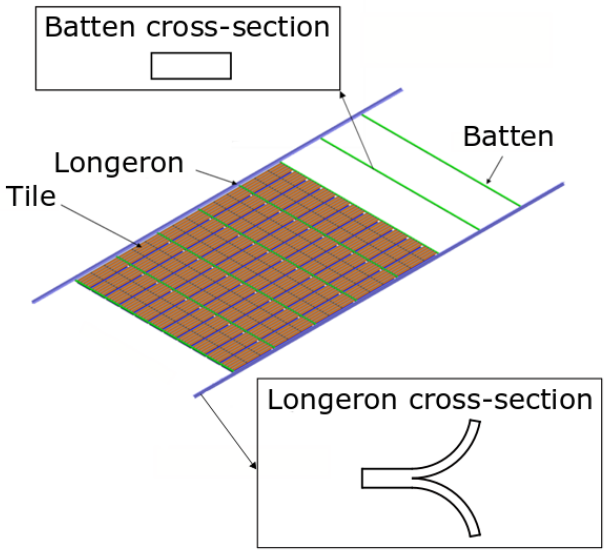

Figure 2.1: Schematic of the Space Solar Power Project strip structure. It is made of two thin-shell longerons connected with transverse battens, that support many functional tiles.

structure and the problem. Following a classical buckling analysis, Section 2.3 highlights the importance of localization and spatial chaos and justifies the use of the newly introduced probing methodology. In Section 2.4, probing is applied along the entire structure to determine the location at which local buckling can appear, and a critical probing scheme is identified. The analysis is then generalized in Section 2.5 to more complex probing scenarios exhibiting instabilities, and leads to an energy map from which the critical buckling mechanism is identified. Finally a stability landscape of shell buckling is computed in Section 2.6, highlights key characteristics of the critical buckling mechanism and shows excellent qualitative agreement with landscapes previously constructed.

2.2 Computational model

Geometry and material

For this chapter, the analysis is restricted to a single geometry, shown in Figure 2.2. The dimensions have been chosen on the basis of the experiment of Chapter 4, and allow for testing to be possible with the available experimental apparatus. The structure is composed of two thin-shell longerons of length 0.4 m. The longeron cross-section consists of a circular arc. The opening angle is 60 deg, the arc radius is 10 mm, and the shell thickness is 0.1 mm, which gives a bending stiffness comparable to the one obtained for the spacercraft structure's TRAC cross-section.

The two longerons are connected with 6 regularly spaced transverse circular rods called battens. The batten spacing is 80 mm and ensures that a significant amount of battens are connecting the two longerons as in the spacecraft structure. The batten length is 50 mm, and the batten cross-section radius is 1 mm. A finite element model of the structure is built using the Abaqus commercial software. The longerons are modeled with 4 node reduced integration shell elements (S4R) and the battens with linear 3D beam elements (B31). The mesh is structured with 2 mm elements. The element size is refined until convergence in the buckling eigenmodes and eigenvalues, shown in Figure 2.4, is achieved. The mesh density was also proven to be sufficient to resolve the localization process, discussed in Section 2.3. We consider an isotropic material of Young's modulus E = 130 GPa, and Poisson's ratio ν = 0.35 for both battens and longerons. For the rest of the chapter, this structure is referred to as a strip.

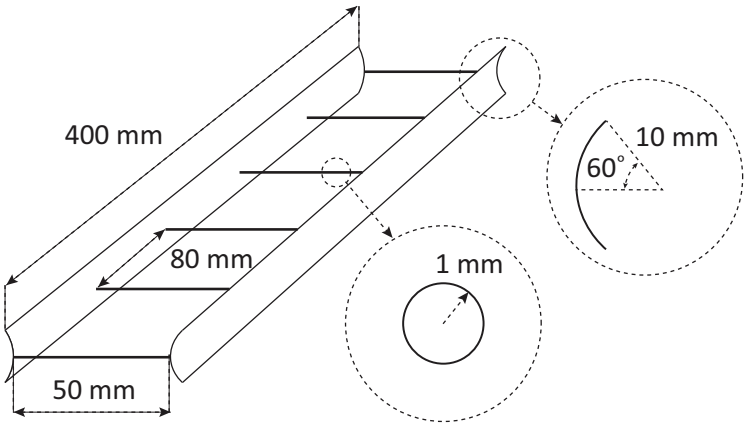

Figure 2.2: Structure composed of two thin-shell longerons connected transversely by battens. This structure is referred to as a strip.

Finite element analysis

The structure's end battens and the longeron end cross-sections are made undeformable and coupled to a reference point at each end on which the boundary conditions and the main loading are applied. A sketch of the problem is shown in Figure 2.3. The structure is simply supported at both ends: one reference point is pinned (all translations blocked) at one end while the Z translation is allowed for the reference point at the other end. Two equal and opposite moments of magnitude M are applied at both reference points, and an arc-length solver (Riks solver in Abaqus standard) is used to statically deform the structure and extract the overall moment/rotation curve. In addition, in Section 2.4, for each value of moment, we

probe the top edge of the longeron by applying a transverse nodal displacement U_x at location Z, and we extract the probe reaction force. Our two control parameters in each calculation are thus the end moment and the probe displacement.

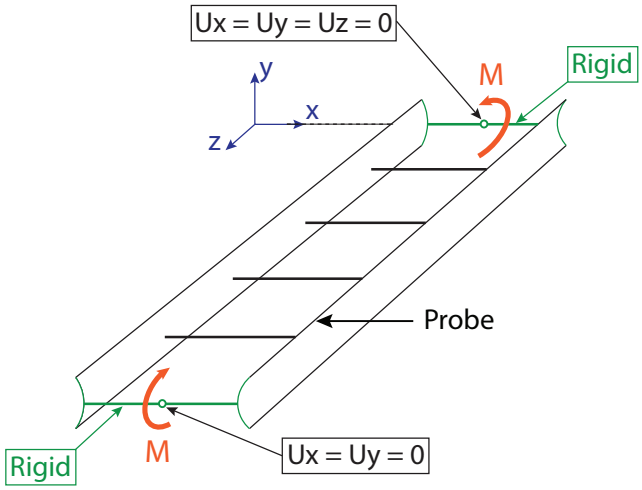

Figure 2.3: Schematic representing the finite element analysis. The end battens and cross-sections are undeformable (in green). One end reference point is pinned while the other end reference point is allowed to slide along the Z-axis and to rotate along all 3 axes. Two equal and opposite moments are applied at the end reference points. When the probing methodology is considered (Section 2.4), a probe is introduced on the top edge of the longeron (longeron and Z location determined by probing scheme). It consists in an applied displacement on the probe node directed along the X-axis.

The strip structure of interest has nonlinear pre-buckling behavior. We will need to distinguish between two types of bifurcation buckling analyses and their associated modes. We will use the standard terminology, classical buckling loads and modes, for results in which the pre-buckling state used in the eigenvalue analysis has been linearized, either about the condition at zero load or at a non-zero load. Our approach will be making use of these eigen-loads and modes to gain insight into the buckling behavior of the strip. However, most of the references to buckling load and modes throughout the chapter will be to "exact" buckling loads and modes computed by analyzing bifurcation from the nonlinear pre-buckling state. Usually we will refer to the "exact" analysis and the outcome with the brief terminology: buckling analysis, buckling loads, and buckling modes. However, if there is any ambiguity the additional terminology, linearized or nonlinear pre-buckling state, will be appended.

2.3 Localization and spatial chaos

Buckling modes and limit points

The first step in assessing the buckling behavior of the strip is to carry out a classical eigenvalue analysis to determine a sequence of the classical applied moments and associated modes at which buckling bifurcations from the perfect strip occur. This information gives a picture of not only the lowest buckling load and associated mode but also of bifurcation modes lurking above the lowest critical mode. Such information gives insight into potentially important imperfection shapes and to "nearby paths" which might play a role in the post-buckling behavior. The computation of the "exact" bifurcation moments and modes is itself is an iterative procedure because the pre-buckling behavior is so nonlinear. To obtain first estimates of the bifurcation points, the pre-buckling nonlinearity is neglected using the ground-state linearity to compute a sequence of the lowest bifurcation eigenvalues (ABAQUS and other structural codes have options for making such eigenvalue evaluations). These bifurcation estimates are then used to guide the search for the bifurcations computed accounting for nonlinear pre-buckling behavior. With full pre-buckling nonlinearity, the strip is then loaded by a moment below the first eigenvalue, the nonlinear pre-buckling problem is solved, and new estimates of the sequence of bifurcation points are computed by linearizing about that state. This iterative process is repeated with an increasing applied moment in each iteration until the bifurcation moments converge. For the strip, nine bifurcation points are determined in the loading interval before the strip attains a limit moment on the fundamental pre-buckling path. As noted earlier, to distinguish between a buckling load of the perfect strip computed using ground state linearity (traditionally called a "classical buckling load") and the buckling load computed accounting for pre-buckling nonlinearity, we will briefly refer to the latter as the "buckling load" and is associated eigenmode as the "buckling mode". The result of this analysis is shown in Figure 2.4.

Both a classical Newton-Raphson solver and the modified Riks solver are used to trace the response of the structure in its unbuckled configuration. The Newton-Raphson solver reaches a limit point at $M = 1464.2$ Nmm, while the Riks solver bifurcates from the fundamental path to a secondary branch at $M = 1435$ Nmm. Note that this moment magnitude is between the first and second buckling moments.

Localization and post-buckling paths

We wish to trace the post-buckling paths corresponding to the several of the lowest buckling eigen-moments and study the evolution of the structure's shape on these

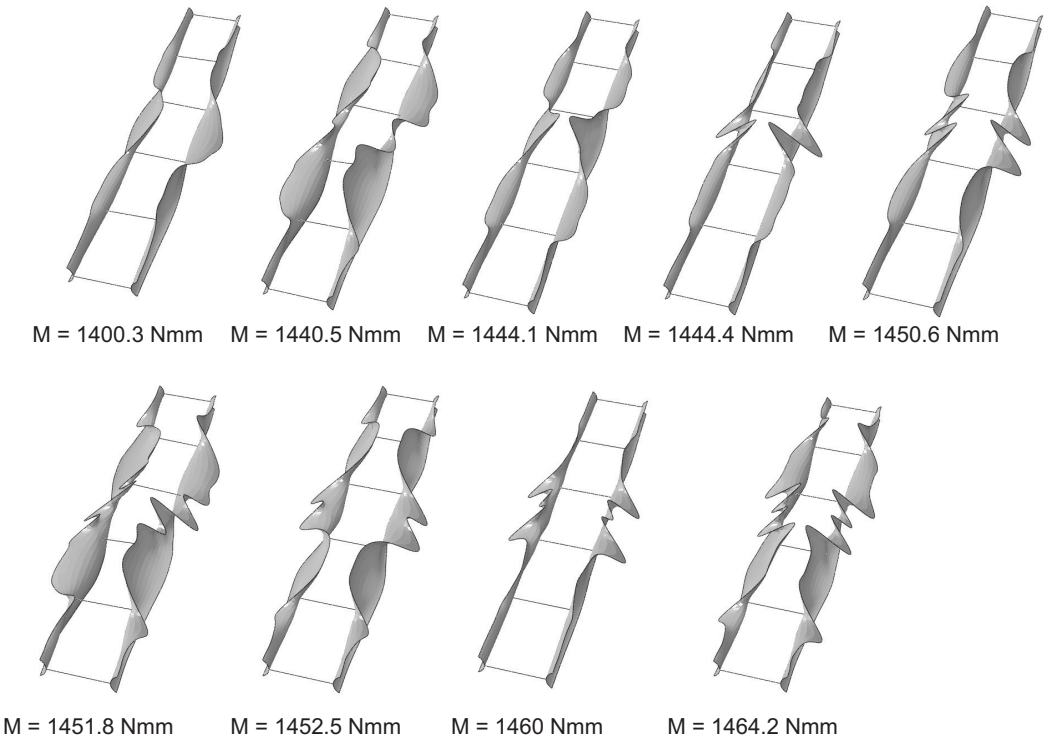

Figure 2.4: 9 buckling modes with associated buckling moments found on the strip fundamental path. These modes exhibit both global and local deformations. For each mode, these deformations appear on both longerons and are concentrated on the longeron's top edge (edge in compression). These deformations are both extending in an inward (towards the strip center) and outward direction. The battens do not exhibit any appreciable deformation.

paths. Of primary interest is the moment/rotation relation for the strip where equal and opposite moments are applied at the strip ends and the rotation corresponds to the rotation around the X axis of the end located at Z = 0 (c.f., Figure 2.3). As a first step, a standard method is used to trace the post-buckling paths associated with the first 3 buckling modes as now described. Each mode is seeded in the structure's initial geometry as a geometric imperfection. The maximum amplitude of this initial imperfection is taken between 1 % and 10 % of the shell thickness (t). The modified Riks solver is used to trace the post-buckling response of the imperfect structure. The computed paths are shown in Figure 2.5, and the corresponding deformed shapes are shown in Figure 2.6. For the second buckling mode, two imperfection amplitudes have been used yielding the two post-buckling paths shown.

The main observation is that the deformed shapes for all the paths exhibit highly localized deformations, contrary to the bifurcation buckling modes. For the first and second mode branches, the post-buckling shapes are quite different from the initial

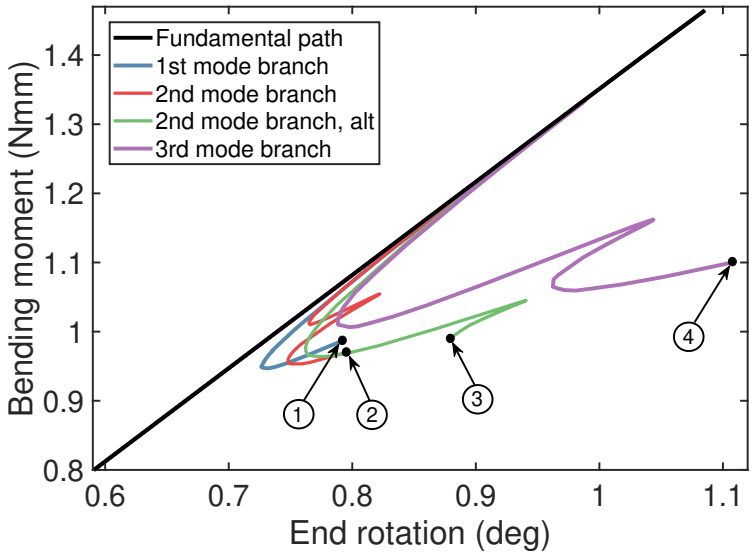

Figure 2.5: Moment/rotation curves for the strip. The fundamental path (black) stops at the limit point $M = 1464.2$ Nmm. The first buckling mode branch (blue) is obtained by seeding the first mode as imperfection with an amplitude of $8\%t$. The second branch (red) is obtained for the second mode imperfection with an amplitude of $8\%t$. The alternate second branch (green) is obtained for the second mode imperfection with an amplitude of $10\%t$. The third branch (yellow) is obtained for the third mode imperfection with an amplitude of $8\%t$. Both second mode branches and the third mode branch exhibit snaking. The deformed shapes obtained at the end of these branches are labeled and shown in Figure 2.6. All branches start lower on the fundamental path than the predicted buckling moments. This highlights the imperfection sensitivity of the structure.

imperfection. These shapes only exhibit inward buckling deformations, whereas the buckling modes also exhibit outward deformations. For the second mode branch, just a slight variation in imperfection amplitude changes completely the buckling location. For the second mode and third mode, the post-buckling paths undergo destabilization and restabilization. This phenomenon is referred to as homoclinic snaking and is also observed for the compressed cylindrical shell [23]. It physically corresponds to the sequential formation of buckles leading to a fully buckled shell. Snaking may occur in all the localized path if the analysis is pushed further. It is interesting to note that we have found that it is possible to resolve the post-buckling path for the third buckling mode without seeding any imperfection in the initial geometry.

For mode 1 and mode 2, the localization process initiates on the imperfect structure's fundamental path, before reaching the falling unstable post-buckling path. Initial

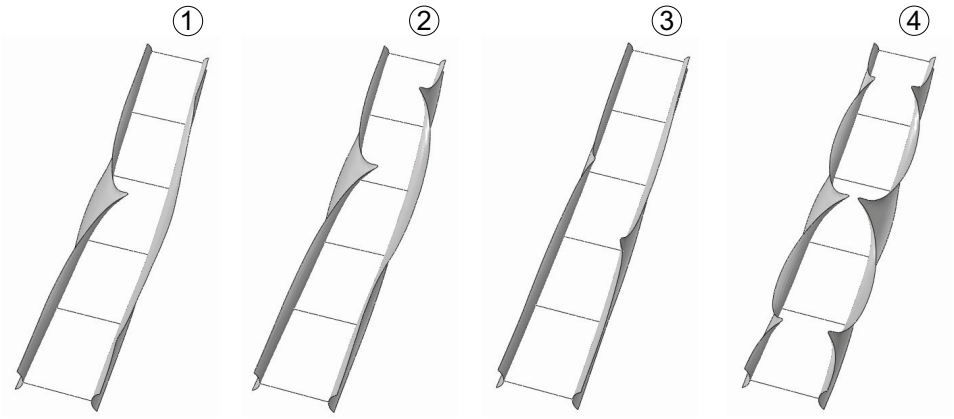

Figure 2.6: Deformed shape obtained at the end of the 4 post-buckling paths of Figure 2.5. They consist in localized longeron deformations and differ from the previously computed buckling modes. All deformations are occurring in the inward direction, and the localization location differs between longerons for the mode 1 branch (labelled 1) and mode 2 branch (labelled 2). Deformations have been magnified by a factor 15 in these images.

deformation grows proportional to the shape of the initial imperfection and then is followed by a transition to a localized mode shape before attaining a limit point. At this point, the location of maximum deformation has already been determined, and on the falling unstable path, the local deformation increases in amplitude without changing location. It is important to emphasize that the limit point for the imperfect structure is offset from the perfect structure's fundamental path, although extremely close to it, due to the eroding affect of the imperfection on the initial stiffness. In addition, these limit points appear at values of applied moment lower than the first buckling moment which reveals the structure's imperfection sensitive nature. Figure 2.7 highlights the localization process for each of the 2 first buckling modes. The displacement of the longeron top edge in the (X-Z) plane is plotted at the limit point as well as at the first post-buckling restabilization point and at the end of the post-buckling path. The normalized buckling mode of the perfect strip is also reported as a dashed line for comparison. For mode 1, localization occurs at two levels. At the structure's scale, local deformations only arise in longeron 1, while for longeron 2, the global deformation tends to cancel the undulations associated with the initial imperfection away for the point of localization. At the longeron scale, the deformed shape goes from a smooth hill to a sharp peak for longeron 2. In addition, the localization process is not unique. We observe different localization mechanisms for buckling mode 2 depending on the imperfection amplitude, as seen on the deformed shape comparison of Figure 2.6. The localization of mode 2 for

an imperfection amplitude of 8%t is shown in Figure 2.7c-d. It highlights the sequential formation of the longeron 1 and longeron 2 buckle characteristics of the snaking process. In the case of buckling mode 3, the buckling mode shape is relatively localized and reassembles the shape observed in Figure 2.6 for the two central buckles. Therefore, no further localization is observed on the post-buckling path before the snaking process is triggered, and four highly localized buckles are formed closer to the longeron ends.

To conclude this section, we re-emphasize that multiple post-buckling paths have been exposed as having initially unstable behavior, but in some cases at least re-stabilized at lower loads. Four different imperfections based on the first 3 buckling modes have been considered here, but other imperfections or linear combinations of buckling modes will give rise to different paths. Seeding imperfections highlights qualitatively the importance of localization for this thin-shell structure and the fact that deformations can localize at many different locations. This multiplicity of buckling and post-buckling solutions is referred to as "spatial chaos." However, we did not consider here all possible localized paths, and we do not know which path constitutes the easiest escape into post-buckling. Based on these qualitative observations, the next section aims at finding this critical localized path by using the probing methodology introduced earlier for the cylindrical and spherical shell.

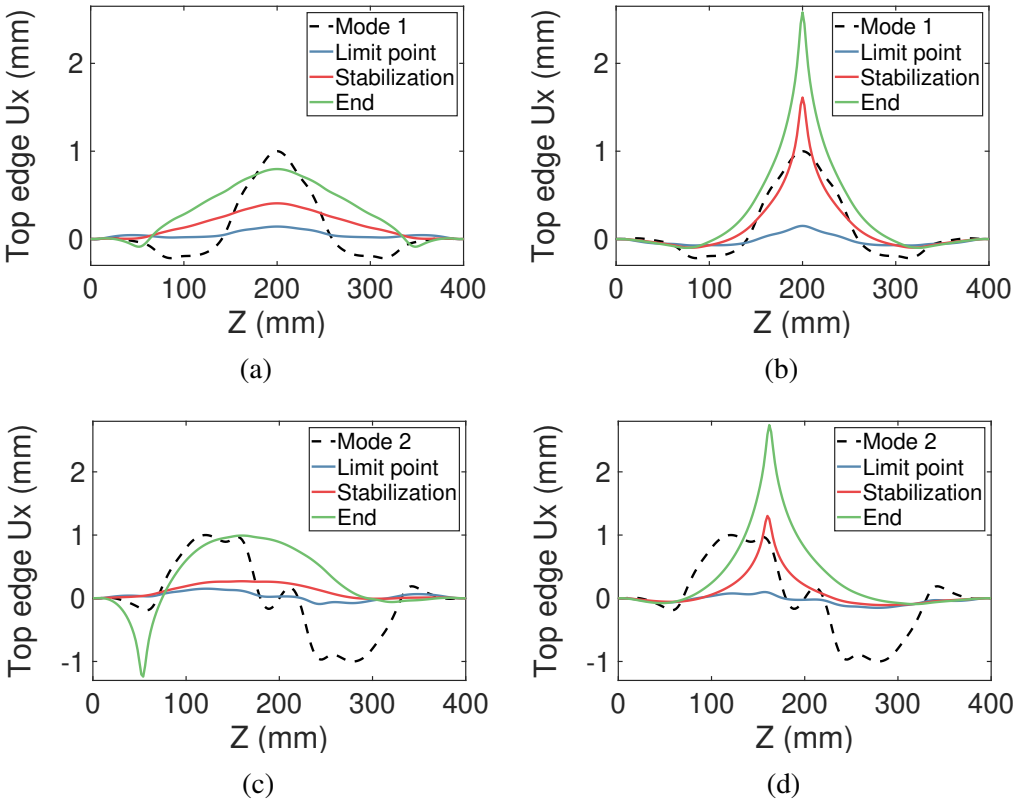

Figure 2.7: (a-b) Localization process for longeron 1 (a) and longeron 2 (b), on the first mode post-buckling path, for an imperfection amplitude of 8%t. The longeron top edge displacement in the X direction is plotted as a function of the strip Z location. The normalized buckling mode is shown as a dashed line. The evolution of the longeron top edge deformation is reported at the limit point, at the point where the post-buckling path first stabilizes and at the end of the post-buckling path. (c-d) Localization process for longeron 1 (c) and longeron 2 (d), on the second mode post-buckling path, for an imperfection amplitude of 8%t.

2.4 Probing along the strip length

Probing methodology

The previous section showed that buckling localization can lead to a large number of post-buckling paths. Our focus in the rest of the chapter is to find the critical buckling mechanism. Here "critical" means that we are focusing on finding the easiest way the structure can buckle, in other words, finding how early the transition into buckling can occur and which deformed shape is the most likely to arise. Two situations may be encountered when end-moments are applied on the structure. The first corresponds to an early transition to a path that intersects the fundamental path, and for which the deformation matches one of the buckling modes (at least at the bifurcation point). This situation may arise for buckling mode 3, for which no imperfection is needed to resolve the post-buckling path. The second situation corresponds to a transition to a disconnected equilibrium path, running in the close vicinity of the fundamental path without intersecting it [36]. In both cases, a finite input of energy into the system is required to make the structure transition early to a secondary equilibrium path. Note that here, "early transition" means that the transition to post-buckling occurs before reaching the first buckling moment. A key assumption made here is that the critical buckling mechanism will exhibit highly localized deformations. This is generally the case for thin-shell structures for which buckling is a sub-critical bifurcation and is motivated by the observations made in the previous section.

The probing method is used to quantify the amount of disturbance needed to trigger early localized buckling. This is achieved by using a probe that displaces the structure locally. In this chapter, the probing method is explored numerically and consists in applying a displacement directed along the X-axis to a node on the top edge of the longeron (the probed node). This is illustrated in Figure 2.3. The top edge is chosen because it corresponds to the location where the structure exhibits the largest compressive stress when bending moments are applied. The analysis goes as follows. The two end-moments are applied on the perfect structure. When the desired moment magnitude is reached, the moment is kept constant and the probe displacement increases. During probing, the probe reaction force is computed. This process is repeated for a wide range of moments up to the first buckling moment, and for various probe locations along the longeron's top edge. In this section, the Abaqus static general solver (Newton-Raphson) is used for both the bending and probing steps. The analysis is restricted to probing paths for which the probe displacement is monotonic.

Two features are of particular interest. The first corresponds to the range of applied moments for which buckled equilibrium states exist. An equilibrium state is located when the probe reaction force falls to zero. When this situation is encountered, there exists at least two equilibrium configurations for a given moment and therefore the fundamental path is meta-stable. Above the moment for which negative probe forces are first encountered, a disturbance may trigger early buckling. The second important feature is the critical amount of energy that needs to be provided to the system to reach the buckled equilibria. It indicates the level of disturbance needed for the structure to transition early into these states.

Five probing schemes are investigated: double outward probing, double inward probing, alternate probing, single outward probing, and single inward probing. They are illustrated in Figure 2.8 and are inspired by the types of deformations seen in the buckling modes. We will restrict our study to one single probe per longeron at most. By characterizing the onset of meta-stability and the critical probe work needed to trigger buckling, we will be using probing as an efficient tool to navigate through spatial chaos and to find the structure's critical buckling mechanism.

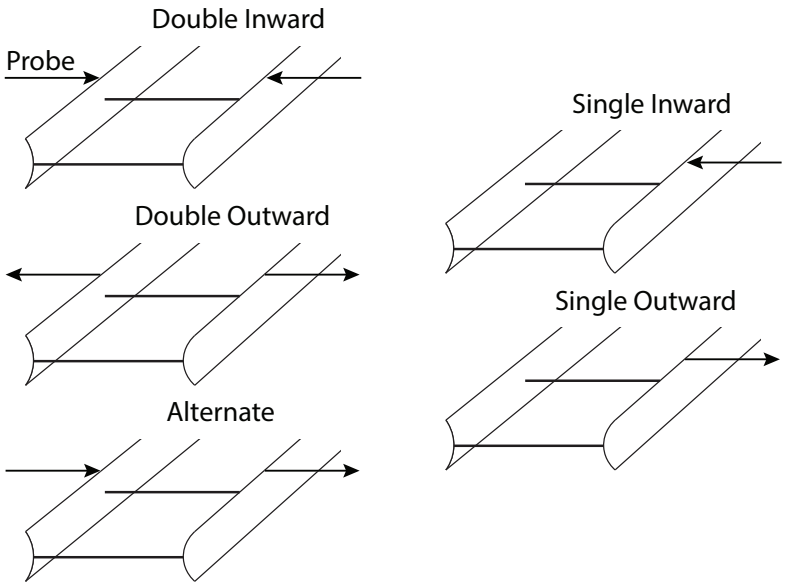

Figure 2.8: 5 probing schemes considered. The arrows are representing the transverse probe displacement. The double inward, double outward, as well as alternate probing schemes are inspired directly by the localized modes found in the previous section. However, we saw that the post-buckling paths exhibit snaking, and to account for a potential sequential formation of buckles, the single inward and single outward probing schemes were also used.

Double inward probing scheme

We first look at the double inward probing scheme. The probe force is plotted as a function of the probe location along the longeron edge (Z-axis), and the probe displacement. These maps are reported in Figure 2.9 for 2 values of applied moments. We focus on a range of moment lower than $M = 1100$ Nmm. For higher moment magnitudes, instabilities are encountered during probing which make convergence hard to achieve. These probe instabilities are analyzed in detail in the next section. This type of probing unveils a rich behavior. For values of moment under 1000 Nmm, probing only yields positive probe forces. The contours of constant probe force exhibit local extrema in the probe location / probe displacement plane. For $M > 950$ Nmm, regions of negative slope appear in the middle of the structure, for probe displacements exceeding 0.2 mm. It creates a positive local minimum of probe force for non-zero probe displacement, and the value of this minimum decreases as M increases. For $M = 1015.5$ Nmm, the local minimum of probe force falls to zero which indicates that the onset of meta-stability is reached for this specific type of localization scenario: buckled equilibrium states appear, and the minimum probe force decreases further to negative values as seen in Figure 2.9b for $M = 1040$ Nmm. One can also notice that local minima of probe force appear at new probe locations, away from the middle of the structure. However, these values never reach zero for moments under 1100 Nmm. These results indicate that early transition into buckling is possible above $M = 1015.5$ Nmm, and that the associated post-buckling shape consists of an inward local buckle in the middle of each longeron. It resembles the third non-linear buckling mode found in Section 2.3.

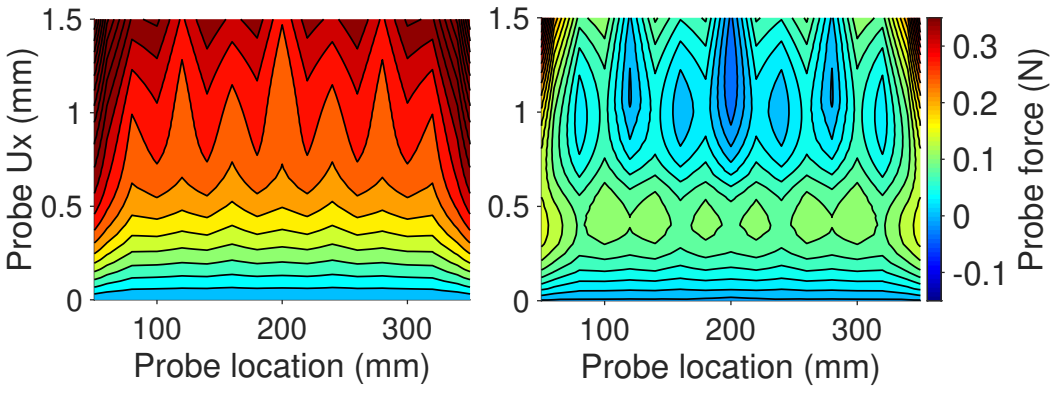

(a) (b)

Figure 2.9: (a) Double inward probing map for $M = 800$ Nmm. The probe force is shown as a function of the probe displacement along the X-axis (U_x) and the probe location along the top of the longeron (Z-axis). For ease of visualization, the regions corresponding to probe location between 0 mm and 50 mm as well as between 350 mm and 400 mm are not shown since they exhibit large probe forces. In these two regions, the probe force vs. probe displacement curve is almost linear. For all other probe locations, the probe force increases monotonically as the probe displacement increases. However, the map exhibits many features, such as regularly spaced local minima of probe force for a given probe displacement. The lowest local minimum is attained in the middle of the structure (200 mm). The probe force is positive for all values of probe displacement. (b) Double inward probing map for $M = 1040$ Nmm. For probe locations ranging from 0 mm to 60 mm and from 340 mm to 40 mm, the probe force increases monotonically as the probe displacement increases. For all other probe locations, the probe force increases and decreases. Regularly spaced local minima of probe force appear, and negative values are reached in the middle (200 mm).

Single inward probing scheme

Next we look at the single inward probing scheme. The corresponding probing maps are reported in Figure 2.10 for 4 values of applied moment. For $M < 900$ Nmm, probing only yields positive probe forces. The magnitude of these forces is very similar to the ones obtained for the double inward probing scheme. However, more features appear in these maps, and a basin of low probe force develops in the middle of the longeron for $M = 800$ Nmm. At $M = 950$ Nmm, the probe force first falls to zero which indicates the onset of meta-stability for this specific localization scenario. It means that early transitions into a single inward post-buckling path are possible. It is important to notice that as the moment increases, the probe displacement at which the local minimum is reached decreases. For $M = 800$ Nmm, this probe displacement is 1.2 mm and reduces to 0.78 mm for $M = 1040$ Nmm. Another

important observation is that meta-stability appears earlier for this type of probing than for the double inward probing scheme. For higher moment magnitudes, the minimum of probe force is still achieved in the middle of the structure, but the region of negative probe force spreads over a larger portion of the structure. Therefore there exist multiple locations at which buckled equilibrium states are found. This supports the observations of Section 2.3 where we saw that localization for the second mode imperfection can occur at multiple locations. However, we see qualitatively that the hill of probe force separating the unbuckled and buckled states is lowest in the middle, which signifies that the minimum energy input required to form an inward buckle is also achieved in the middle of a single longeron. For $M = 1200$ Nmm, the probing map resembles qualitatively Figure 2.10b. A region of negative probe force is reached in the middle of the structure for a probe displacement of 0.35 mm. In addition, a second minimum of probe force forms in the middle for a probe displacement of 0.2 mm. However, when probing at other locations than the middle, the probing path encounters instabilities as the probe force decreases after the peak, and the Newton-Raphson solver aborts. It leaves the probing map incomplete. Again here, we see that the probe displacement for which local minima of probe force are attained decreases as the moment increases. When increasing the moments to $M = 1350$ Nmm, instabilities occur for even smaller values of probe displacement (as soon as 0.1 mm) and truncates the probing map. Furthermore, the map exhibits two distinct regions of negative probe force in the middle, for a probe displacement of 0.075 mm and a probe displacement of 0.14 mm. This shows that probing can detect adjacent post-buckling equilibrium solutions. However, the overarching goal of the probing method is to compute the minimum energy input needed to trigger early buckling for every probe locations. Here it is not yet possible due to the probe instabilities. At the locations where the probing sequence suddenly stops, it is impossible to draw any conclusions regarding the structure's meta-stability. It is therefore necessary to resolve probing sequences past these instabilities, and this is the subject of Section 2.5.

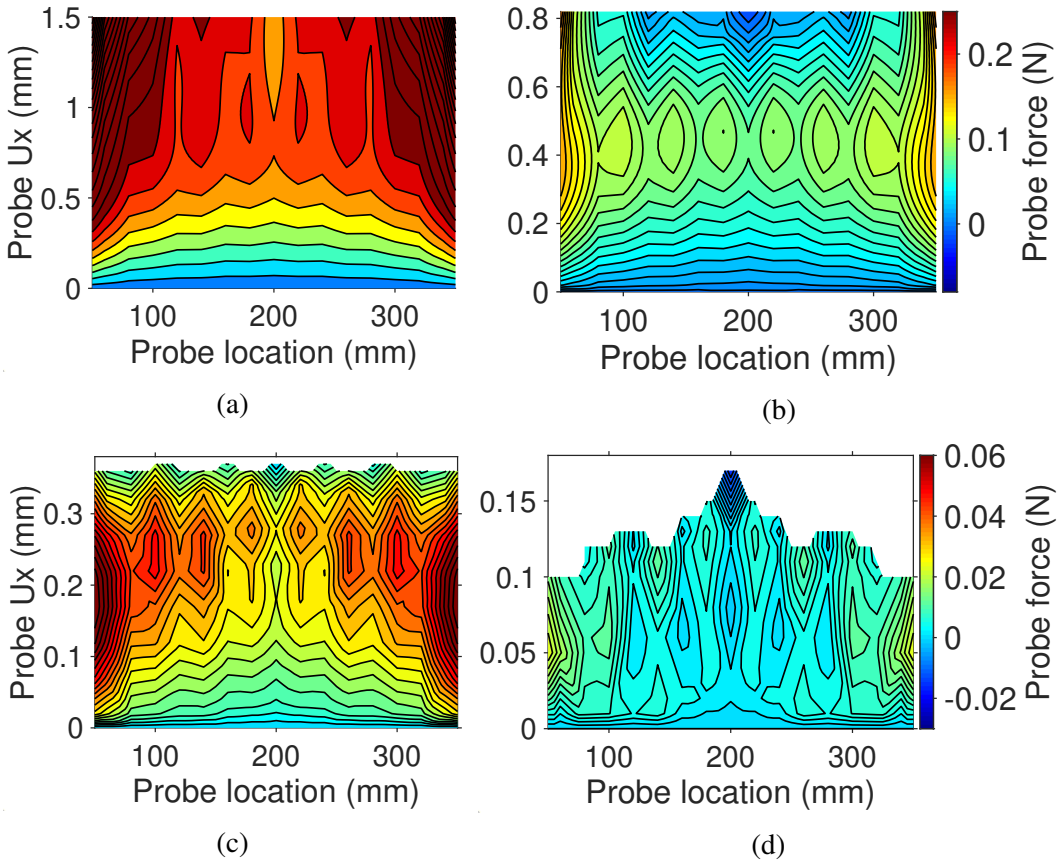

Figure 2.10: (a) Single inward probing map for $M = 800$ Nmm. As the probe displacement increases, the probe force increases monotonically, except in the middle and its vicinity, for which a basin of local minima appears (probe displacement of 1.2 mm). The probe force is positive everywhere. (b) Single inward probing map for $M = 1040$ Nmm. Local maxima of probe force appear and form a hill separating the fundamental path and regions of local minima. The local minimum is negative in the middle, whereas it stays positive at other locations, while being very close to zero. This map resembles the one obtained for the double inward probing scheme. (c) Single inward probing map for $M = 1200$ Nmm. A local minimum of probe force appears for a probe displacement of 0.2 mm, before reaching the negative probe force region at 0.35 mm. Probe instabilities truncate the map prematurely for probe locations different from 200 mm. (d) Single inward probing map for $M = 1200$ Nmm. The probe instabilities appear as early as 0.1 mm of probe displacement and cause a severe truncation of the map. The probing path in the middle exhibits two regions of negative probe forces (for 0.075 mm and 0.14 mm) indicating two adjacent buckled equilibrium states.

Outward and alternate probing schemes

We focus here on the double outward probing scheme. For this specific type of probing, the structure does not exhibit any moment for which the probe forces

decreases to 0 N. Instead, as the longeron is locally displaced outwards under constant applied moments, the probe force increases monotonically. The probe force reaches 1 N for a probe displacement of about 1 mm, which is an order of magnitude higher than the probe force obtained with the double inward probing scheme. Probing does not reveal any buckled equilibria.

The alternate probing scheme exhibits a more complex behavior. One probe is being displaced in the inward direction whereas the other is being displaced in the outward direction. For the outward probe applied on longeron 1, the probe force increases monotonically as the probe displacement increases similarly to what was observed for the double outward probing scheme. However for the inward probe on longeron 2, the probe force in the center becomes negative for all probe displacements, above a certain moment magnitude. This suggests that the outward probe alone on longeron 1 may be able to generate a buckle on longeron 2. It highlights that the disturbance brought by probing can be transferred between longerons. However since the outward probe force never falls to 0 N, probing does not reveal any buckled equilibria. Similar behavior is observed for the single inward probing scheme. When the probe outward displacement increases, the probe force monotonically increases, while an inward buckle forms in the unprobed longeron. Similarly to the alternate probing scheme, no equilibrium configurations are encountered, but the probing path is truncated before the prescribed end displacement is reached due to instabilities. These instabilities are analyzed in Section 2.5.

These 3 probing schemes seem to indicate that buckling localization can only arise in the inward direction, since no outward buckled configurations are detected during probing. This conclusion supports the observation of Section 2.3 for which no outward localization was observed. However, the single outward probing scheme showed that probing one longeron in the outward direction can cause the other longeron to buckle inward, even if no equilibrium states were detected. It is shown in Section 2.5 that such states exists if probing is extended past instabilities.

Critical probe work and initial probing schemes comparison

In order to find the critical buckling mechanism for the strip structure, the probing schemes presented above need to be compared. The critical buckling mechanism corresponds to the mechanism for which the minimum amount of energy is needed to reach buckled equilibria. In practice, this energy is brought by disturbances. For the present study, special care has to be taken with the terminology, especially when

referring to the energy barrier to buckling and the critical probe work.

In all buckling and probing studies referenced in this chapter, the energy barrier refers to the difference in total potential energy between the unbuckled state and the unstable buckled state. As explained in the introduction, the unstable buckled state corresponds to a saddle point (also called mountain pass point) in the energy landscape and is attained for a critical value of probe displacement, when the zero threshold in probe force is reached. If the main loading is kept constant, the probe work reaches a local maximum at this critical displacement. We will use the terminology of "critical probe work" to refer to this local maximum of probe work. When the probe displacement is monotonic during probing (no folding of the path), and for a displacement-controlled main loading, the critical probe work is equal to the energy barrier. This scenario is for instance encountered for the probed cylinder under constant end shortening [81]. However in the present study, energy barrier and critical probe work can be different for the two following reasons:

- The main loading is moment-controlled, which means that probing occurs at a constant value of end-moment. During probing, the ends of the strip are rotating and the end-moments are doing work. As a result, the energy barrier is greater than the critical probe work since it accounts for the end-moments' additional contribution to the energy of the system. However, the constant moments are part of the known conditions the structure is subjected to during operation. Therefore the contribution of an unknown disturbance is only represented by the probe here, and as such the quantity of interest is the critical probe work. The study has been repeated in the case of a rotation-controlled loading and is presented in Section 2.7. In the later case, the probe work only contributes to the total external work of the system.

- For unstable probing sequences, a vertical tangent can be reached and the probing path can fold. In such cases, snap-buckling can be triggered before the zero probe force threshold is attained, and the value of critical probe work is computed at the point of vertical tangent rather than at the first buckled equilibrium. Such cases are presented and analyzed further in Section 2.5.

We next focus on the critical probe work for the two inward probing schemes. We saw that for both schemes, the probing path does not exhibit any instabilities in the middle of the structure. As a result, meta-stability can be detected, and the critical

probe work required to reach the buckled equilibrium states can be computed. The critical probe work obtained for the middle probe location and for both probing schemes is shown in Figure 2.11.

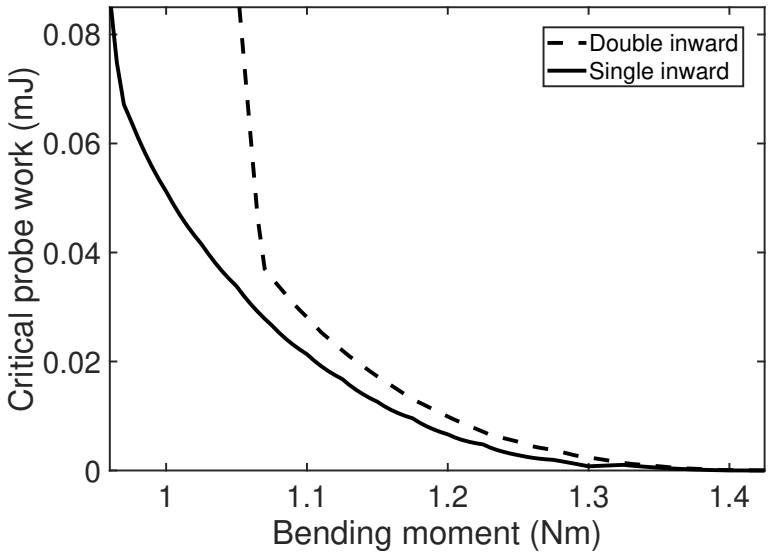

Figure 2.11: Critical probe work between fundamental as a function of applied bending moment, for both single and double inward probing schemes, for the central probe location. It corresponds to the work done by the probe force between the two states. The single inward probing scheme gives the smallest energy barrier for all bending moments.

The single inward probing scheme gives a lower critical probe work than the double inward probing scheme for the entire range of moments considered. As a result, if buckling is to be triggered early, it likely to consist of a single buckle in the middle of one of the longerons rather than on both longerons. When comparing the local maximum of probe force obtained for both probing schemes, we also see that it is the lowest for the single inward probing scheme, regardless of the probe location. It seems therefore that if meta-stability is detected at a specific probe location, the single inward probing scheme would also give the lowest critical probe work at this specific location. Finally we saw in this section that buckled equilibrium states appear for lower values of moments for the single inward probing scheme. As snaking seems to play a prominent role for this structure, we would expect a sequential formation of single buckles which supports the energy comparison between the two probing schemes. For all these reasons, the rest of the chapter will only focus on the single inward / outward probing schemes rather than the double probing schemes.

2.5 Unstable probing sequences

Single inward probing

This section extends the probing simulations to probing locations and moments for which instabilities are encountered. The probing displacement is applied similarly to what has been done before, but an arc-length solver (Riks solver) is now used, which allows probing to continue even after a vertical tangency (fold) in the probe force vs. probe displacement plane is reached. These probing sequences are first computed for the single inward probing scheme and for all probing locations. The 2 main types of probing path instabilities encountered are analyzed in this section.

The results of this analysis for a probe located at 100 mm from the end of the structure is shown in Figure 2.12. For moments of low magnitude ($M < 1050$ Nmm), the probing path is stable and the probe force exhibits a local maximum and local minimum. However, the probe force is always positive and no locally buckled equilibrium solutions exist. For $M = 1050$ Nmm, a vertical tangent is encountered and the path folds. This path eventually restabilizes for a value of probe force of about -0.1 N. However, the restabilized path is short and does not reach positive probe forces. This suggests that another bifurcation is encountered for a probe displacement of about 0.2 mm. This behavior is also encountered for higher values of moments, although the corresponding probing paths do not restabilize for positive values of probe displacement. Figure 2.13a shows the probing path for $M = 1050$ Nmm with four key points on the probing sequence.

The deformed shapes obtained for these four points are shown in Figure 2.13b. On the stable part of the path (before reaching point 2), displacing the probe results in an increase in local buckle amplitude. After point 2, the probing path becomes unstable. As the probe displacement decreases, the probe force increases to point 3 to then decrease to 0 N at point 4, which corresponds to a buckled equilibrium solution. Physically, the unstable path corresponds to the change of location of the buckle formed during the stable probing path. At point 4, a local buckle in equilibrium exists in the structure, but the final buckle location does not correspond to the probing location. Note that the probe force vs. probe displacement curve has a positive slope at point 4 which means that the equilibrium is stable. The critical probe work required to form the localized buckled configuration at point 4 corresponds to the shaded area shown in Figure 2.13a. It is important to point out that this area does not correspond to the energy barrier per se, as explained in the previous subsection. In order to compute the energy barrier, i.e the difference in

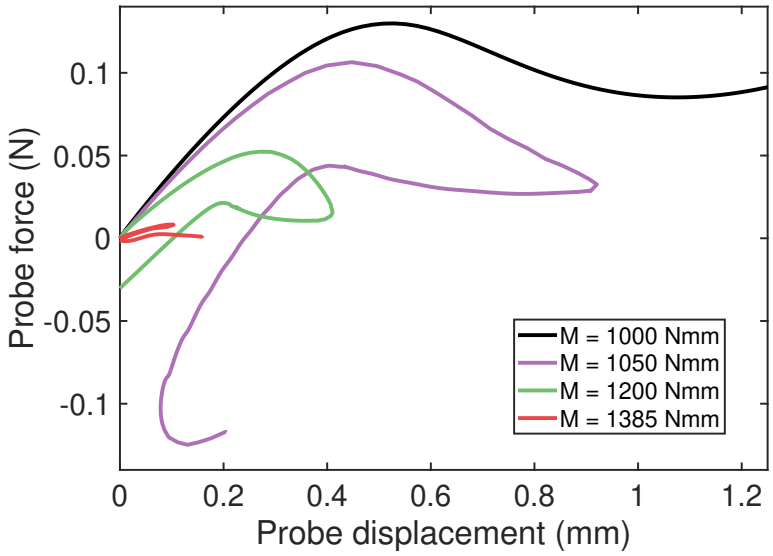

Figure 2.12: Probe force vs. probe displacement for a probe located at $Z = 100$ mm and for 4 values of applied moment. For $M = 1000$ Nmm, the path exhibits a local maximum and local minimum without reaching the zero threshold for the probe force. The path is well behaved and can be resolved with a Newton-Raphson solver. For $M = 1050$ Nmm, the path starts folding. The point of vertical tangency is reached for a probe displacement 0.92 mm, and the path past this point would not be resolved with a Newton-Raphson solver. The loop formed by the path folding is becoming smaller as the moment magnitude increases until it folds on itself for $M = 1385$ Nmm.

total potential energy between the unbuckled state and the buckled state at point 4, the area enclosed by the probing path would have to be considered. The area under the curve formed by points 2, 3 and 4 would have to be subtracted from the shaded area, and the work done by the end-moments would have to be added.

Path folding has also been encountered in the case of a compressed spherical shell being probed at its pole, under rigid volume control [79], and all of the generic bifurcations that can arise and disrupt a probing sequence have been described [77]. Two approaches have been proposed to explore experimentally these unstable probing sequences. The first one consists in introducing feedback control [77]. If the probe displacement and probe force are chosen as inputs, it is then possible to resolve vertical tangents. It is also possible to navigate around the fold and avoid unstable probing paths by using the moment and probe displacement as inputs. Another approach consists in using additional probes to suppress instabilities [79].

We next analyze the probing paths for a probe located at 160 mm from the end of

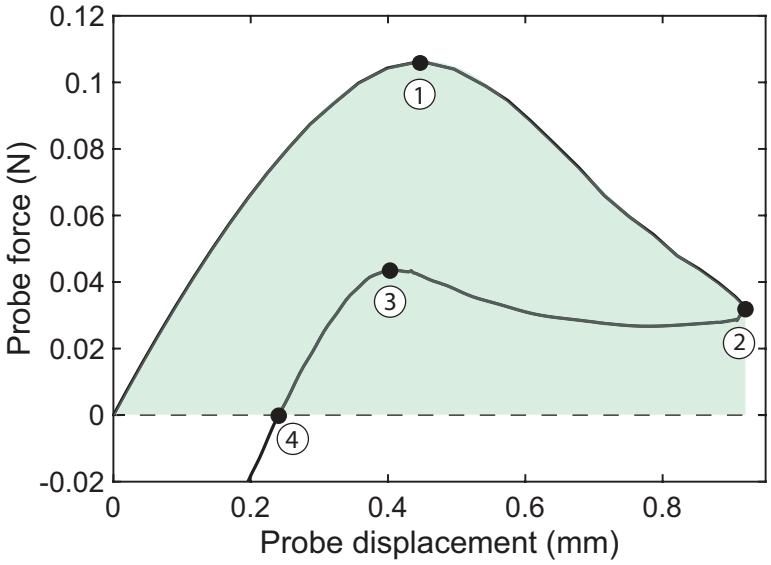

(a)

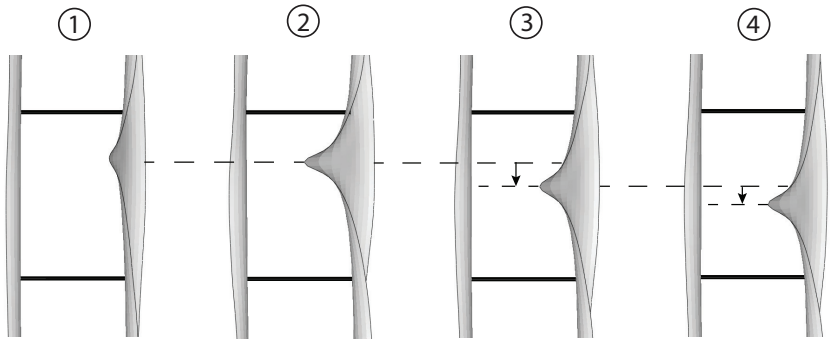

(b)

Figure 2.13: (a) Probing path for a probe located at $Z = 100$ mm and an applied moment $M = 1050$ Nmm. 4 key points are highlighted and corresponds to the deformed shape shown in (b). The area shaded in green is the probe work needed to be input into the structure to trigger snap-buckling. (b) Mode shapes obtained at point 1, 2, 3, and 4 on the probing sequence. The stable part of the path (point 1 and 2) corresponds to the growth of the buckle formed by the probe. On the unstable part of the path (point 3 and 4), we observe that the buckle previously formed is shifting location. Deformations have been magnified by a factor 20 in these images.

the structure. The paths are shown in Figure 2.14. For moments of low magnitude ($M < 1050$ Nmm), we observe similar results as the previous probe location. The probing path is stable and the probe force exhibits a local maximum and local minimum. For $M = 1050$ Nmm, we see a similar path folding as observed previously. However the restabilized path extends further and reaches positive probe forces, which indicates that a stable equilibrium solution exist. As the moments

increase in magnitude, we observe probing path spiraling. The number of spirals formed increases as the moment magnitude increases and the spacing between spirals decreases. These spirals disappear closer to the buckling moment.

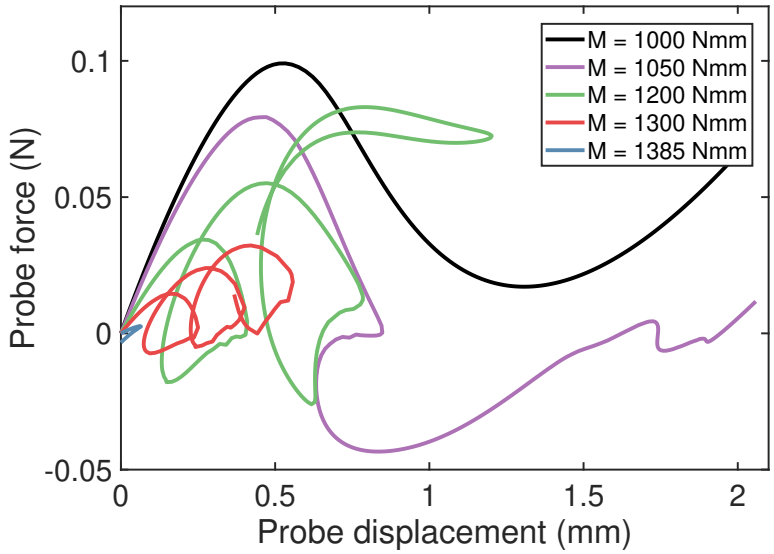

Figure 2.14: Probe force vs. probe displacement for a probe location at 160 mm and for 5 values of applied moment. For $M = 1000$ Nmm, the path exhibits a local maximum and local minimum without reaching the zero threshold for the probe force. The path is well behaved and can be resolved with a Newton-Raphson solver. For $M = 1050$ Nmm, the probe path starts folding and the point of vertical tangency is reached for a probe displacement 0.85 mm. The path folding is then replaced by path spiraling as the moment is increased, which indicates that multiple equilibrium solutions exist in parallel. The number of equilibrium solutions encountered on the probing path increases as the moment increases. For $M = 1200$ Nmm, 4 equilibrium solutions are detected and the spiraling evolves for $M = 1300$ Nmm to reveal 5 equilibrium solutions. Close to the buckling load, at $M = 1385$ Nmm, a single path is observed for extremely small values of probe displacement, which indicates an extremely low critical probe work.

The probing path for $M = 1300$ Nmm is shown in Figure 2.15a, and the 5 equilibrium states are indicated. The deformed shapes obtained at these points are shown in Figure 2.15b. As the probe displacement increases initially, the probe force increases and then decreases. The probing path becomes unstable right before reaching the first equilibrium state (1). At this point, a buckle (buckle 1) in equilibrium is formed in the longeron at the probing location. Notice that this first equilibrium solution is stable since the path slope is locally positive. The unstable path between state 1 and 2 exhibits negative probe forces, and we observe the initially formed buckle traveling along the longeron's top edge. This situation is similar to what has been observed at

the 100 mm probe location. The main difference is that the path restabilizes with an immediate increase in probe force. Point 2 is now also an equilibrium state, whereas we only located one equilibrium solution before. Equilibrium state 2 is also stable. From state 2 to state 3, the probe force increases, and the magnitude of the maximum probe force is about twice the one attained before state 1. On this part of the path, buckle 1 continues to travel along the longeron, and a second buckle (buckle 2) is forming at the probe location. The path loses stability at a probe displacement of about 0.4 mm and reaches the stable equilibrium 3, for which buckle 1 and buckle 2 are sustained, forming a "train" of 2 buckles. This buckle formation shifts location before reaching the unstable equilibrium 4. The path proceeds with a third loop and the 2-buckle formation continues traveling, while a third buckle (buckle 3) is being formed at the probe location. The path reaches equilibrium 5 for which 3 buckles in series are sustained in the longeron. Note that point 5 also corresponds to a local minimum of probe force and as a result, no negative probe forces appear anymore on the path.

Two other situations are encountered. Closer to the strip ends (probe location between 20 mm and 60 mm) hysteresis is observed. The probe displacement first increases, and the probe force increases until reaching a limit point, after which the probe displacement decreases and the path returns to the origin. However, the return path does not coincide with the first stable portion and exhibits lower probe forces. This situation physically corresponds to a complex interaction between longerons. The local inward displacement imposed on longeron 1 by the probe causes a macroscopic in-plane bending of the full structure, causing the unprobed longeron (longeron 2) to buckle. This transfer of energy between longerons through the battens was also encountered for the alternate probing scheme and for the unstable single outward probing scheme described in the next section. Finally, for some combination of probe locations and moments, the solver stops before the end of the analysis and the full probing path cannot be resolved. This is due to secondary bifurcations being encountered during probing. While path folding and spiraling could be resolved using the Riks solver alone, continuing these probing paths after the bifurcation would require more evolved continuation algorithms [25] and is beyond the scope of this chapter. In most cases, path folding is observed before reaching the bifurcation point, but the path stops before reaching the zero threshold for the probe force. Therefore, no equilibrium solutions can be detected, and they may or may not exist. However, it is still possible to compute the probe work required to trigger snap-buckling, when the vertical tangent is reached.

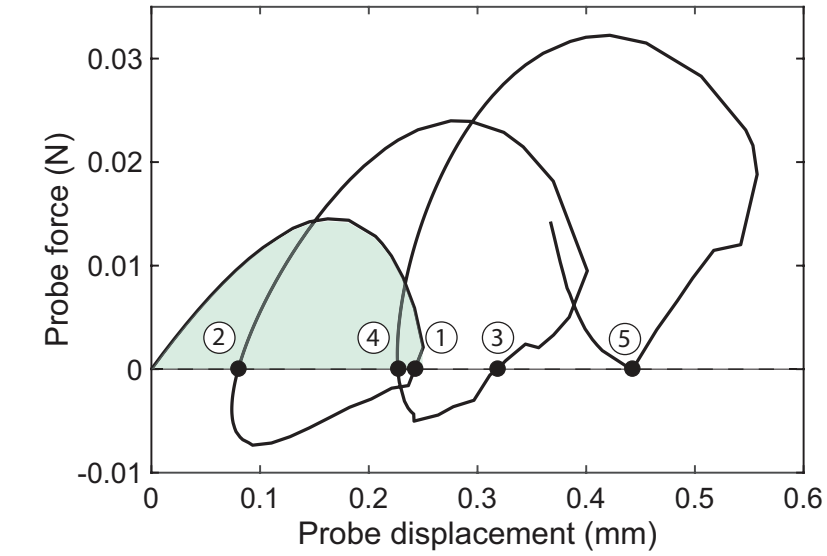

(a)

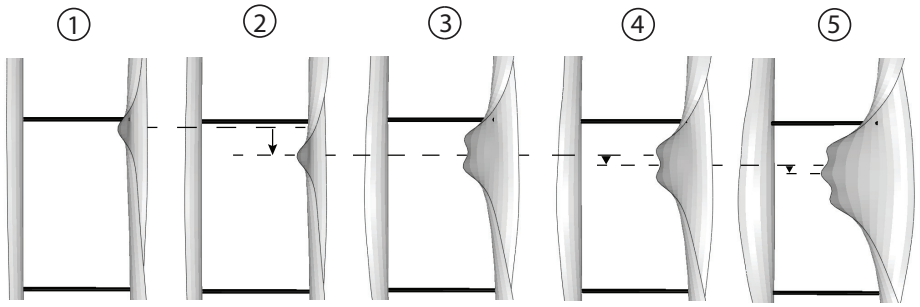

(b)

Figure 2.15: (a) Probing path for a probe location at Z = 160 mm and an applied moment M = 1300 Nmm. 5 key points are highlighted and corresponds to the deformed shape shown in (b). The area shaded in green is the probe work needed to be input into the structure to trigger snap buckling. (b) Mode shapes obtained at point 1, 2, 3, 4, and 5 on the probing sequence. These points are all equilibrium solutions. Points 4 and 5 correspond to unstable equilibria. The first loop yields a single buckle equilibrium at the probe location and a shifted single buckle equilibrium. The second loop gives double buckle equilibrium and the third one, a triple buckle equilibrium. Deformations have been magnified by a factor of 40 in these images.

Single outward probing

No buckled equilibrium solutions were detected when the single outward probing scheme was used in Section 2.4, and the probe force increased monotonically as the probe displacement increased. Even if buckled equilibrium states seemed at first unlikely to be encountered for this type of probing, the probing paths were

prematurely terminated by instabilities and therefore no conclusion could be drawn regarding their existence. Here, the Riks solver is used to compute the probing paths past vertical tangents. Surprisingly however, we found that the single outward probing scheme is able to trigger inward buckled equilibria, and the two main buckling mechanisms are analyzed below.

The first buckling mechanism corresponds to the formation of a buckle, in the unprobed longeron. Probing at $M = 1100$ Nmm and at a location of 180 mm exhibits this behavior, and the corresponding probe force vs. probe displacement curve is shown in Figure 2.16a. The structure's deformed shapes obtained at selected points on the path are shown in Figure 2.16b. The probing sequence starts with a monotonic increase in probe force as the probe on longeron 1 is displaced outwards. The deformed shape at point 1 shows the large displacement of the probed longeron but no localization is observed. However pulling on longeron 1 results in a global in-plane bending of the structure, which creates inward displacement of the unprobed longeron 2, since the two longerons are connected by the battens. Past point 1, the probe displacement decreases and the inward displacement of longeron 2 localizes to form a buckle. At point 2, the inward buckle on the unprobed longeron 2 is in equilibrium and stable. Once the probe displacement becomes negative, the single inward probing scheme is recovered and an inward buckle is formed on the probed longeron 1. Path folding is then observed which corresponds physically to the buckle on longeron 1 travelling, as described in the previous subsection. The only difference here is that the initial outward probing created an additional inward buckle on longeron 2.

The second buckling mechanism is more surprising and corresponds to the formation of an inward buckle in the longeron probed outward. Probing at $M = 1300$ Nmm and at a location of 120 mm exhibits this behavior, and the corresponding probe force vs. probe displacement curve is shown in Figure 2.17a. The structure's deformed shapes obtained at key points on the path are shown in Figure 2.17b. The probing sequence starts again with a monotonic increase in probe force as the probe on longeron 1 is displaced outwards. The deformed shape at point 1 shows the large displacement of the probed longeron, but inward localization is observed farther away from the probe, on the same longeron. Past point 1 the path becomes unstable, and the localized fold present at point 1 is localized to form an inward buckle on the probed longeron. The local hump in probe force observed on the unstable path corresponds to the buckle traveling until the stable equilibrium at point 2 is reached.

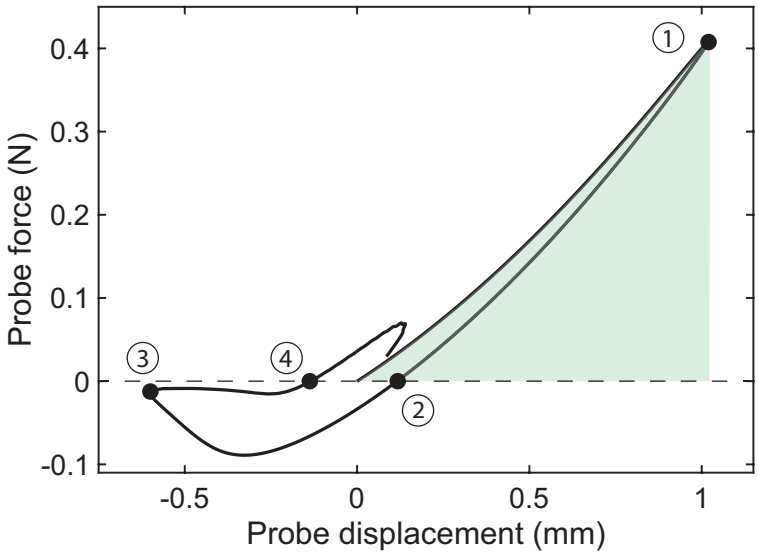

(a)

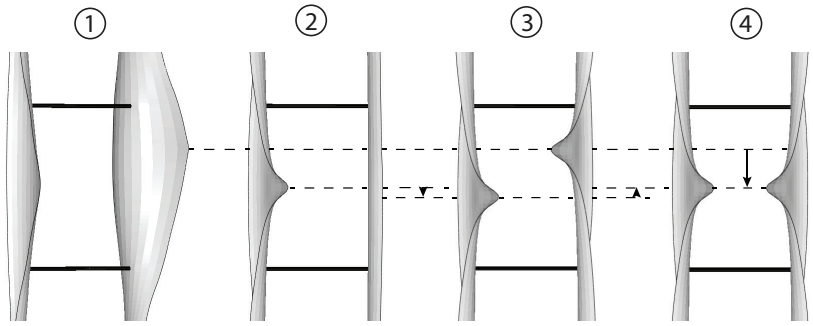

(b)

Figure 2.16: (a) Probing path for a probe located at Z = 180 mm and an applied moment M = 1100 Nmm. 4 key points are highlighted and correspond to the deformed shapes shown in (b). The area shaded in green is the probe work needed to be input into the structure to trigger snap buckling. (b) Mode shapes obtained at point 1, 2, 3, and 4 on the probing sequence. The unstable part of the path (point 1 and 2) corresponds to the growth of the inward buckle formed on the unprobed longeron. After point 2, the single inward probing scheme is recovered and buckle traveling is observed. Deformations have been magnified by a factor of 30 in these images.

After point 2, the single inward probing scheme is recovered and an additional buckle is formed on the probed longeron. Path folding is again observed here.

Finally, other types of outward probing paths are encountered for different probe locations and consist of a superposition of the two simple buckling sequences described above. Note that once the first buckle has been formed by the outward

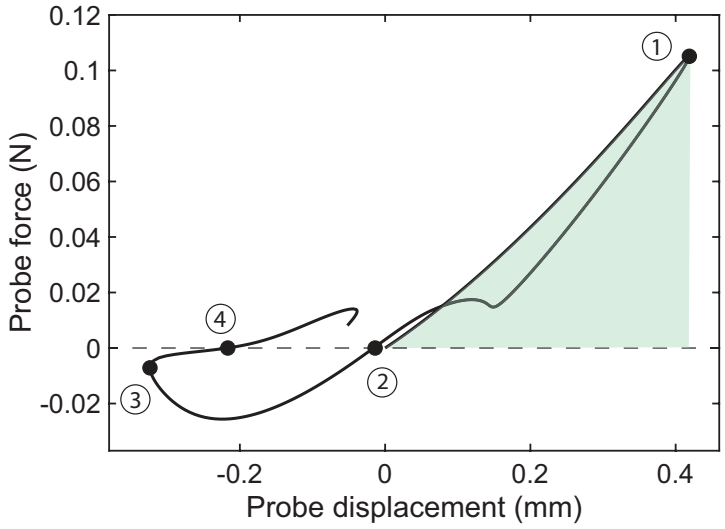

(a)

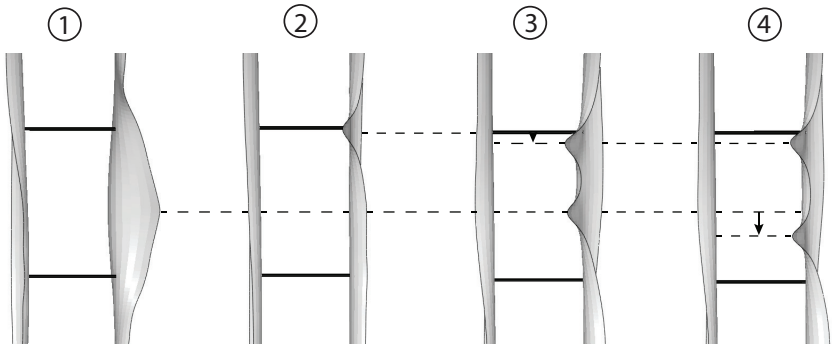

(b)

Figure 2.17: (a) Probing path for a probe located at 120 mm and an applied moment $M = 1300$ Nmm. 4 key points are highlighted and corresponds to the deformed shape shown in (b). The area shaded in green is the probe work needed to be input into the structure to trigger snap buckling. (b) Mode shapes obtained at point 1, 2, 3, and 4 on the probing sequence. At point 1, the probed longeron exhibits large outward deformations, but a local fold is observed right above the displaced region. This folds localizes to form a buckle and a second buckle is formed through inward probing. Buckle traveling is also observed. Deformations have been magnified by a factor of 50 in these images.

probing scheme, these paths can exhibit spiraling, and very complex series of buckles in equilibrium can be found. The analysis of each of these complex situations is beyond the scope of this chapter, and corresponds to even more equilibrium solutions. The main take away here is that both the single inward and single outward probing schemes can trigger inward buckling, and no outward buckling has been observed for this structure. For each probing scheme, a value of critical probe work to trigger

snap-buckling can be computed.

Critical probe work map

The analysis is repeated for all probe locations, moments, and both the single inward and single outward probing scheme. It leads to the two critical probe work plots shown in Figure 2.18. Each color corresponds to a given moment magnitude. When probing is achieved past the first zero threshold in probe force, a buckled equilibrium is detected and indicated by a dot. In some cases, secondary bifurcations are encountered on the probing path before reaching the zero probe force threshold. In this case, additional techniques need to be used to trace the full probing path. However, the critical probe work can be computed and is reported without a dot. If the probing path can be fully resolved but never crosses the zero probe force threshold, the maximum work done by the probe is also reported without a dot. Since the problem is symmetric with respect to the middle transverse axis of the strip, we are only reporting results for half a strip in Figure 2.18. No early buckling can be triggered for a strip location between $Z = 0$ mm and $Z = 20$ mm, and this region is not shown. Finally, it is important to highlight that the probe location does not necessarily coincide with the buckling location.

We first focus on the inward probing scheme for which the critical probe work is shown in Figure 2.18a. Multi-stability is first detected in the middle of the strip (probe at 200 mm) for $M = 950$ Nmm, and for higher values of moments, the meta-stable region extends almost on the entire length of the structure. For moment values under 1385 Nmm, the minimum critical probe work is always reached in the middle of the strip (probe at 200 mm) and is extremely small. For $M = 1000$ Nmm, it is about 0.06 mJ and quickly drops under the microjoules threshold for $M = 1350$ Nmm. These magnitudes make early buckling extremely likely to occur in an experiment. Closer to the first buckling moment ($M = 1400.3$ Nmm), the location of the minimum critical probe work is changing. It is attained for a probe at 180 mm for $M = 1385$ Nmm and shifts to 160 mm for higher values of moments. Note that for this range of high moments, the critical probe work drops dramatically. At $M = 1400$ Nmm, the critical probe work first drops to zero (marked as 10^{-7} in Figure 2.18 by convention).

We saw in the previous subsection that the single outward probing scheme also induces inward buckling of the probed or the unprobed longeron. The critical probe work for the single outward probing scheme is reported in Figure 2.18b.

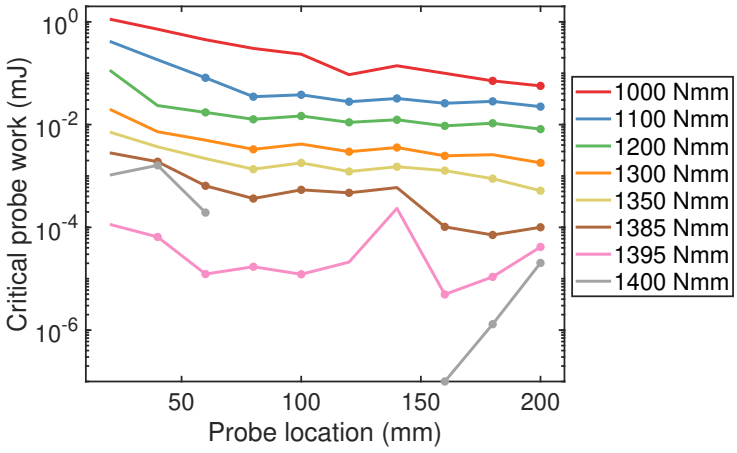

(a)

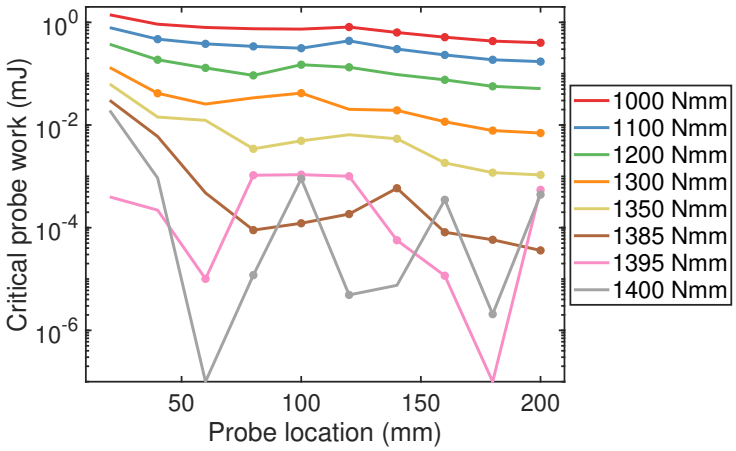

(b)

Figure 2.18: (a) Critical probe work map for the single inward probing scheme. When probing is achieved past the first zero threshold in probe force, a buckled equilibrium is detected and indicated by a dot. In some cases, secondary bifurcations are encountered on the probing path before reaching the zero probe force threshold. In this case, additional techniques need to be used to trace the full probing path. However, the critical probe work can be computed and is reported without a dot. For moments under $M = 1385$ Nmm, the minimum critical probe work is reached in the middle of the strip (probe location 200 mm). Closer to the buckling moment, the minimum critical probe work location shifts and falls to 0 mJ for $M = 1400$ Nmm. (b) Critical probe work map for the single outward probing scheme. The trend is similar to the single inward probing scheme except that the single outward probing scheme requires more energy to trigger inward buckles than the single inward probing scheme, for all values of moment.

Qualitatively, the behavior reassembles what was observed for the single inward probing scheme. The minimum critical probe work is attained in the middle of

the strip for moment values below $M = 1385$. However, the critical probe work is consistently higher for this type of probing, suggesting that inward probing is the critical disturbance for this structure. Closer to the buckling moment, for $M > 1385$ Nmm, the minimum critical probe work is similar for the inward and outward probing schemes. At $M = 1400$ Nmm, the critical probe work first drops to zero (marked as 10^{-7} in Figure 2.18 by convention) but for a probe location of 60 mm, which differs from the single inward probing scheme.

For both probing schemes, and for $M < 1385$ Nmm (99% of the buckling moment), the minimum critical probe work is attained in the middle of the structure and is extremely low. In an experiment, we suspect that initial imperfections would erode the critical probe work significantly, and as a consequence, the structure would never attain moments close to the buckling moment prior to buckling. Having said that, we can conclude that early buckling is most likely to be triggered by inward probing in the middle of the structure, and it is thus the critical disturbance. For this specific case, the probing and buckling location are the same. Therefore, the critical buckling mechanism consists of a localized single buckle in the middle of one of the two longerons. Finally, rotation-controlled simulations have been carried out, and the rotation-controlled critical probe work maps are presented in Section 2.7.

2.6 Stability landscape for critical localized buckling

The notion of a stability landscape of shell buckling was introduced [81] as a way to characterize the meta-stable nature of cylindrical thin-shell buckling. The original experiment accompanying this study used soda cans. A local radial displacement is imposed in the middle of the compressed can using a small ball probe (called "poker" in [81]). The stability landscape is the surface created when the probe force is plotted as a function of the probe displacement for various levels of the main loading parameter (axial compression or end-shortening of the cylinder). The landscape provides a very useful way to quantify the impact of probing on the buckling behavior and a general way to study the structure's buckling sensitivity to disturbances. In the cylinder case, the probe location coincides with the location of the critical buckling mechanism. As a reminder, this critical buckling mechanism corresponds to the formation of a single dimple in the middle of the cylinder and the probing experiment is aimed at triggering this specific mode (lowest mountain pass point). From the previous section, we were able to identify the critical buckling mechanism for the strip structure. Local buckling can first appear as a single inward buckle forming in the middle of one longeron. As a result we are now able to

construct the critical stability landscape of shell buckling for this new structure. This landscape is reported in Figure 2.19.

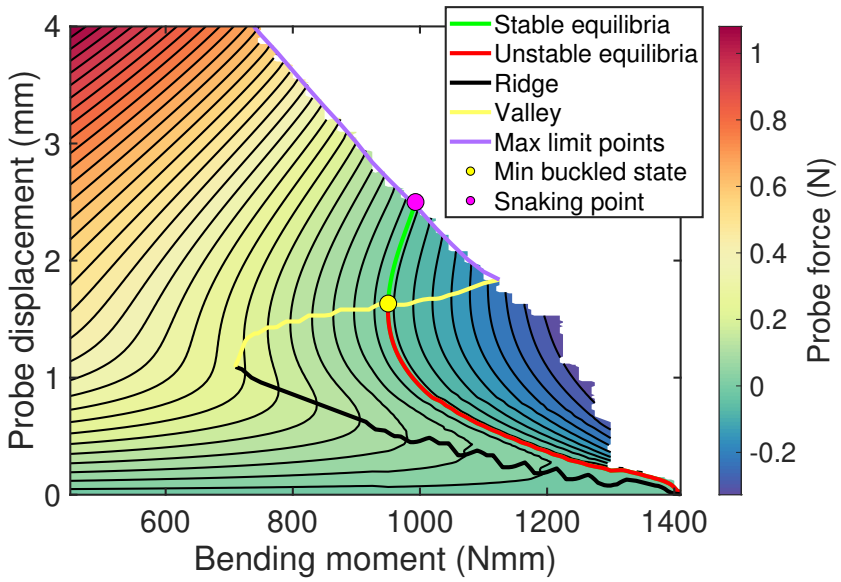

Figure 2.19: Stability landscape for the strip critical buckling mechanism (single inward buckling in the middle). It shows a region of negative probe force enclosed by a stable and an unstable buckled equilibrium contour, separated from the fundamental path by a ridge of probe force. The path restabilizes past the valley and additional buckling events are triggered through snaking when the maximum limit point contour is reached. No buckles can be sustained in the structure for moments below the minimal buckling moment (M = 950 Nmm).

This landscape matches qualitatively the one obtained for the compressed cylindrical shell, but also the stability landscape for more complex geometries and loading [69]. Several important features are observed and were previously noted in [81]. They are explained here. The point of spontaneous buckling corresponds to the state for which the structure will undergo buckling without any action from the probe (no probe displacement). This point is reached when the moment attains the buckling load (accounting for nonlinear pre-buckling deformation). However, before reaching this point, buckled equilibrium solutions are accessible through probing. These solutions correspond to the contour for which the probe force is zero (for a non-zero probe displacement). It is split into two parts: stable and unstable states. For a specific value of moment, the stable and unstable states coalesce. This condition corresponds to the lowest value of moment for which a buckled equilibrium solution exists, and thus represents the onset of meta-stability. The associated state is called the minimally buckled state [81], and we will refer to this moment value as the

minimal buckling moment for the rest of the chapter. For the strip structure, the minimal buckling moment is 950 Nmm (68% of the buckling moment), and the probe displacement at the minimally buckled state is 1.6 mm. Below the minimal buckling moment, no local buckles can be sustained in the structure. This load may serve as an effective lower bound for experimental buckling loads [23]. During a moment-controlled experimental probing sequence, where the probe is not attached to the structure, the longeron flange will dynamically snap as soon as the probe evolves past the unstable equilibrium contour, since the probe will experience negative reaction forces. Depending on the moment at which probing occurs, the structure can restabilize and reach the stable equilibrium contour. For a moment above a critical value, corresponding to the snaking point of Figure 2.19, the structure will not restabilize and will completely collapse. The snaking moment is $M = 993$ Nmm (71% of the buckling moment). It is possible to probe the stable post-buckling path and compute the critical probe work required for early snaking, following the same methodology. This will be the subject of a future study. However, it is important to realize that the existence of the stable equilibrium contour is not guaranteed, and depends on the structure but also on whether the experiment/simulation is load controlled or displacement controlled. For example, a spherical shell under external pressure will exhibit stable buckled states when loaded under volume-control but has no stable buckled states (other than complete collapse) under pressure-control [40]. In some cases, it has also been observed that the stable buckled equilibrium contour can extend much farther than the first buckling load [69]. Note that the unstable equilibrium contour stops at the buckling moment but does not intersect the fundamental path. This case is also encountered for the compressed cylindrical shell [23] and means that this "broken away" localized mode does not stem from a bifurcation and is rather considered as a mountain pass point, as introduced in Section 2.1.

The local maxima of probe force creates the ridge of the stability landscape, and forms a hill of energy between the fundamental path and the unstable buckled equilibrium states. At any applied moment, the critical probe work is the minimum energy that must be input into the structure for it to locally buckle. This quantity is directly related to the buckling sensitivity to disturbances, referred to as "shock-sensitivity" [76]. The ridge meets the fundamental path at the point of spontaneous buckling under prescribed probe force (but not under prescribed probe displacement). Past this point, negative probe forces are encountered as soon as the probe is displaced. The local minima of probe force forms the valley of the stability landscape, and is

the limit beyond which probing paths restabilize. The valley intersects the buckled equilibrium contour at the minimally buckled state after which the minimum probe force becomes negative. The ridge and valley intersect at $M = 710$ Nmm (51% of the non-linear buckling moment), after which the landscape starts exhibiting a negative probing stiffness. In a moment-controlled experiment for which the probe is not glued to the structure, kinetic energy would be released during probing, through snapping (for force controlled probing). For higher values of probe displacements, the stability landscape is bounded by limit points ending each probing sequence. The ridge, valley, and maximum limit points are forming the landscape's foldline which defines more generally the range of stability for the structure against the single buckle mode of deformation. Snaking, which corresponds to secondary modes being triggered, will occur when the maximum limit points are exceeded. Finally, rotation-controlled simulations have been carried out and yield qualitatively the same landscape. The rotation-controlled stability landscape is shown in the next section.

2.7 Rotation-controlled bending

The analysis presented in the chapter is repeated for a rotation-controlled main loading. Here the rotation is prescribed at the two ends of the strips, at the reference points shown in Figure 2.3. The moment-controlled and rotation-controlled studies lead to the same qualitative results. The same buckling modes and unstable probing paths are observed, and the critical probe work maps can be computed. These maps are shown in Figure 2.20a for the single inward probing scheme and in Figure 2.20b for the single outward probing scheme. The values of applied rotations are chosen such that they correspond one-to-one to the moment magnitudes in Figure 2.18, on the structure's fundamental path.

One important difference here is that the probe work accounts for all the external work since the end moments are not doing any work. For rotations (or corresponding moments) between 0.745 deg and 0.894 deg, a higher critical probe work is required to trigger snap-buckling when the loading is rotation-controlled rather than moment-controlled. In this initial range of rotations, the minimum critical probe work is still achieved by probing in the center ($Z = 200$ mm), and therefore the single inward buckling in the middle of one longeron is also the critical buckling mechanism for a rotation-controlled loading. For higher values of rotation, the critical probe work is higher for the moment-controlled case, even if it has a similar order of magnitude for both types of loading. Closer to the buckling point, we observe that the critical

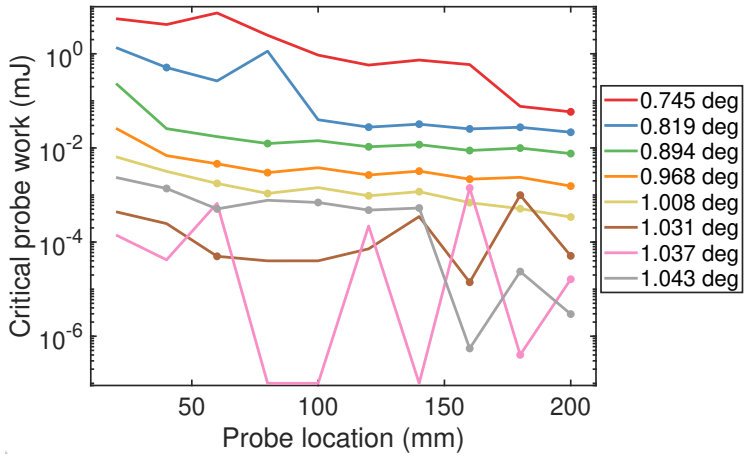

(a)

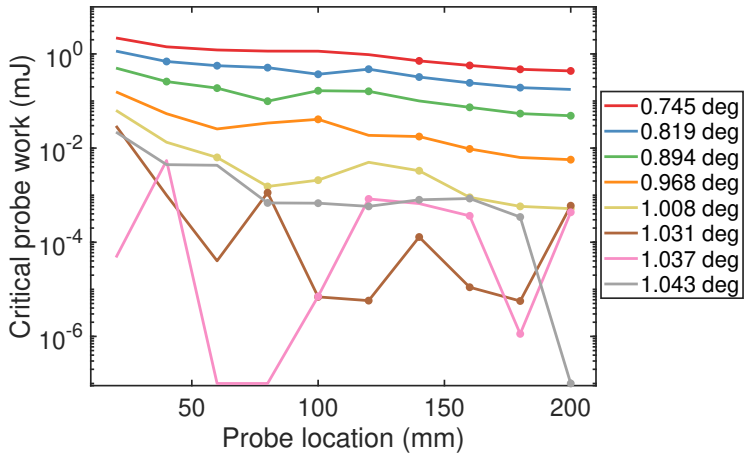

(b)

Figure 2.20: (a) Critical probe work map for the single inward probing scheme. When probing is achieved past the first zero threshold in probe force, a buckled equilibrium is detected and indicated by a dot. In some cases, secondary bifurcations are encountered on the probing path before reaching the zero probe force threshold. In this case, additional techniques need to be used to trace the full probing path. However, the critical probe work can be computed and is reported without a dot. (b) Critical probe work map for the single outward probing scheme.

probe work becomes chaotic across the structure's length.

For the critical buckling mechanism identified above (single inward buckle at Z = 200 mm), the rotation-controlled stability landscape can be built and is shown in Figure 2.21. It presents the same features as the moment-controlled stability landscape. In both studies, the probing path restabilizes after the minimally buckled state. The minimal buckling rotation is about 70 % of the classical buckling rotation which is comparable to the minimal buckling moment which was 68 % of the

classical buckling moment. Probing becomes unstable close to the snaking point which explains the missing area in the map shown in Figure 2.21. It is important to point out that when the applied rotation is held constant, the area under the probe force vs. probe displacement curve is the critical probe work but also the energy barrier between the unbuckled equilibrium and the unstable buckled equilibrium.

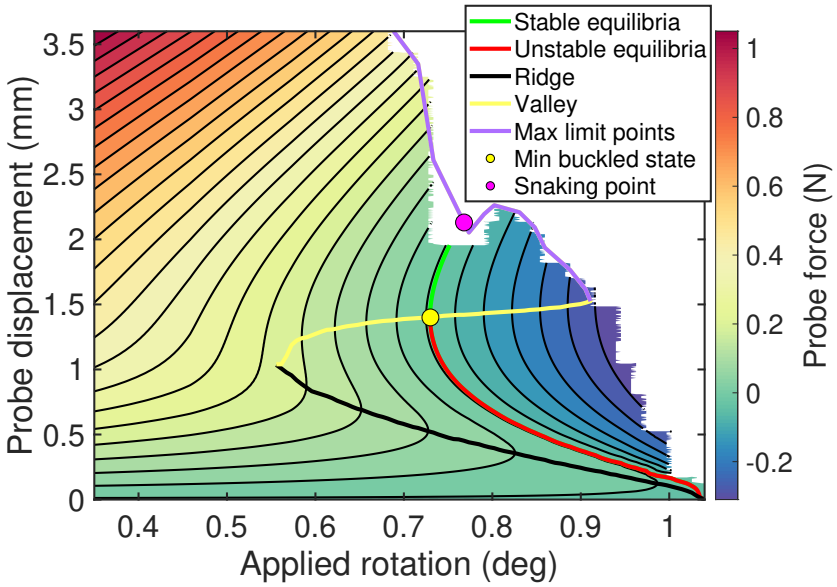

Figure 2.21: Stability landscape for the strip critical buckling mechanism (single inward buckling in the middle), and for a rotation-controlled loading. The same features as for the moment-controlled study are observed.

2.8 Conclusion

This chapter has presented a numerical analysis investigating the buckling sensitivity of a thin-shell strip structure, applying the novel probing methodology previously used for cylindrical and spherical shells. The focus has been on one single geometry, inspired from large spacecraft structures, with the goal of paving the way for the experiment of Chapter 4.

First, a classical post-buckling analysis has been conducted and consisted in seeding imperfections based on the structure's buckling modes in the initial geometry. It showed that from a limited set of 9 buckling modes, multiple localized post-buckling solutions arose, which suggested that the structure was exhibiting spatial chaos. Therefore, applying the probing methodology seemed particularly suited to finding the critical buckling mechanism. This new methodology has been extended to probe the entire structure and showed that only localized buckling in the inward direction can be triggered before the buckling moment is reached. Furthermore,

the comparison between single and double inward probing schemes highlighted that the longerons will most likely not undergo buckling simultaneously and will rather exhibit a sequential formation of buckles know as snaking, which was also supported by the classical post-buckling analysis. However, when the probing location does not coincide with the middle of the structure, incomplete probing sequences have been observed, for which instabilities are encountered on the probing path. Therefore, an arc-length solver was further used to resolve unstable probing sequences. It highlighted complex behaviors such as buckles traveling along the structure and multiple equilibrium paths juxtaposed next to each other. In addition, unstable outward probing also led to the creation of local inward buckling through complex interactions between components at the structure's level. The generalized probing approach enabled the construction of a critical probe work map from which we concluded that a single inward buckle forming on a single longeron was the buckling mechanism requiring the least amount of disturbance to be triggered before reaching the buckling moment. A further in depth study of this critical buckling mode enabled the construction of a stability landscape of shell buckling. It highlighted the region of stability for the buckled structure as well as the region for which restabilization occurs, between the minimal buckling moment and the snaking moment. The main observation is that this stability landscape is qualitatively similar to the one constructed for a previous cylindrical shell experiment. Although the core of the chapter presented results for a moment-controlled loading, for which probing occurs at constant moment, a rotation-controlled loading had also been studied and leads to the same qualitative results for this structure, shown in Section 2.7.

More generally, we have shown throughout this chapter that the probing methodology can be applied to more complex structures than the cylindrical and spherical shells. Therefore, the use of such a technique for complex assemblies of thin-shell components seems to be possible and could enable an in-depth understanding of any structure's buckling sensitivity. One could think about designing for a specific level of disturbance during operations and thus push the structure's capabilities to its fullest. If one does not have a full knowledge of potential disturbances, an experimental determination of the minimal buckling load seems to provide an excellent buckling criteria. However, more work needs to be done to assess how initial imperfections erode the critical probe work required to trigger buckling and how they could provide connections between the adjacent post-buckling path and the fundamental path. Recent studies suggested that the minimal buckling load varies extremely slowly for imperfections of limited amplitude (about 50 % of the shell

thickness) [69], even if the critical probe work is greatly affected. A thorough investigation of the role of imperfections on the buckling sensitivity will be the subject of a future study.

Chapter 3

ISOSTATIC PURE BENDING MACHINE FOR IMPERFECTION-SENSITIVE NONLINEAR STRUCTURES

3.1 Introduction

Three-point and four-point bending tests performed on universal testing machines are well established as a way of characterizing the behavior of materials and structures under bending. They are widely used to measure the bending stiffness and strength of stiff test samples, undergoing small deformations. Recent applications involving large bending deformations of compliant structures [5, 26], large-strain and ultra-thin flexible components for spacecraft structures have been accompanied by efforts to develop alternative testing setups. Our specific interest is in the deployment of ultralight spacecraft apertures [17] based on thin-shell structures that include tape springs and collapsible booms [27, 84], which can form localized folds with a small radius. The ideal test configuration for this type of structure is pure bending, with large imposed end rotations. Moreover, in the case of thin shells with geometric imperfections, any redundant constraints imposed on the sample may lead to a state of self stress if the structures' end mounts are not exactly aligned. In practice, the effects of this additional stress perturbation on the thin shell buckling behavior are significant, and would increase dramatically the apparent imperfection sensitivity of the test structure. Therefore, statically determinate boundary conditions are particularly relevant for the testing of non-linear thin-shell structures.

Different fixtures that can be mounted on a universal testing machine have been developed [16, 52, 56, 86] to characterize composite materials under large bending deformations. However, none of them can generate a state of pure bending in a sample of arbitrary geometry. Platen bending tests [52, 86] introduce normal and shear forces, and the effective length of the sample changes during the test. An improved version of these setups [16] can maintain a constant effective length but still introduces normal and shear forces, as well as additional loads due to the mass of the test fixture. These parasitic contributions create a more complex stress state than pure bending and are sensitive to missalignements in the testing apparatus, due to their redundant boundary conditions. A four-point bending fixture that can impose large rotations without any axial forces has been developed [9, 56]. The kinematic

diagram for this solution is presented in Figure 3.1c. However, a pure bending stress state is only obtained if the test sample deforms symmetrically and therefore if its material and geometric imperfections are negligible. This architecture is statically indeterminate and initial geometric imperfections will induce an initial state of self stress in the sample.

Special-purpose, pure bending machines have also been developed, often based on pulleys and cables [14, 15, 30, 46]. In the design presented in [46], each end of the sample is attached to a pulley, and a cable links the two pulleys ensuring two equal reaction moments on both sides. The cable shortening can be imposed by an actuator, causing the pulleys to rotate. The use of rollers in conjunction with the cable and pulleys prevents any axial forces to appear. A kinematic diagram of this testing apparatus is shown in Figure 3.1a. Identical setups were employed in [14, 15] and a similar concept is also proposed in [30, 55, 61]. However, these machines are primarily used for the testing of very large and stiff samples for civil engineering applications. In addition, even if the degree of indeterminacy is lower than for the machine of Figure 3.1c, this architecture is still statically indeterminate.

Another type of machines eliminates external forces by employing linear guides [11, 31, 49, 87] so that only a bending moment can be applied to the structure. In the concept by [87], one sample end is resting on two perpendicular linear guides which allows it to translate in plane. The other sample end is rotated by a motor. The kinematic diagram for this machine is shown in Figure 3.1d. This architecture reduces the magnitude of in-plane reaction forces, which can only arise from friction in the sliders. The concept presented in [11] uses a similar architecture and is illustrated in Figure 3.1e. It uses two perpendicular linear guides, on which the sample's ends are attached. One end is rotated relative to the corresponding linear guide by a motor. The sliders on each guide are allowed to translate without friction, which suppresses all in-plane reaction forces. They are also allowed to rotate about the guide's axis to suppress parasitic reaction moments. This testing apparatus has only a degree of indeterminacy of 1, stemming from the redundant constraint on the vertical translation of the sample. However, this machine is large and is best suited for relatively stiff samples. The pure bending machine presented in [49] and illustrated in Figure 3.1b is used for the testing of softer thin-shell samples. It uses only one frictionless linear guide, and during testing, special care needs to be taken to balance the reaction moments at the ends to avoid shear reaction forces at the two sample ends. Doing so requires a careful coordination between the two end

rotations, which is difficult if the test sample becomes unstable. A machine similar to [11], but suitable for much smaller and softer samples, was designed in [31], but not realized. A suspension system removing all external forces is presented in [2] and uses two overlapping identical samples. The two samples are bent in opposite directions by actuators. In this concept, pure bending is only achieved if the properties of the two samples are identical.

Imperfection-sensitive structures and non-linear structures undergoing buckling or snap-through are hard to study, and are particularly sensitive to boundary conditions, as discussed earlier. Even if the testing apparatus described above is extremely suitable for the testing of plate coupons and stiff structures, a fully isostatic pure bending apparatus dedicated to the testing of thin-shell components does not exist yet. This chapter presents the design of a new bending machine that uses the concept presented in [11] as a baseline, and releases the redundant constraint by employing an additional slider in the vertical direction, as illustrated in Figure 3.1f. It results in an isostatic system generating a state of pure bending in the test sample, regardless of its geometric or material imperfections. This new machine enables the testing of ultra-thin materials and softer structures with complex cross-sections [17], needed for modern aerospace applications.

The chapter is structured as follows. Section 3.2 discusses the impact of redundant boundary conditions for testing thin-shell structures, and Section 3.3 presents the physical implementation of the bending machine. Its stiffness is then assessed through experiments on stiff tubes in Section 3.4, and Section 3.5 analyzes the testing machine's performance and its parasitic effects, through experiments on circular rods. Testing is then extended to tape springs in Section 3.6, and the interaction between kinematic constraints and sample imperfections is analyzed using finite element simulations in Section 3.7. Finally, Section 3.8 concludes and presents an outlook of future experiments rendered possible by this new testing setup.

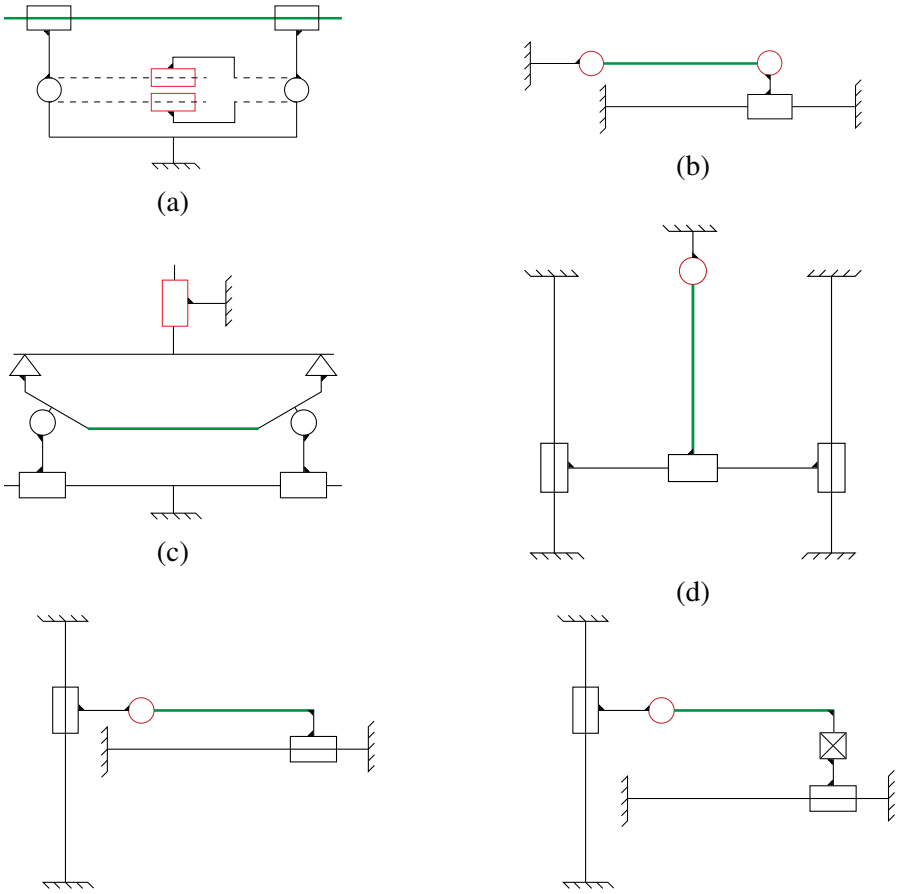

(a)

(b)

(c)

(d)

(e)

(f)

Kinematic pair name	y z	y x	Degrees of freedom
Cylindrical			Uz, URz
Revolute			URz
Prismatic			Uz
Cylinder-plane			Uy, Uz, URx, URy

(g)

Figure 3.1: Kinematic diagrams for various bending machine concepts. The bold green line represents the test samples, and the kinematic pairs indicated in red are actuated. The diagrams are drawn in the (X-Y) plane and the bending axis coincides with the Z-axis. (a) Apparatus from Kyriakides et al. The dashed line represents a chain coupling two revolute kinematic pairs. (b) Bending machine from Fisher et al, (c) Murphey et al, (d) Yoshida et al., (e) Boers et al and (f) the new bending machine described in the present chapter. (g) Definition of the kinematic pairs used in the kinematic diagrams and their degrees of freedom. The symbols are based on [42].

3.2 Eliminating redundant constraints

The purpose of the new bending machine is to test thin-shell structures under large deformations, and to predict accurately their buckling and post-buckling behavior. One important feature of such structures is that they exhibit an unstable post-buckling regime, and therefore, the pre-buckling state is metastable close to the buckling load. A small amount of energy input into the system can therefore force the structure to transition in its post-buckling regime before the theoretical buckling load is reached. If the testing apparatus is statically indeterminate, geometric and material imperfections can also perturb the pure bending stress state and affect significantly the buckling transition. Another challenge arises from the study of structures with non-symmetric cross-sections, or for which the stable mode of deformation is non-symmetric. In this case, the structure will undergo large 3D deformation under pure bending. If the boundary conditions restrain the displacement of the end cross-sections relative to one another, large reaction forces and moments can arise perpendicular to the bending axis. The structure will no longer be under pure bending and its behavior will be influenced by statically indeterminate reaction forces and moments at the supports. If boundary conditions can be modelled accurately, simulations will in theory enable capturing these statically indeterminate reactions. However, the test results become more sensitive to the structures' initial imperfections and its mounting into the testing machine. Therefore, it requires adjustments to guarantee a structure free of self stress throughout the test, which in practice may only be achieved by having no redundancy in the boundary conditions. This important characteristic is studied in depth in [47], where the authors analyze the buckling of a cylindrical shell under compression. The two shell's end cross-sections are held using friction, which in effect provides statically determinate support conditions at high loads, allowing the end cross-sections to be non-planar. Furthermore, the researchers introduced initial stresses by locally displacing the one end cross-section, highlighting that the shell's apparent imperfection sensitivity was limited by the use of isostatic boundary conditions. Other studies focused on other types of boundary conditions and showed how the constraints imposed by the testing apparatus influence the structure's sensitivity to buckling [21]. We wish to address and justify here the choice of boundary conditions for the new bending machine. We discuss successively the role of in-plane ($X-Y$ plane) constraints on translations and rotations, and will touch upon the release of the out-of-plane translation constraint, in order to create a statically determinate (isostatic) testing apparatus.

Reaction forces aligned with the test structure's neutral axis have a large influence on

its stress state. Parasitic compressive or tensile stresses are respectively reducing or increasing the buckling moment significantly. It is therefore important to remove any redundancy in translational constraints along the sample's longitudinal axis. This condition is met by all designs presented in Figure 3.1. Translational redundancy transverse to the sample longitudinal axis can create shear forces at the structure's supports, and this effect is for instance observed if the two bending moments at the sample ends are imbalanced. In the design presented in Figure 3.1b, the two end rotations are controlled independently and the bending moments can be matched in theory, but is hard to achieve in practice. In the design of Figure 3.1a and 3.1c, the single degree of freedom actuation results in two equal and opposite bending moments only if the tested structure is close to perfect. Quantifying the parasitic effect generated by shear forces is hard in practice due to the testing machine's static indeterminacy. To avoid any parasitic contributions from in-plane forces, the designs in Figure 3.1d and 3.1e employ two perpendicular linear bearings which remove any in-plane redundancy in translational constraints.

The effect of redundant rotational constraints is harder to analyze but is particularly important for imperfect thin-shell structures. Recent advances in spacecraft structures uses very thin and complex composite booms [48]. Even though these components are designed to be straight along their longitudinal axis, they exhibit residual twist and camber after manufacturing, and the two end cross-sections are often non coplanar. If the coplanarity of the end cross-sections is enforced through fixed rotation boundary conditions, it can induce a significant amount of prestress in the test structure. One potential solution is to have custom end fittings which compensate for these geometrical imperfections. However, the test results become extremely sensitive to the position accuracy provided by these additional components. In addition, if the test structure exhibits significant off-axis deformations, any rotational constraint redundancy can create significant parasitic reaction moments and a complex stress state in the structure. The impact of rotational constraints on imperfect tape spring structures is analyzed in details through simulation in Section 3.7. To avoid any parasitic moments and self stress, the design presented in Figure 3.1e, employs a similar concept to Figure 3.1d, but the prismatic joint between the sample and the linear guide is replaced by cylindrical joint, which releases the rotational degree of freedom along the guide's axis. This architecture removes all redundant rotational constraints' redundancy, and the same architecture is adopted in the present bending machine.

One redundant constraint in the apparatus of Figure 3.1e makes it statically indeterminate. The out-of-plane (z-axis) translations of both sample ends is constrained. In the physical implementation presented in [11], the sample is hanging below the plane formed by the two linear guides. As a result, the rotation of one sample end around its linear guide's axis results in a change of its z-coordinate. Compatibility of displacements requires that the two ends have the same z-coordinate and therefore, the rotation of both ends needs to be equal. For flat material coupons, deformations transverse to the main bending axis have very limited amplitude, and coupling between the two end rotations may not be a concern. However, for complex structures undergoing large 3D deformations, a coupling between global torsion and bending transverse to the main bending axis arises, which creates a very complex stress state and is hard to model accurately. In the design presented in this chapter, this coupling is removed by adding a slider in the z-direction at one sample end, and the resulting boundary conditions are statically determinate. The machine's kinematic diagram is shown in Figure 3.1f, and the boundary conditions are explicitly stated in Figure 3.2.

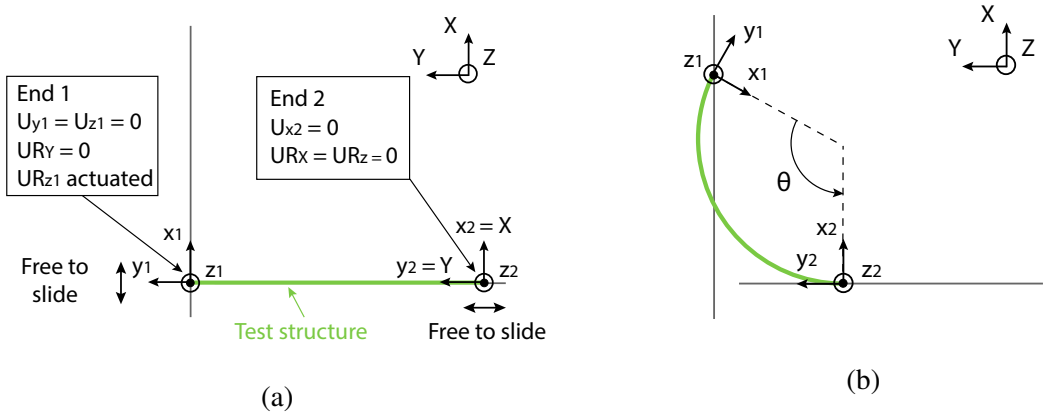

Figure 3.2: Conceptual representation of the bending machine, specifying the boundary conditions on the two ends of the sample. (a) Undeformed configuration and (b) deformed configuration after a rotation of θ is applied to end 1. U corresponds to the translational degree of freedom and UR to the rotational degree of freedom. In a previous concept [11], Uz was constrained for end 2. This constraint has been released in the present bending machine. The local coordinate systems attached to end 1 and end 2 are shown as well as the global coordinate system.

3.3 Design of the bending machine

The bending machine employs two perpendicular circular rods in the $X-Y$ plane, similarly to the setup presented in [11]. They form two linear guides on which two air bearings are allowed to translate and rotate. As explained in Section 3.2, this architecture suppresses all in-plane reaction forces and moments during the test, and prevents any self-stress in the test structure. The pressure in the air bearings is 90 psi. Several components are attached to each air bearing, and we refer to this assembly as a slider. The actuated slider, on which one end of the test structure is attached (end 1, see Figure 3.2), is made of a DC motor (Harmonic Drive FHA-8C) which controls the rotation of the sample around the local z-axis. An incremental encoder with a resolution of up to $800,000$ counts per revolution measures the applied rotation. A sensor (ATI Mini40) is attached to the motor's rotating end and measures the three reactions force components with a resolution of $1/100$ N and the three reaction moment components with a resolution of $1/4000$ Nm. These sensors can measure in-plane forces up to 40 N, out-of-plane forces up to 120 N, and moments up to 2 Nm. An aluminum bracket is mounted on the sensor and provides and interface to attach the test structure. The second end of the test structure (end 2, see Figure 3.2) is attached to the rigid slider, where the DC motor is replaced by an aluminum column. An offloaded bracket allows the sample to translate along the slider-local z-axis. It uses a hanging mass and a pulley, which compensates for half of the mass of the test structure and half of the mass of the bracket's translating assembly. To avoid parasitic moments caused by gravity, a counterweight is attached to the top of each slider and can be translated to adapt to a wide range of sample mass. A CAD model of the bending machine is shown in Figure 3.3. A custom Matlab code was developed to read, display, and record the forces, moments, and rotations in real time. The rotation of end 2 can be applied both as a ramp or as a smooth s-curve, and the maximum angular acceleration can be chosen to limit dynamic effects. Note that the apparatus is mounted on an optical table and the spacing of the circular rods can be varied to accommodate a wide range of sample lengths and applied rotations. The height of the table is adjusted using spacers. The physical implementation of the machine is shown in Figure 3.4.

3.4 Experimental setup compliance assessment

The two main quantities of interest for a pure-bending test are the bending moment around the z-axis and the rotation applied to the test structure. These quantities can be affected by any torsional compliance in the sliders. It is then critical to measure the

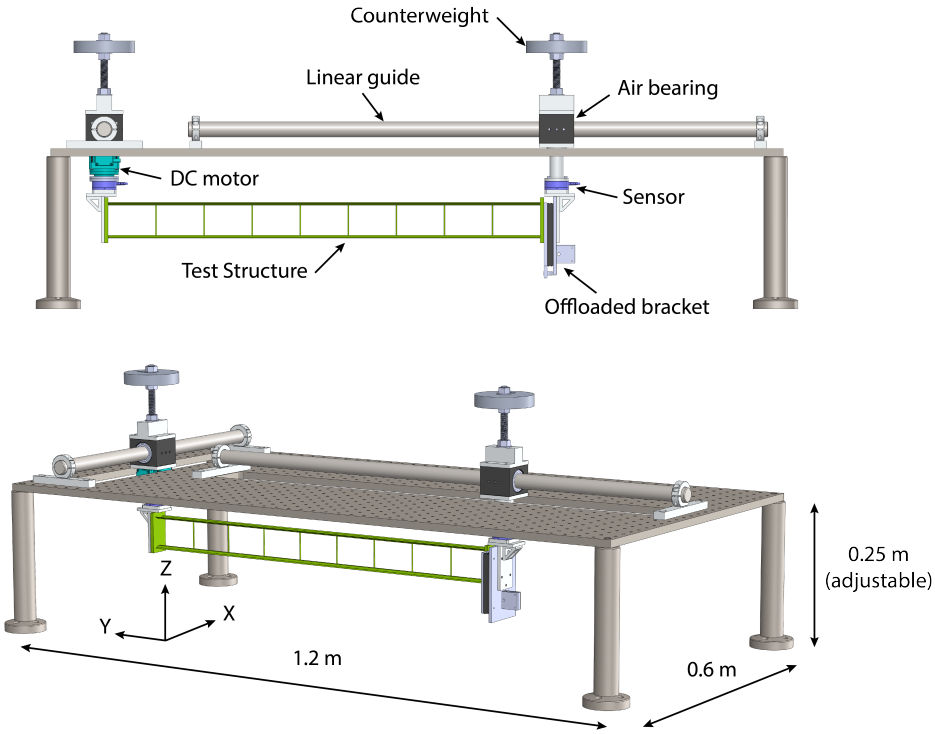

Figure 3.3: CAD of the bending machine. Two frictionless linear guides are mounted perpendicular to each other on an elevated optical table. Two sliders are suspended on these linear guides and the moment caused by gravity is eliminated by using counterweights. One slider assembly is made of a DC motor and sensor while the other slider features an offloaded mounting bracket and a sensor.

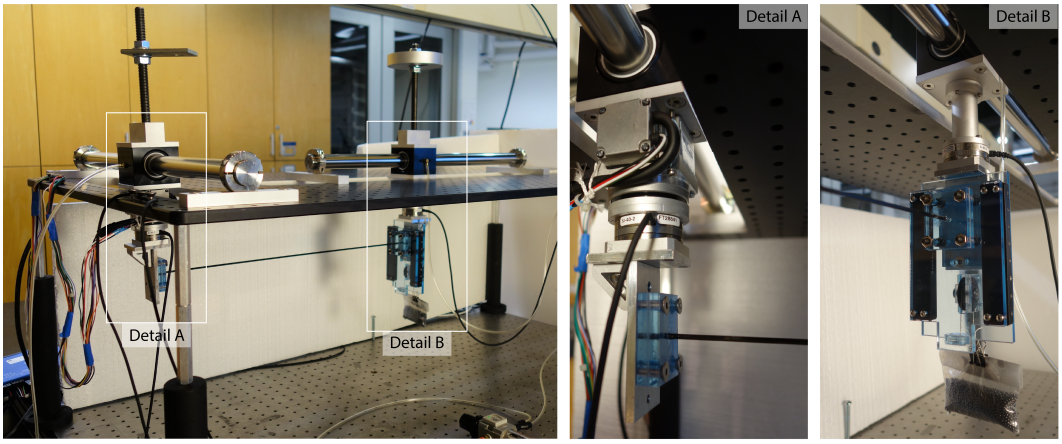

Figure 3.4: Physical implementation of the bending machine. Here the test structure is a carbon fiber rod, corresponding to the test described in Section 3.5.

torsional stiffness of each slider and to understand the impact it has on the test results. The compliance of the experimental setup can then be included in simulations. In

order to measure it, a very stiff tube, shown in Figure 3.5 is attached to the machine. The tube geometry is chosen such that it is orders of magnitude stiffer than any samples that would be tested with the machine, and the tube can be considered rigid in the analysis. When the motor is actuated, the tube rotates as a rigid body, resulting in the twisting of both sliders. The twisting moment is measured for both sliders and the rigid body rotation of the tube is determined experimentally using a laser scanner (FaroArm). The tube and apparatus are represented in their deformed configuration in Figure 3.6b. The measurements are repeated every rotation increment of 0.1 deg until an absolute rotation of 0.9 deg is reached. The twisting angle of both sliders is determined. For the rigid slider, the equivalent twist is simply the rigid body rotation of the tube, whereas for the actuated slider, the equivalent twist is the difference between the applied rotation and the tube rotation.

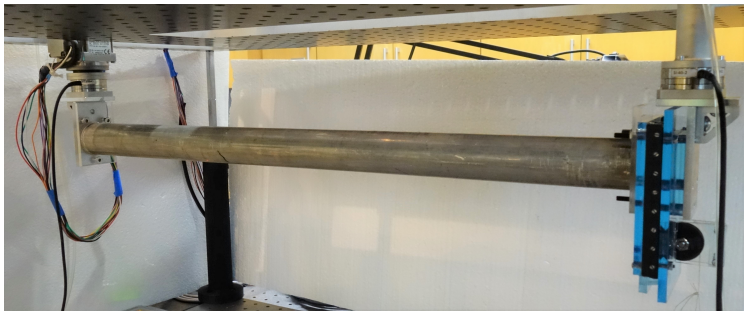

Figure 3.5: Stiff tube mounted on the bending machine. This test sample is used to determine the torsional stiffness of both sliders.

The reaction moment plotted as a function of the equivalent twist for both sliders is shown in Figure 3.6a. The rigid slider appears to be softer in torsion than the actuated slider. This can be explained by the presence of the offloaded bracket on the rigid slider, which is partially made of acrylic and therefore softer than the rest of the components made of aluminum. The sliders' torsional response can be considered linear up to a reaction moment of 0.7 Nm. The complete response could best be described as bi-linear. A linear fit is shown in Figure 3.6a for reference. The softer behavior can be due to a local deformation between the tube and its end mounts, and may not be representative of the sliders' torsional stiffness. Therefore, for the rest of the chapter, a linear fit between a rotation of 0 and 0.2 deg is considered. The resulting torsional stiffness is 203 Nm for the rigid slider and 301 Nm for the actuated slider.

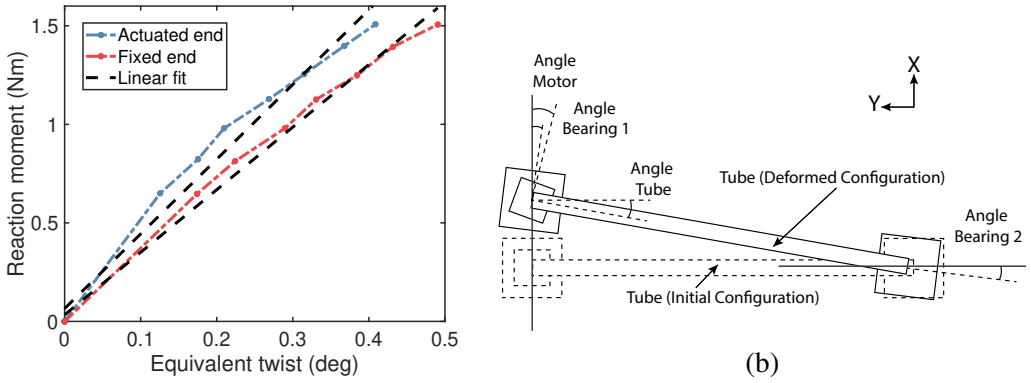

(a) (b)

Figure 3.6: Compliance assessment test performed with a rigid cylinder. (a) Bending tests results for a rigid cylinder. A linear fit is shown which is used to compute the torsional stiffness of each slider assembly. (b) Schematic of the rigid tube test. An equivalent twist can be defined and takes for arguments the angles indicated in the figure.

3.5 Machine accuracy and parasitic effects

To assess the accuracy of the bending machine, an initial set of bending tests was performed on 3 circular carbon fiber rods. 2 cross-section diameters are considered, $d = 2.88$ mm and $d = 3.19$ mm, as well as 2 different lengths, $L = 581$ mm and $L = 446$ mm. Each rod end was inserted and bonded into an acrylic plate, which attaches to the machine's brackets. For each rod, 3 loading and unloading sequences were performed and the 3 reaction moments and reaction forces were measured by the sensors. The result of a specific test, performed on a rod of diameter $d = 3.19$ mm and length $L = 446$ mm, is shown in Figure 3.7. For this particular test, a S-curve rotation profile is prescribed with a maximum angular velocity of 0.1 deg/s, and the maximum rotation is set to 10 deg. The sensors are zeroed after the sample is mounted on the machine.

The bending moments M_{z1} and M_{z2} are linear for the entire range of rotations considered. Even if some oscillations are noticeable, their amplitude is negligible compared to the global linear trend. However when looking at in-plane moments (Figure 3.7b) and forces (Figure 3.7d), as well as out-of plane forces (Figure 3.7c), oscillations of larger amplitude are observed. This behavior is not caused by noise in the sensors but rather by the physical oscillation of the two sliders. The bending machine is equivalent to a system of two pendula coupled by a soft spring. Each pendulum has its own mass, natural frequency, and plane of oscillation. The resulting mechanical coupling creates a beating phenomenon (amplitude modulation) and

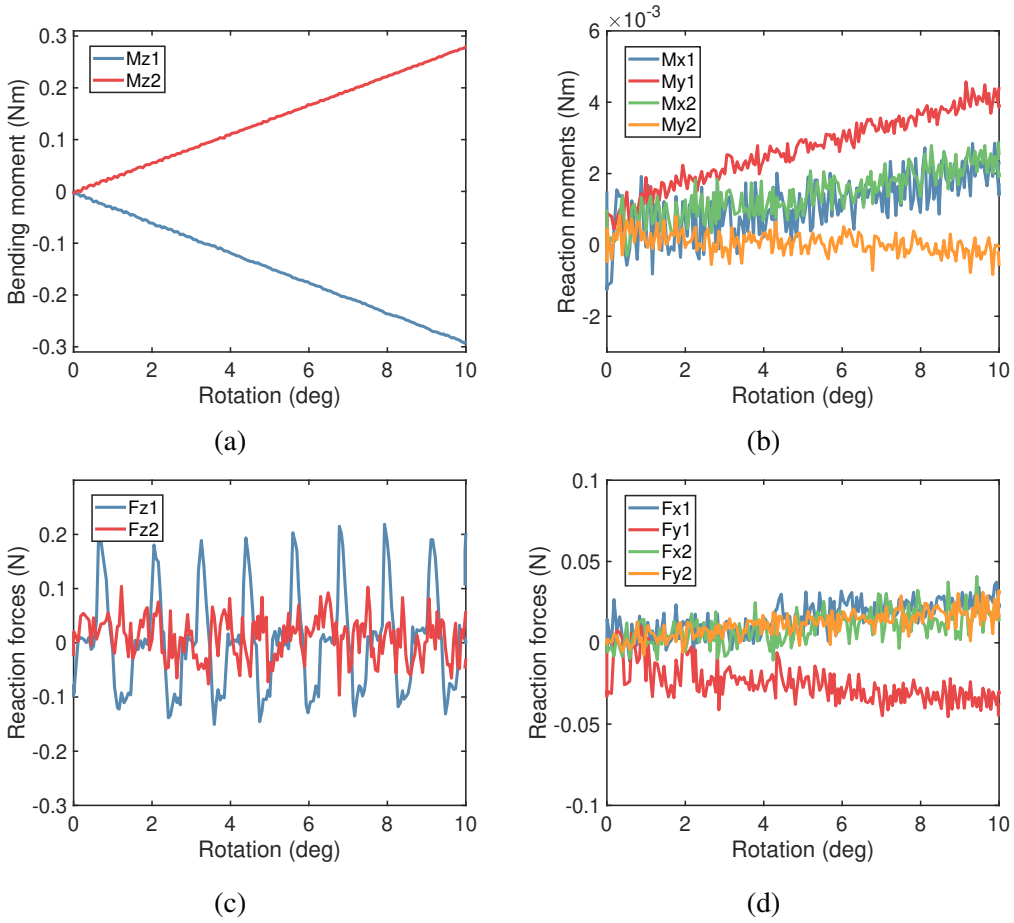

Figure 3.7: Test results for a rod with diameter $d = 3.19$ mm and length $L = 446$ mm. The maximum angular velocity for this specific test is set to 0.1 deg/s. The reaction moments and forces are measured in the deformed reference frames attached to end 1 and end 2, described in Figure 3.2. (a) Main bending moment around the z axis, (b) reaction moments around the x- and y-axes, (c) reaction forces on the z direction and (d) reaction forces on the x- and y-axes.

explains the complex oscillatory profile observed for the out-of-plane forces. In practice, the range of slider rotation characteristic of this oscillatory behavior is extremely limited and is barely noticeable by eye. A series of tests has been performed on the same rod sample with various maximum angular velocities. A plot of in-plane bending moments for a maximum velocity of 0.01 deg/s and 0.6 deg/s is shown in Figure 3.8. In the case of Figure 3.8b, the test duration is about 17 min, whereas it is about 17 s in Figure 3.8a. Since the natural frequency of the coupled pendula does not change, the data appear more noisy for the longer duration test. However, the maximum angular velocity does not influence the results as long as the test can be considered quasi-static.

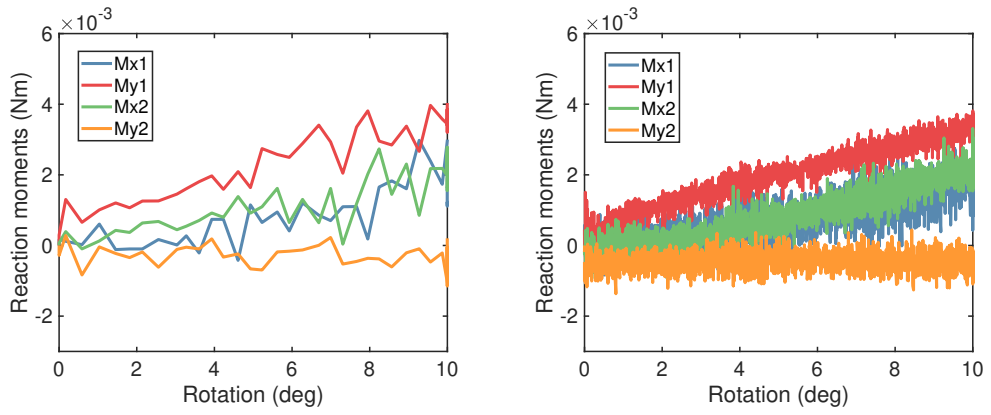

Figure 3.8: Test results for a rod with diameter $d = 3.19$ mm and length $L = 446$ mm for a maximum angular velocity of (a) 0.6 deg/s and (b) 0.01 deg/s.

Three tests are performed on the rod of diameter $d = 3.19$ mm and length $L = 446$ mm, with a maximum angular velocity of 0.01 deg/s. The results of these tests are shown in Figure 3.9. The mean of the three tests is computed and filtered using a moving average filter. The area corresponding to test data within one standard deviation is also reported for the three bending moments and forces. The spread of the data is caused by the oscillatory behavior explained above, and we mostly discuss here the trends followed by the mean moments and forces. As observed before, M_{z1} and M_{z2} (Figure 3.9a) are linear, and their standard deviation is extremely small.

The in-plane forces are more complex to analyze. F_{x1} and F_{y2} (Figure 3.9d) follow a linearly increasing trend. These reaction forces are along the linear guides' axes. In theory, the air bearings make the guide frictionless, and therefore the axial reaction forces would be zero. However in practice, the presence of cables and air tubes, seen in Figure 3.4, creates these non-zero reaction forces. During the test, both sliders undergo a small rotation around their guides' axes, due to small imperfections in the sample. As a result, the sensor's local z-axis is no longer aligned with the local vertical, and part of the slider's weight is projected onto the linear guide's transverse axis. This geometric effect creates the F_{y1} and F_{x2} reaction force components. Note that as the test progresses, the tilt of each slider increases and therefore the weight projection increases in magnitude as well, which explains the linear trend followed by these forces. These reaction forces also have a separate component that partially equilibrates F_{x1} and F_{y2}. The out-of-plane forces F_{z1} and F_{z2} (Figure 3.9c) also follow a linear trend, caused by the slider tilt.

The cables and slider tilt are also responsible for the in-plane moments observed in

Figure 3.9b. The offset between the cables and the sliders' axes of rotation creates the moment components M_{x1} and M_{y2}. It is important to mention that the rigid slider only has one cable connecting to the sensor and one air tube connecting to the bearing, while the actuated slider has a significant amount of additional cables connecting to the DC-motor. For this reason, M_{y2} is almost zero for the entire range of rotations whereas M_{x1} has a larger amplitude. The linear increase can be explained by the shift in the cable bundle's center of gravity and therefore changes the magnitude of the reaction moments. The out-of-plane forces create moment components M_{y1} and M_{x2}. When the slider tilt increases linearly, the magnitude of M_{y1} and M_{x2} also increases linearly.

In conclusion, the parasitic reaction forces and moments measured by the sensors are caused by two effects: the presence of cables and the the tilt of the sliders during the test. However these effects do not significantly affect the accuracy of the main bending moment measurement, and therefore the performance of the bending machine, as discussed next. Improvement in the handling of the cables can be made, but it was not deemed necessary for the type of structure we are looking at.

Next, the test described above was repeated three times for each rod sample, and their bending stiffnesses were computed, based on the average of M_{z1} and M_{z2}. In addition to the tests on the new bending machine, 3-point bending experiments were conducted on the same samples, and the bending stiffnesses obtained by the two methods are compared, see Table 3.1. A good agreement is observed between the two tests, with a relative error under 2 % for all samples. The discrepancy between the two tests can be attributed to 3 factors: the cables, the slider tilt and the slider torsional compliance. Since the latter has been characterized in Section 3.3, its effects are included into a finite element simulation, where the rod model is connected to two torsional springs of equivalent stiffnesses. The relative error between the bending machine experiment and the simulation is under 1 % for all samples. Qualitatively, the torsional compliance of the sliders reduces the rod's apparent bending stiffness. This effect is more significant for the shorter and thicker rod, for which the bending moments are higher than for the two other samples. The remaining discrepancy is attributed to the cables and slider tilt, and these effects are more dominant for longer and/or softer samples. However, these parasitic effects are very limited and are not a concern here. These initial tests revealed that the performance of the new bending machine is satisfactory for linear structures, and will next be assessed for more complex tests on non-linear thin-shell components.

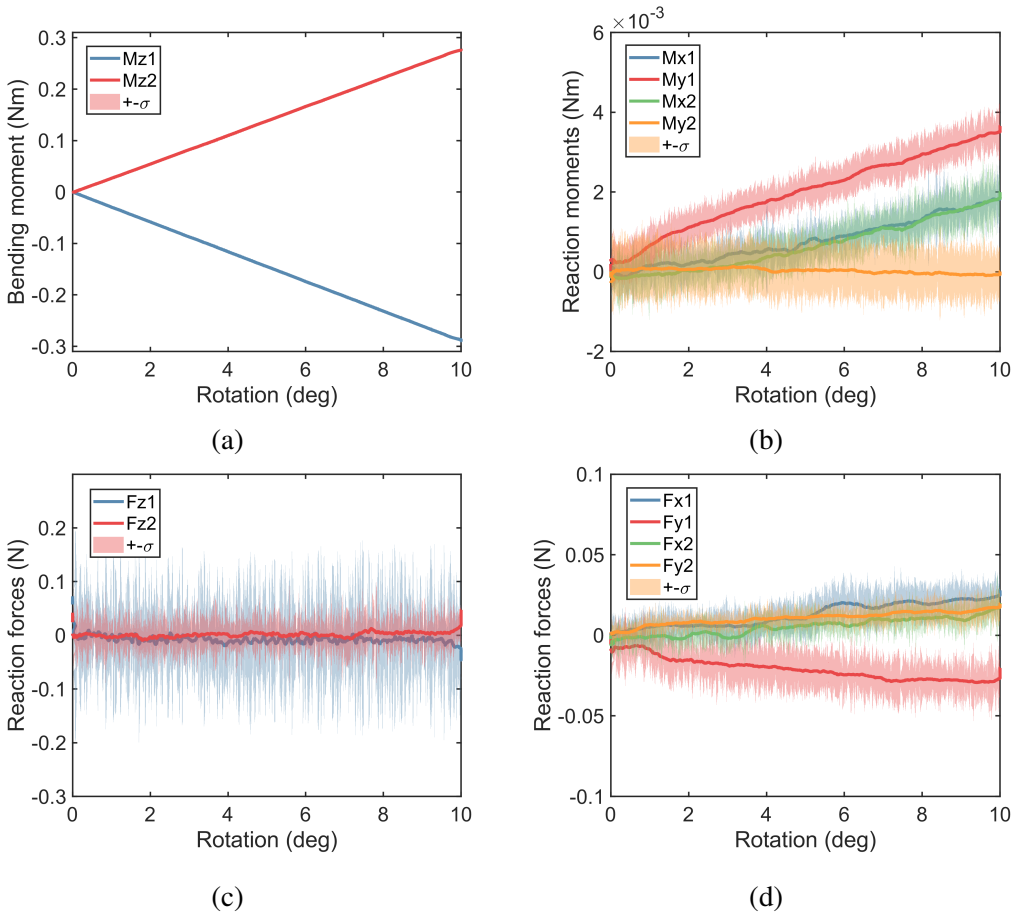

Figure 3.9: Test results for rod sample 2 (d = 3.19 mm and L = 446 mm). The reaction moments and forces are measured in the deformed reference frames attached to end 1 and end 2, described in Figure 3.2. (a) Main bending moment around the z axis, (b) reaction moments around the x- and y-axes, (c) reaction forces on the z direction and (d) reaction forces on the x- and y-axes.

	d = 3.19 mm L = 581 mm	d = 3.19 mm L = 446 mm	d = 2.88 mm L = 446 mm
Methodology	Rod bending stiffness, EI (Nm)		
3-point bending	0.736	0.736	0.354
Simulation	0.738	0.723	0.357
Experiment	0.742	0.729	0.360
Reference	Experiment relative error on EI (%)		
3-point bending	0.912	-0.964	1.602
Simulation	0.541	0.824	0.754

Table 3.1: Measured bending stiffness for 3 carbon fiber rods. The first row corresponds to a 3-point bending test performed on a universal testing machine (Instron). The second row corresponds to finite element simulation, taking into account the sliders' torsional stiffness found in Section 3.3. The third row corresponds to the tests preformed on the new bending machine. Finally the relative error between the new bending machine experiment and the 3-point bending experiment is reported in the fourth row and the relative error between experiment and simulation is reported in the fifth row.

3.6 Non-linear structures: tape springs

The main propose of the new bending machine is to test non-linear thin-shell structures and to study their instabilities. One such structure, used as a building block for more complex thin-shell deployable components, is the tape spring, which has been studied extensively [73]. It captures all the important features of the thin-shell behavior: unstable buckling, imperfection sensitivity, and localization of buckling modes. In this section, a series of tests on a short tape spring are carried out. The tape spring cross-section is described in Figure 3.11 and has a length of 215 mm. The tape spring is made of stainless steel and has a thickness of 110 μm. The sample's Young's modulus has been measured to be $E = 208$ GPa and its Poisson's ratio is $\nu = 0.3$. Each end of the tape spring is glued into an acrylic plate in which the nominal cross-section is cut. The sample attached to the bending machine is shown in Figure 3.10.

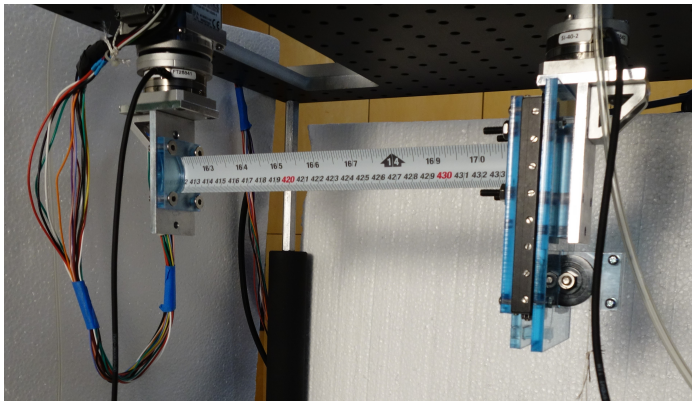

Figure 3.10: Tape spring attached to the bending machine.

In addition, a finite element analysis is conducted, using the Abaqus Standard software. The finite element model is detailed in Figure 3.11. The tape spring is meshed using 1 mm x 1 mm reduced integration shell elements (S4R), and its end cross-sections are held rigid and offset from the linear guide, similar to the experimental setup. They are coupled to two cylindrical joints representing the linear guides, which are implemented in Abaqus using boundary conditions. To model the compliance of the sliders, the two cylindrical joints are attached to two torsional springs whose stiffnesses have been determined in Section 3.4. For the rigid slider, the other end of the torsional spring is clamped, whereas it is rotated in the case of the actuated slider. The bottom edge of the experimental tape spring has a slight camber (maximum deflection less than 0.5 mm), and the tape spring

also exhibits a small twist (less than 1 deg). Both effects are included in the finite element model. An arclength solver (modified Riks method in Abaqus) and a Newton Raphson solver (Static general in Abaqus) are both used.

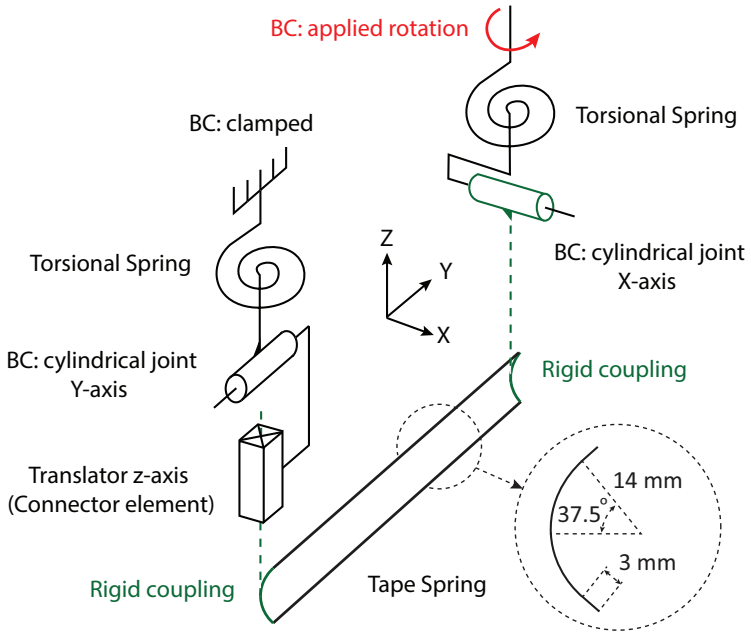

Figure 3.11: Sketch of the tape spring finite element analysis. BC refers to the application of boundary conditions in Abaqus. The rigid coupling is introduced using an Abaqus constraint and the z-axis translator is implemented using a connector element.

Equal sense and opposite sense bending tests are conducted, and their full loading and unloading characteristics are reported in Figure 3.12. For each bending sense, 3 tests have been conducted and the mean and standard deviation are shown. The opposite sense bending moment vs. rotation curves matches previous work on tape springs [72], in the case of loading and unloading. The structure exhibits a uniformly bent shape early in the test and the deformation quickly localizes in the center of the tape spring, where the cross-section flattens and forms a localized fold of uniform curvature. When unloading, the fold disappears at a lower rotation than the one for which the snap-through occurs. Here, the well-known hysteresis behavior is not affected by the new boundary conditions provided by the bending machine. The finite element analysis captures well the experimental response. The Riks solver diverges on the unstable part of the path, and a static solver with numerical damping (10^{-8}) is used to continue after the point of vertical tangency. Both peak and steady-state moments are accurately predicted by the simulation. The deformed

shape obtained from the experiment and the finite element simulation are in good agreement and are shown in Figure 3.13.

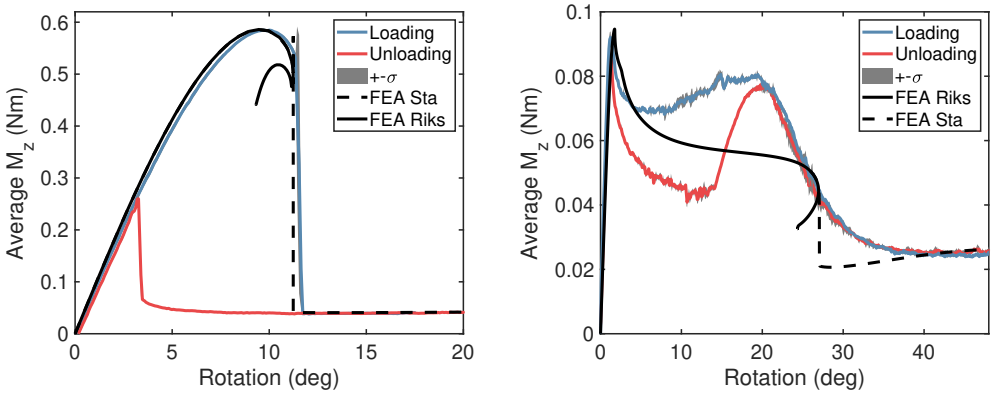

(a) (b)

Figure 3.12: Results of the (a) opposite sense bending tests and (b) equal sense bending tests of the tape spring sample. For each bending sense, 3 tests have been conducted, and the mean of the 3 tests is plotted as well as an grey envelope corresponding to one standard deviation around the mean. Finite element analyses are reported in black. The solid line corresponds to an analysis using an arclength solver whereas the dashed line uses a Newton Raphson solver.

(a) (b)

Figure 3.13: Tape spring deformed shape obtained for the opposite sense bending test. (a) Experimental deformed shape and (b) finite element deformed shape. The color map corresponds to the distribution of the Von Mises stress, but it used here solely for visualization purposes.

Contrary to the opposite sense bending, for which a snap-through destabilizes the structure, the structure under equal sense bending traverses a series of bifurcations. Equal sense bending is therefore more unstable than opposite sense bending, and the results are extremely sensitive to imperfections and disturbances. For a perfectly straight tape spring, the top and bottom edges would exhibit symmetric deformations. However, in practice, this mode of deformation is never observed and a torsional instability appearing at the peak moment breaks this symmetry. The boundary conditions specific to the present machine do not prevent global torsion to arise, contrary to previous tests [72], and therefore changes the behavior of the structure

after the peak moment is reached. The deformed shape observed in the experiment is shown in Figure 3.14a. When the peak moment is reached, a single kink forms on the bottom edge of the tape spring while a global torsion develops along the structure. It is almost instantaneously followed by the formation of two kinks on the top edge of the tape spring. This configuration is extremely unstable and one kink reduces in amplitude as the test progresses, which causes the single bottom kink to slowly migrate off-center. When one of the top edge kinks fully disappears, the remaining top edge kink and the bottom edge kink move towards each other and merge to form a single fold. Note that since torsion is allowed in the test, the fold does not form in the center of the structure and it never becomes perpendicular to the axis of the tape spring. The relative amplitude between the two top edge kinks drives the behavior between the peak and the steady state. In the experiment, we observe that both kinks fully form and their amplitudes grow until a rotation of about 20 deg, which explains the rising path after their initial formation. However, in simulation, while the amplitude of one top edge kink increases after its initial formation, the other sees its amplitude decreasing rapidly. This sequence of amplitude increase and decrease explains the falling path observed in simulation. Note that the two different paths emerge from a single bifurcation point, and are extremely sensitive to local edge imperfections. For other tape spring samples, the opposite behavior has been observed in experiment, for which the path after the peak is falling all the way to the steady state moment. An accurate resolution of the tape spring local edge imperfections would allow the Riks solver to transition to the experimental path (rising path), but this has not been attempted here. The peak and steady-state moments are accurately predicted by the finite element analysis. The unloading behavior differs from what is observed in the case of clamped boundary conditions [72]. While previous experiments show no hysteresis for equal sense bending, the present experiment features a different response. Both loading and unloading responses are identical above a rotation of 20 deg. When the rotation is decreased further during unloading, the global twist reduces while the single fold slowly disappears, causing the bottom kink to travel to the middle of the edge while the top kink travels towards the end of the tape spring. If the global twist was constrained, the tape spring would instead form the two top edge kinks observed during loading.

To conclude this section, we saw that the bending machine allows to resolve the loading and unloading of the tape spring, and the finite element simulation gives a very accurate prediction of the key features of these tests. The isostatic nature of the testing machine eliminates any self stress in the structure during the test, therefore

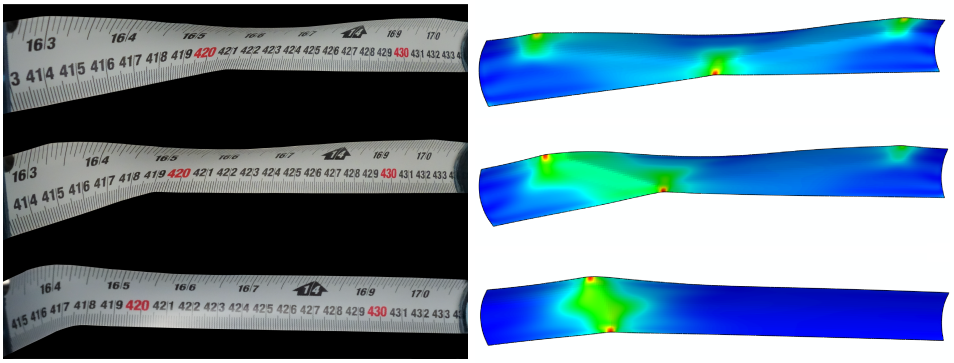

(a) (b)

Figure 3.14: Tape spring deformed shape obtained for the equal sense bending test. (a) Experimental deformed shape and (b) finite element deformed shape. The color map corresponds to the distribution of the Von Mises stress, but it is used here for sole visualization purposes.

eliminating any stress disturbances. Statically indeterminate boundary conditions often prevent the peak moment for both equal and opposite sense bending to be predicted accurately. An accurate match between experiment and simulation is achieved here, as the geometric imperfection is the only perturbation applied on the test structure. The interaction between boundary conditions and tape spring imperfections is explored further in the next section, and confirms this observation.

3.7 Interaction between kinematic constraints and imperfections

In this section, we use the example of a tape spring with initial geometric imperfections to illustrate the effect of statically indeterminate boundary conditions. If no adjustments are made, misalignment between the structure's end mounts can cause an initial prestress in the test structure, which in turn can dramatically affect its behavior.

To illustrate this sensitivity, the same nominal tape spring as in Section 3.6 is considered, and its equal sense bending response is simulated. It is important to recall that in the simulation of Section 3.6, the tape spring geometry includes imperfections based on measurements of the actual experimental sample. In this section, the nominal tape spring geometry is considered with different types of geometric imperfections that do do not corresponds to the ones used before. For this reason, we expect different responses from the simulation of Section 3.6 and the one presented here. The finite element model, described in Figure 3.11, is also used.

We focus on the effect of releasing constraints in the boundary conditions, and highlight the benefits of an isostatic testing machine. In particular, we are comparing the testing machine of Figure 3.1d and 3.1e with our testing machine illustrated in Figure 3.1f. Two types of global imperfections resulting in a missalignement of the test structure's mounts are analyzed here, using finite element simulations. Camber, shown in Figure 3.15a, and twist, shown in Figure 3.16a, are of particular interest since they are common global imperfections observed in thin-shell components. Note that in the case of a bending imperfection around the z-axis, the actuator's initial rotation can be offset to guarantee that the structure is stress free at the beginning of the test. In order to study the impact of global camber and twist, the structure is deformed and its deformed shape is then imported into the finite element simulation of Section 3.6. To create an initial camber, one end cross-section is clamped while a rotation around the X-axis is applied to the other end cross-section (kept rigid). To generate an initial twist, the process is similar, with a rotation applied around the Y-axis. Note that only the deformed geometry is imported, and the structure is stress free after the importation. In a first analysis step, an opposite rotation is applied to the structure such that its end cross-sections are realigned. It results in an initial stress of the structure. The boundary conditions specific for each machine are then applied to the structure which is allowed to relax in a second analysis step. In the final step, the structure is bent around the z-axis.

The buckling sensitivity to the tilt between the end-cross sections (caused by the global camber), is shown in Figure 3.15. The main observation is that the initial tilt affects dramatically the peak moment and transition into buckling for the statically indeterminate boundary conditions. For the testing machine of Figure 3.1d, once the structure has been prestressed during mounting, the boundary conditions do not allow it to relax, if no adjustment systems are considered. Even a tilt between the structure's mounts as small as 0.05 deg results in a decrease of 20 % in the peak moment. While one can argue that it is possible to mount the structure on adjustable brackets that compensate for the structure's imperfections, measuring and correcting the misalignment of the mounts with an accuracy error below 0.05 deg is extremely challenging in practice. Note that the prestress caused by the initial tilt also affects the deformed shape in the postbuckling regime. For the testing machine of Figure 3.1e, the initial stress state created by straightening the structure changes once it is mounted on the machine, since the release of the rotational constraints enables the partial relaxation of the structure. However, in this design, the rotations of the two sliders are coupled by the redundant constraint on the translation along the

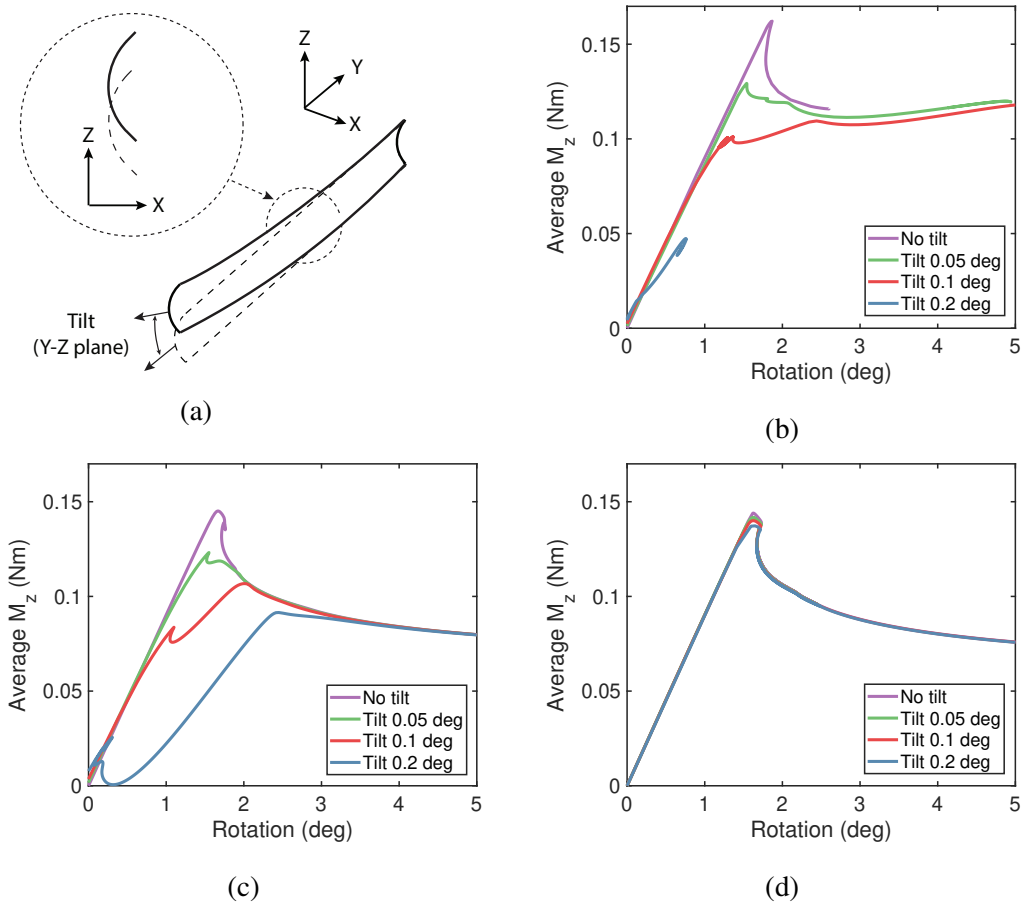

Figure 3.15: Analysis of an imperfect structure for which a global camber induces a tilt between the two end cross-sections as illustrated in (a). The imperfect structure behavior is simulated for the testing machine architecture of (b) Figure 3.1c for which the sample rotations are constrained, (c) Figure 3.1d for which the sample rotations are released, but the vertical translation is constrained, and (d) for the present, isostatic bending machine.

Z-axis, as explained in Section 3.2. When one slider rotates, the corresponding end cross-section translates along the z-axis. Compatibility of displacements imposes a similar translation of the second end-cross section which inherently causes the second slider to rotate. Therefore, there exists a coupling between bending and twisting, and its effect is shown in Figure 3.15c. Even if the degree of indeterminacy for this architecture is much lower than in the previous case, the buckling behavior is dramatically affected by the redundant constraint. A tilt of 0.05 deg induces a 15 % decrease in peak moment and its effect is more significant for larger values of tilt. Finally, the statically determinate architecture yields an imperfection-insensitive behavior highlighted in Figure 3.15d. The boundary conditions allow the structure

to be fully stress free before the bending experiment is carried out. The peak moment decreases by 5 % between the perfect structure and the worst tilt analyzed (0.2 deg). The response around the peak is identical for all tilt values and the spread in peak moments is only caused by the change in the structure's geometric properties and is not influenced by the testing machine. Note that the behavior of the perfect structure is similar in Figure 3.15c and 3.15d, but differs from Figure 3.15b in which the peak moment is higher.

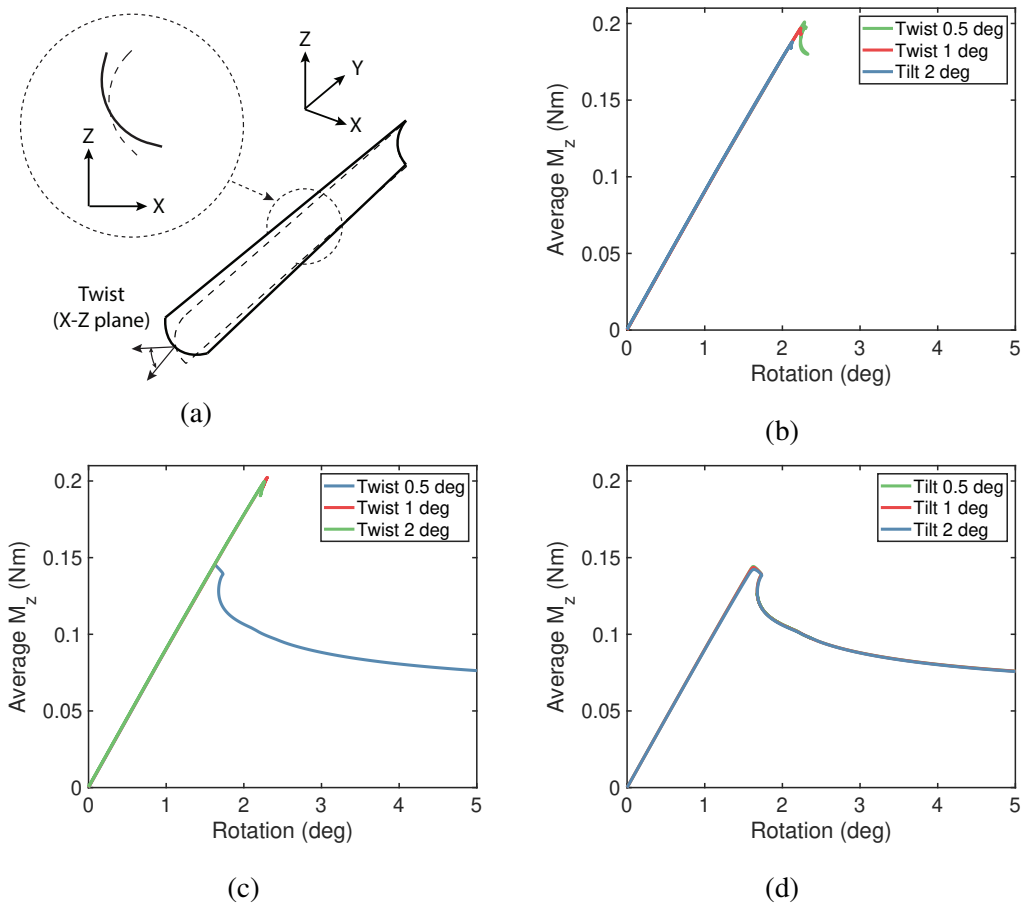

Figure 3.16: Analysis of an imperfect structure for which a global torsion induces a twist between the two end cross-sections as illustrated in (a). The imperfect structure behavior is simulated for the testing machine architecture of (b) Figure 3.1c for which the sample rotations are constrained, (c) Figure 3.1d for which the sample rotations are released, but the vertical translation is constrained, and (d) for the present, isostatic bending machine.

We then shift our focus to the global twist imperfection, represented in Figure 3.16a. When the rotations are constrained, as in Figure 3.16b, the peak moment increases significantly for all values of twist when compared to the perfect structure

of Figure 3.15b. As mentioned in Section 3.6, the first buckle forms simultaneously as the structure starts twisting. An initial twist affects significantly this behavior, and a twist in the other direction will have the opposite effect (reduction of the peak moment). However the variation in peak moment is less important than for the camber imperfection. Since the torsional stiffness of the structure is much lower than its in-plane bending stiffness, the prestress caused by the twist has a lower magnitude than for the camber imperfection, which explains the more limited spread in buckling moments. When redundancy is limited to the sample's vertical translation, the buckling behavior follows to distinct regimes, shown in Figure 3.16c. For small twists, the state of self stress induced by the redundant constraint has a low magnitude, and the testing apparatus behaves like the isostatic machine. However for larger values of twist, the buckling behavior is similar to the one encountered in Figure 3.16b. Finally, the isostatic machine exhibits almost no variation of buckling moment when the twist is varied. Moreover, the bending characteristic observed for the twist imperfection matches the one observed from the camber imperfection. From the isostatic experiment, we can therefore conclude than the geometric twist imperfection does not have a significant influence on the equal sense bending of the tape spring. This conclusion would not have been possible to reach with the two other experimental setups, as the effects of the parasitic stress perturbation mask the low geometric imperfection sensitivity.

3.8 Conclusion

Throughout the chapter, we highlighted the importance of boundary conditions in pure bending tests. Various pure bending machines have been designed and are mostly used for material testing or stiff structures, for which they demonstrated advanced performances. Of particular interest is the use of frictionless linear guides which enable us to mitigate the effect of parasitic reactions moments and forces on the test structure. However, these architectures all have redundant boundary conditions which cause them to be statically indeterminate. While it is often not an issue for flat and stiff samples, it has a dramatic impact in the testing of very thin-shell structures, for which the unstable behavior at buckling is extremely imperfection sensitive. Geometric imperfections are often introduced during manufacturing of thin-shell structures, and will inherently affect the behavior of these structures, regardless of the testing machine. However, in the case of a statically indeterminate testing apparatus, the geometric imperfection can also introduce a stress perturbation in the form of an initial stress state. In practice, the effect of this stress perturbation is much

more important than the geometric imperfection itself, and artificially increases the apparent imperfection sensitivity of the structure.

This chapter tackled the development of a new bending machine for which the boundary conditions are statically determinate. It is inspired by the testing machine presented in [11] and releases its only redundant constraint, the test structure's out-of-plane translation, using an offloaded sliding bracket. The accuracy of this machine was first analyzed through the testing of circular rods. These tests highlighted a very good agreement between simulations and experiments (less than 1 % relative error), and the magnitude of parasitic effects induced by the cables and slider rotations is negligible for the type of structures the machine is designed for. Testing has then been extended to tape springs, which captures essential features of non-linear structures undergoing complex instabilities. Here again, the analysis showed that it is possible to resolve accurately their complex bending behavior. We finally presented simulations on the same tape springs which highlighted the effect of initial stresses caused by geometric imperfections in statically indeterminate testing machines. It has been shown that these effects dominate the structure's buckling behavior and are often masking the structures' real geometric imperfection sensitivity. In the isostatic bending machine presented in this chapter, the imperfection sensitivity of the test structure can be directly quantified since no other perturbations can affect the test results.

This new testing machine paves the way for the experimental study of the buckling sensitivity of thin shell structures. Of particular interest is the study of localization of buckling modes and the sensitivity to disturbances in the structure's environment [70]. The magnitude of the disturbances analyzed in such studies is extremely small (disturbance energy below 1 mJ), and any parasitic effect or prestress introduced by the testing machine would make these effects undetectable.

Chapter 4

THIN-SHELL STRUCTURES UNDER BENDING: EXPERIMENTAL STUDY

4.1 Introduction

Thin shells have been widely used in many engineering applications. They enable very lightweight structures to be built, while featuring excellent load-carrying capabilities. They play a paramount role in the development of aerospace vehicles for which mass is often the most critical design parameter. As new applications appear, and more advanced capabilities are sought, the thickness of thin shells tends to go down. In the past decades, the rapid progress of high-strain composites used in deployable structures accelerated this trend [50], with thin shell booms being used to support large aperture space systems [7, 16].

However, one of the main challenges in using thin shell structures is the unpredictability of their buckling behavior. This complication lies in the physics of the buckling event. For thin shells, buckling is part of a wider family of instabilities called sub-critical bifurcations, which exhibit an immediate falling post-buckling response in the load/displacement plane. If the path does not regain stability, the structure loses all its load-bearing capabilities and fails. In most cases, the unstable post-buckling path runs very close to the pre-buckling path (also called fundamental path), making the structure meta-stable close to the bifurcation point. It is then possible to transition early into the post-buckling regime if a small amount of energy is brought to the system, and if the difference in total potential energy between the two states is overcome. The "proximity" between the pre-buckling and post-buckling states also makes the structure extremely sensitive to imperfections, which was first discovered in early experiments on cylindrical shells [13, 44, 82]. For a real structure, a small imperfection would easily erode the energy barrier between these two states, otherwise found in the theoretically perfect structure. The imperfection thus behaves like a connecting mechanism between these two states, causing the bifurcation point to be encountered earlier than theoretically predicted. The phenomenon is even more pronounced as the thickness of the shell decreases.

In order to still be able to use these structures in practice, structural engineers usually avoid buckling at all cost. For axially compressed cylindrical shells and

pressurized spherical shells, numerous experiments have been conducted in the twentieth century, and a lower bound on the statistical distribution of experimental buckling loads determined. The difference between the theoretical buckling load and this empirical lower bound, called knockdown factor, has been the basis of practical cylindrical and spherical shell designs. It led for instance to the NASA space vehicle design criteria for the buckling of thin-walled circular cylinders (NASA SP-8007) [62]. Although the classical knockdown factor approach is powerful, it has two major limitations. First, it is widely seen as very conservative and therefore often prevents using the mass saving capabilities of thin shells to their full extent. Recent efforts by NASA's Shell Buckling Knockdown Factor (SBKF) Project established in 2007, aims to develop revised and more realistic knockdown factors[29]. Second, each knockdown factor is only valid for a unique structure/loading combination and is therefore difficult to generalize to other kind of structures and applications. It has been shown that knowing accurately the structure's initial geometry enables the accurate prediction of the buckling event [51]. However, in many applications, measuring the shape of the structure before use can be both expensive and in some cases impossible.

On top of imperfection sensitivity, localization of buckling deformations makes the thin-shell buckling behavior even harder to predict. It causes significant differences between the theoretical buckling eigenmodes and the experimentally observed deformed shape. Localization arise in two situations. The first corresponds to post-buckling localization and is a manifestation of the extremely non-linear response of the structure after the bifurcation is exceeded. In this case, the onset of the buckling eigenmode appears at the exact point of bifurcation, and greatly affects the structure's geometric stiffness. As the loading is increased, deformations concentrate at specific locations, given by the peak eigenmode amplitude and/or by dominant imperfections. In this case, the buckling mode starts with global deformations and becomes more and more localized. This type of localization is for instance observed for beams on elastic foundations [83] or for spherical shells under pressure [4, 38, 40]. Another localization scenario is observed when a global post-buckling mode is created through the sequential formation of localized buckles. It features a series of destabilization and restabilization of the post-buckling path known as snaking, or cellular buckling [35]. Interestingly, the first localized buckle can appear on post-buckling paths disconnected from the fundamental path, while running asymptotically close to it [23]. This phenomenon is observed in cylindrical shells for which a single dimple, "broken away" from the unbuckled state, evolves to a fully

periodic buckling mode through snaking [23, 45]. It has been proven that for the cylindrical shell, the single-dimple state sits on a mountain pass in the energy landscape, between the pre-buckling and post-buckling states, and is the lowest critical escape mechanism by which the structure can buckle [32]. Since the location at which deformations localize heavily depend on the imperfections of the structure, it can generate a large number of post-buckling solutions even for a small set of theoretical eigenmodes. This is referred to as spatial chaos [80].

The imperfection sensitivity driving the buckling behavior is then twofold. It erodes the energy barrier between pre-buckling and post-buckling states, causing early buckling, and it creates a high number of possible post-buckling paths through localization. For these reasons, predicting buckling is extremely difficult for shell structures and often relies on a case by case approach. Recent work has focused on the sensitivity of the buckling phenomenon to disturbances in thin cylindrical and spherical shells. A non-destructive experimental method has been proposed in 2013 to study the meta-stability of the unbuckled state. It focuses on determining the energy barrier separating the fundamental path and the critical localized post-buckling state [41, 75, 79]. The search for the load at which the critical buckling mechanism can be triggered is carried out by imposing a local radial displacement in the middle of the structure using a probe. This method effectively quantifies the resistance of shell buckling against the single dimple imperfection mentioned earlier. The method has been successfully applied to cylindrical shells [81] and to pressurized hemispherical shells [53]. These experiments quantified in particular the onset of meta-stability, often referred to as "shock sensitivity" [76], and a comparison with historical test data has shown that this specific loading can serve as an accurate lower bound for experimental buckling loads [20, 23], leading to better knockdown factors.

In this chapter, we wish to apply and extend the experimental probing methodology used for cylindrical and spherical shells to more complex structures. These thin shells capture the essence of ultralight coilable space structures recently developed in the Space-based Solar Power Project (SSPP) at Caltech [3, 71]. Previous analysis showed that local buckling plays a key role in such structures [69] and motivates the need to conduct experimental buckling characterization. However, the size of the structure together with the complexity of its components and the peculiarity of its non-uniform bending moment, makes experiments very challenging. In order to address these limitations, the behavior of a simpler structure under pure bending is

presented here. While the structure and loading are different, it enables us to draw more general conclusions on the buckling of structures featuring thin-shell open cross-sections. The approach here is purely experimental and complements finite element probing analyses presented in previous work.

An important characteristic of the structure studied in this chapter is that its post-buckling path restabilizes under bending and therefore, the maximum moment it can carry is greater than the first buckling moment [69]. Such behavior offers an incredible opportunity to operate closer to buckling than ever before. If applications allow, the structure can also be used in its post-buckling regime, as long as we have guarantees that it will behave safely. To achieve these goals, the present chapter aims to show that by using the experimental probing methodology, the meta-stable behavior of the structure close to buckling can be fully characterized. This knowledge can be used to derive very efficient buckling criteria based on disturbance levels, or the minimum load at which meta-stability arises. The methodology can then be extended to navigate spatial chaos in the post-buckling regime, where competing paths can be identified and a range of possible post-buckling responses determined. The philosophy here is to embrace buckling rather than avoid it, and therefore enable the use of dramatically lighter structures.

The chapter is structured as follows. Section 4.2 describes in more detail the test structure and the experimental bending a probing setup. Following a classical buckling analysis, Section 4.3 highlights the importance of localization and spatial chaos by comparing finite element simulations and the experimental buckling response. In Section 4.4, probing experiments are carried out to study the formation of the experimentally observed buckling mode and characterize its meta-stable behavior. In Section 4.5, probing is applied along the entire structure to determine alternate locations at which local buckling can appear, and the formation of these alternate modes is studied through additional probing. Consequences of their appearance on the global bending response are finally highlighted, and Section 4.5 concludes the chapter.

4.2 Test structure and experimental setup

Test structure

The test structure is made of tape springs called longerons, connected transversely by rods called battens. The complete structure is referred to as a strip. The longerons are cut from a Crafstman 1-in blade tape measure, and their length is $L = 714$

mm. Their cross-section can be approximated by a circular arc to which tangent flat segments are added to the two extremities. Details of the cross-section are presented in Figure 4.1d. The circular portion of the cross section has a radius of 14 mm, an opening angle of 75 deg, and the flat sections are 3 mm long. The shell thickness is $t = 110\ \mu$m. The longerons are made of stainless steel with a measured Young's modulus of $E = 208$ GPa and Poisson's ratio $\nu = 0.3$. The battens are pultruded carbon fiber rods of diameter $d = 2$ mm and Young's modulus $E = 140$ GPa. The battens have a length of $l = 50$ mm.

Four battens are inserted and glued into rivets pinching the longerons. In addition, both sides of the rivets (longeron back/front) are embedded into a hemisphere of epoxy, which guarantees a full connection between longeron and batten. The end cross-sections of each longeron are inserted and glued into an acrylic plate in which the cross-section has been laser cut. The acrylic plates serve as the interface between the test structure and the bending machine described next.

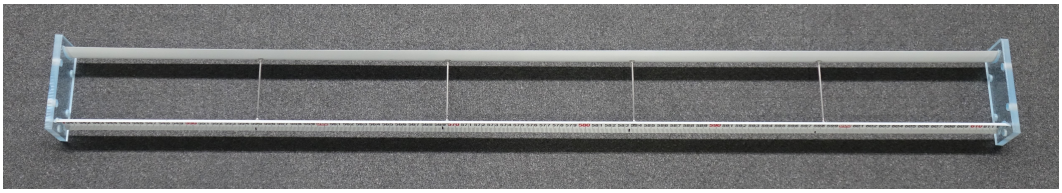

(a)

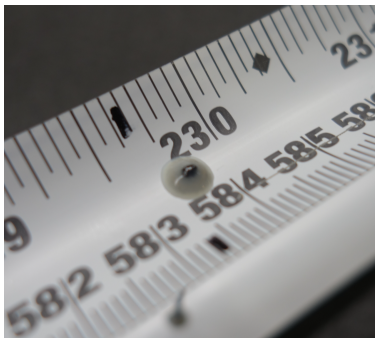

(b)

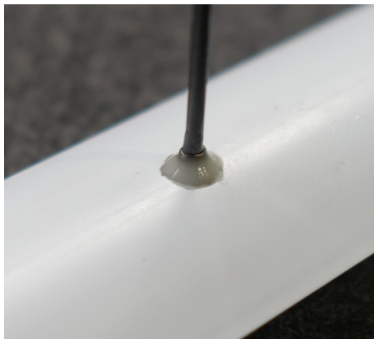

(c)

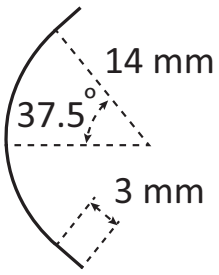

(d)

Figure 4.1: (a) Thin shell test structure used in the experiment. The longerons are made of stainless steel tape springs and connected transversely by carbon fiber rods. Full (b) front connection and (c) back connection between batten, rivet, and longeron. (d) Approximated tape spring cross-section used for the longerons.

Bending machine

The original pure bending machine used in the experiment is discussed extensively in previous work, and a CAD model is shown in Figure 4.2. The actual implementation

is shown in Figure 4.4. It employs two linear guides on which air bearings are able to translate and rotate along and around the guides' axes. This architecture guarantees that no parasitic reaction forces can arise during the test, and that only a bending moment can be applied to the structure. There is no redundancy in boundary conditions provided to the test structure, which makes the system statically determinate and prevents any self-stress during testing. The boundary conditions provided to the test structure are detailed in Figure 4.3. Several components are attached to each air bearing, and we refer to this assembly as a slider. The actuated slider, on which one end of the test structure is attached, is made of a DC motor (Harmonic Drive FHA-8C) which controls the rotation of the sample around the local z-axis. The rotation profile follows a smooth s-curve, and the maximum angular acceleration can be chosen to be 0.05 deg/s to limit dynamic effects. An incremental encoder with a resolution of up to $800,000$ counts per revolution measures the applied rotation. A force/torque sensor (ATI Mini40) is attached to the motor's rotating end and can measure bending moments up to 2 Nm. An aluminum bracket is mounted on the sensor and provides and interface to attach the test structure. The second end of the test structure is attached to the rigid slider, where the DC motor is replaced by an aluminum column. An offloaded bracket allows the sample to translate along the slider's local z-axis. It uses a hanging mass and a pulley, which compensates for half of the mass of the test structure and half of the mass of the bracket's translating assembly. To avoid parasitic moments caused by gravity, a counterweight is attached to the top of each slider and can be adapted to a wide range of sample masses. Finally, a probing stage is added to the bending machine and perturbs the test structure locally. This specific apparatus is described next.

Probing stage

In addition to being subjected to the main bending moment, the strip is perturbed by a "probe" that locally displaces the longeron. The probing apparatus is composed of a motorized linear stage (Newport MFA-CC) providing a positioning accuracy of ± 3 μm. A force sensor (ATI Nano17) is mounted on the moving part of the stage and supports a wedge that comes into contact with the longeron edge when probing is applied, as seen in Figure 4.4c. The sensor measures the probe force with a resolution of 1/320 N, and an incremental encoder on the motorized stage measures the probe displacement with a resolution of 0.0176994 μm. When the structure is bent, half of the longeron will undergo compression, with the maximum stress being found on the edge. The wedge axis is perpendicular to the longeron edge, creating a

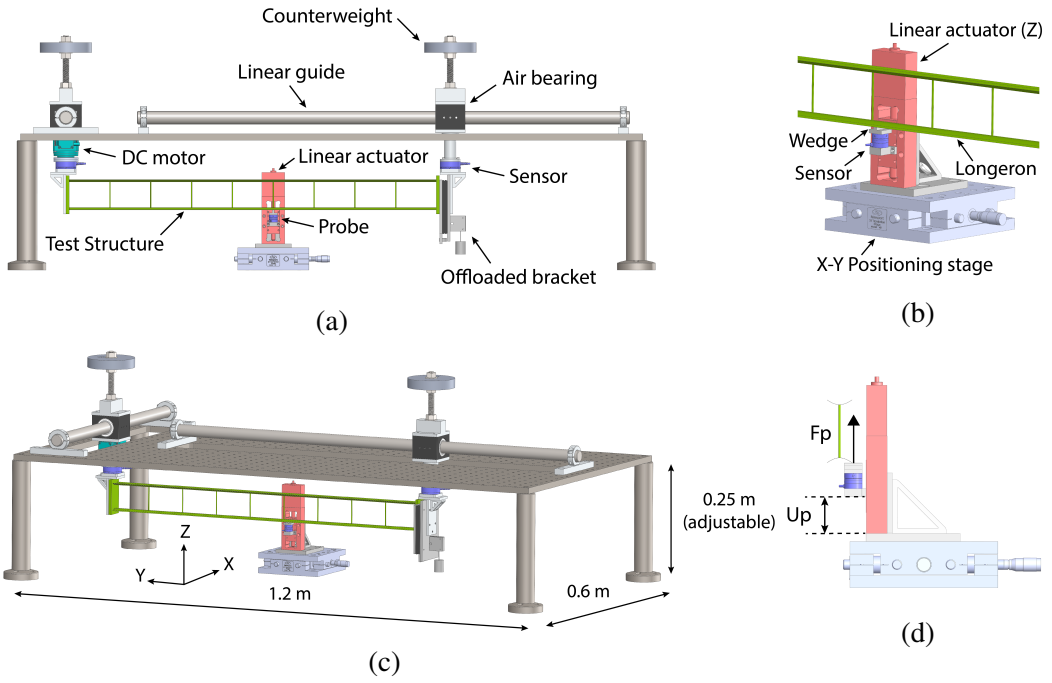

Figure 4.2: (a) Front view of the pure bending machine and its probing stage. The machine provides isostatic support conditions to the test structure and its dimensions are illustrated in (c). Details of the probing stage are presented in (b) and (d).

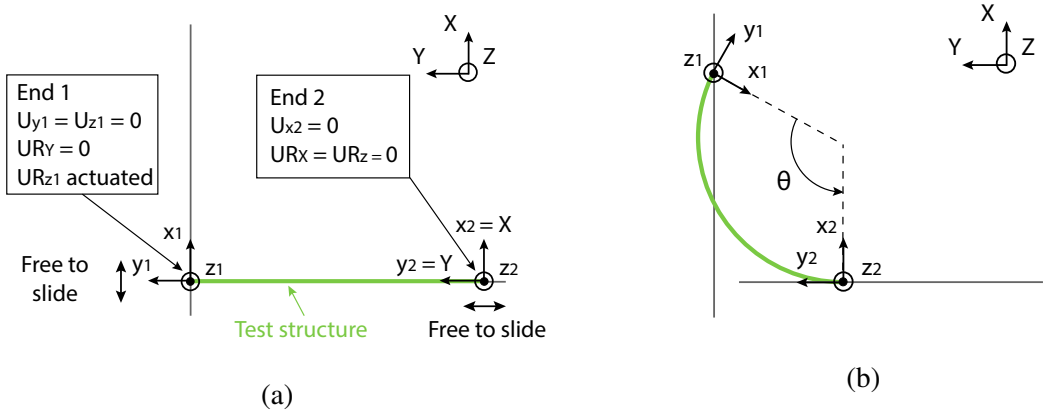

Figure 4.3: Conceptual representation of the bending machine, specifying the boundary conditions on the two ends of the sample. U corresponds to the translational degree of freedom and UR to the rotational degree of freedom. (a) Undeformed configuration and (b) deformed configuration after a rotation of θ is applied to end 1.

punctual contact between the two parts. As the longeron is probed, its cross-section flattens, and there exists a relative motion between the wedge and the longeron. The impact of friction on the probing characteristic is reduced by fabricating the wedge

out of Teflon. Details of the probing stage are shown in Figure 4.2b, d, and Figure 4.4d, c.

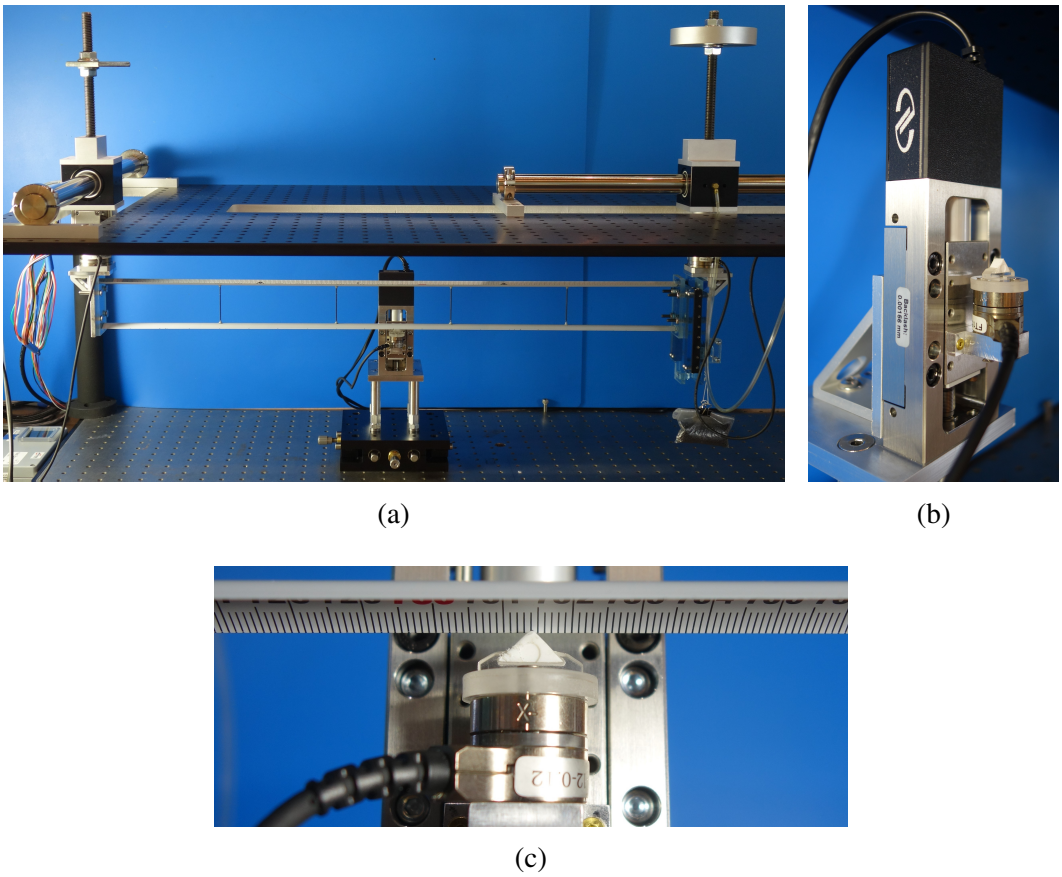

(a) (b)

(c)

Figure 4.4: Physical implementation of the experimental apparatus. (a) Setup overview with the test structure mounted in the bending machine and the probing stage placed under it. (b) Detailed view of the probing stage and (c) the Teflon wedge that comes into contact with the longeron edge.

4.3 Classical buckling experiment and analysis

Buckling eigenmodes

The first step in understanding how buckling unfolds is to conduct a buckling eigenvalue analysis. The goal is to detect bifurcations arising on the structure's pre-buckling path or fundamental path. It gives insights into the buckling loads/rotations but also unveils additional buckling modes that can be found above the first bifurcation. knowing the buckling modes is important since they reveal critical imperfections that have a practical influence on the transition into the post-regime regime. They also give information about the deformed shapes to be expected once the structure buckles.

To compute the buckling eigenvalues/eigenmodes, a finite element model is created in Abaqus 2018, which replicates the structure's geometry, materials, and the bending machine's boundary conditions. To compute the "exact" buckling eigenmodes and moments, an iterative procedure is required as the fundamental path can exhibit geometric nonlinearities for thin shell structures [48]. The first iteration follows a classical buckling analysis. A linear perturbation is applied to the stress-free structure and buckling moment estimates are computed. The strip is then loaded by a bending moment, under the first buckling moment estimate, and the problem is linearized about this new pre-stressed state, taking into account pre-buckling nonlinearities. This process is repeated until the first buckling moment estimate converges to its "real" value. The analysis yields four bifurcation points, and their corresponding buckling eigenmodes are shown in Figure 4.5.

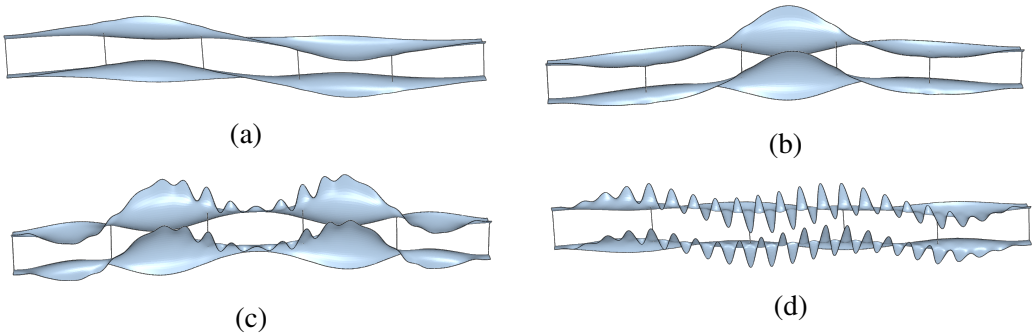

Figure 4.5: Buckling eigenmodes determined through finite element simulations. The eigenvalue problem is linearized around a state where the structure is prestressed by a bending moment of 1 Nm. (a) First (M_{cr} = 1.604 Nm), (b) second (M_{cr} = 1.759 Nm), (c) third (M_{cr} = 2.003 Nm), and (d) fourth (M_{cr} = 2.009 Nm) eigenmode.

The first two buckling modes are dominated by long wavelength deformations spanning the entire longerons, and therefore can be characterized as global. The last two buckling modes feature short wavelength deformations modulated in amplitude by a global long wavelength deformation. Note that in Figure 4.5, the amplitude of these deformations is arbitrary since it represents normalized eigenmodes. From this analysis, a first buckling moment around M_{cr} = 1.6 Nm is expected, as well as a post-buckling deformed shape resembling the first eigenmode, as seen in Figure 4.5a. However, the classical buckling eigenvalue analysis has two main limitations. First, it does not take into account the imperfections found in the real structure. These imperfections can change the order of bifurcations, and prioritize one buckling eigenmode over another. The post-buckling deformed shape often stems from a linear combination of the first few buckling modes, if their buckling moments are

relatively close. Second, thin shells exhibit buckling mode localization, as explained in Section 4.1. In most cases, even for a perfect structure, the computed eigenmode is only valid at the bifurcation point, and deformations localize at one or more preferred locations as soon as the structure transitions to its post-buckling regime.

Moment/rotation response and post-buckling localization

A set of five bending experiments are carried out. The maximum rotation is set to $\theta_{max} = 3$ deg. The mean moment/rotation response, as well as the experimental standard deviation, is shown in Figure 4.6a. In Figure 4.6a and throughout the chapter, the average of the two end bending moments is reported. The response is linear until the structure bifurcates for $\theta_{cr} = 1.74$ deg and $M_{cr} = 1.25$ Nm. The structure undergoes a snap-back and restabilizes at $M_{cr} = 1.09$ Nm. Note that the experimental buckling moment is 22% lower than the first theoretical bifurcation, which highlights the imperfection sensitivity of the structure. In the experiment, the snap-back occurs over a small range of rotations, and a quasi-static response (vertical tangent) would be observed for a lower angular velocity. The post-buckling regime is stable for both moment and rotation-controlled cases, and the response is weakly non-linear. In further tests, presented at the end of the chapter, the maximum rotation has been extended to $\theta_{max} = 10$ deg and shows that the stable post-buckling regime extends to larger values of bending moments. It suggests that the strip could be safely operated in its post-buckling regime, and this type of behavior has been observed previously for a similar type of structures [69].

We wish to compare the experimental response with finite element simulations. In particular, we want to compute the post-buckling paths corresponding to the first two eigenmodes. To do so, a standard method is employed [66, 68]. Each mode is seeded in the structure's initial geometry as a geometric imperfection. Here the imperfection amplitude is chosen to be 30% of the shell thickness (t). The modified Riks solver available in Abaqus is used to trace the stable and unstable part of the post-buckling response. These paths are shown in Figure 4.6b together with the experimental response. The corresponding deformed shapes at the end of the two post-buckling paths are shown in Figure 4.6d (first mode) and 4.6c (second mode). In both cases, the post-buckling shapes exhibit significant differences with the buckling eigenmodes. They feature highly localized deformations extending inward (towards the structure's longitudinal mid-plane), forming a series of alternating buckles. The buckle locations coincide with the inward peak deformations found in the eigenmode. It illustrates that here, the localization phenomenon prioritizes inward

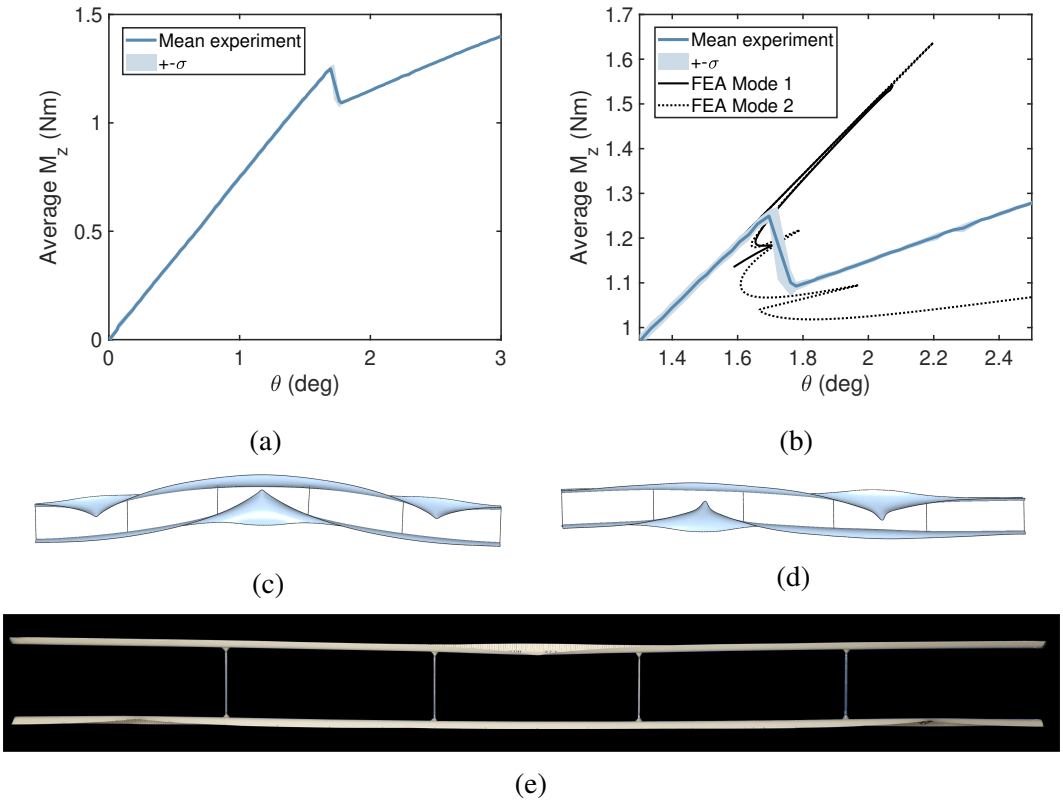

Figure 4.6: (a) Mean experimental moment/rotation curve and standard deviation for five bending experiments. (b) Comparison between experiment and FEA in the vicinity of the bifurcation point. (c) Post-buckling mode obtained by FEA when seeding the second buckling eigenmode as imperfection. (d) Post-buckling mode obtained by FEA when seeding the first buckling eigenmode as imperfection. (e) Experimental post-buckling shape.

deformations, as no outward buckles are found. The post-buckling paths feature a snaking sequence, characterized by a series of destabilization and restabilization events. Snaking corresponds physically to the sequential formation of buckles. For the post-buckling path corresponding to the second mode, the structure bifurcates at higher values of moments than for the first mode, as expected from the eigenvalue analysis. The central buckle formation corresponds to the first post-buckling fold, directly connected to the unbuckled path, while the side buckles form in the second and third folds. The post-buckling shape corresponding to the first mode forms in a similar way. The structure bifurcates around $M = 1.58$ Nm and the first fold corresponds to the formation of one of the two buckles. When the second destabilization point (called snaking point) is reached, the second buckle starts to form. However, the simulation is stopped before the path restabilizes. At this point, the two buckles compete, causing the solver to oscillate between forming one or the

other. Continuing the simulation was not attempted here but is possible by tweaking the initial imperfection.

Next, the simulation results and the experiment are compared. The deformed shape obtained experimentally, after a rotation of $\theta = 3$ deg is applied, is shown in Figure 4.6e. It matches exactly the post-buckling shape found in simulation for the second eigenmode imperfection, even if in theory, the lowest bifurcation corresponds to the first eigenmode. Note that top and bottom longerons are interchangeable in Figure 4.6c/d since no gravity is applied in simulation. In addition, significant differences exist between the two post-buckling paths. The experimental post-buckling restabilizes at a higher moment, and the post-buckling stiffness is also higher. It highlights the limitations of a purely simulation-based design and analysis approach for such structures. In particular, the transition to buckling happens at a significantly lower moment, due to the structure's imperfection sensitivity. Only two types of geometric imperfections are considered here, but any linear combinations of the four eigenmodes would potentially yield a different post-buckling solution corresponding to a different localization mechanism, characteristic of spatial chaos [24]. Note that it is possible to find all the potential post-buckling paths for the perfect structure using an advanced computational method, such as path-following [25]. However these methods are not usually available in commercial finite element software, and can only be matched with experiments if the real imperfections in the structure are known. Indeed, in reality, various post-buckling modes compete and the structure's imperfections determine which path connects to the unbuckled state. This path does not necessarily coincide with the solution given by the lowest eigenmode, and many paths can run close to the unbuckled path without ever intersecting it. These alternate modes can be accessed if a small perturbation is applied to the structure, causing early buckling. This meta-stable behavior is explored next, using probing experiments.

4.4 Probing the experimentally observed post-buckling mode

This section focuses on the formation of the post-buckling mode observed experimentally, if no perturbations are applied to the structure. In the rest of the chapter, this specific mode is referred to as main post-buckling mode. When a rotation of $\theta_{cr} = 1.74$ deg is imposed, the bifurcation point is reached and the structure experiences a snap-back, during which three buckles form simultaneously. They are shown in Figure 4.6e, and are referred to as the TC (Top edge Central), the BR (Bottom edge Right), and the BL (Bottom edge Left) buckles. In reality, their formation

follows a specific snaking sequence, resembling the simulated post-buckling paths of Figure 4.6b. However, in a rotation-controlled experiment, unstable portions of the response are not captured, and the snaking sequence is hidden by the snap-back event. Once the first local buckle forms, it triggers the formation of the second buckle and subsequently the third one. These buckles interact with each other through global structural deformations (torsion, in-plane and out-of-plane bending). However, close to the buckling load, the structure is meta-stable and equilibrium configurations featuring one or more of these local buckles can be attained if a small perturbation is applied to the structure. Of particular interest is the lowest rotation/bending moment at which these buckles can be found in equilibrium, and the energy barrier that needs to be overcome to form them. In this section, each of the three buckle locations (TC, BR and BL) are probed. For a fixed rotation, the longeron's edge in compression is locally displaced at each of the three buckle locations, and the probe reaction force is measured. The rotation increment is set to 0.05 deg initially and refined to 0.02 deg at higher values of rotation (when ridge and valley start). Three stability landscapes, which display the probe force as a function of the rotation and the probe displacement, are shown in Figure 4.7. They give insights into which combinations of buckles can be observed before the bifurcation point and identify the critical buckle responsible for the transition into the post-buckling regime. This representation was first introduced in 2016 [81] for cylindrical shells. We show here that similar stability landscapes can be found for more complex structures.

Top edge central probing (TC)

The top edge central buckle location (TC) is first probed and the results of the experiment are shown in Figure 4.7a. For $\theta < 1.29$ deg, the probe force F_p increases monotonically as the probe displacement U_p increases, and the probe force is close to linear with respect to the probe displacement when the applied rotation is small ($\theta < 0.5$ deg). When the rotation is increased, the probe force versus probe displacement characteristic is no longer monotonic, and a region of negative probe stiffness appears. It creates two important features in the stability landscape. The local maximum of probe force forms the ridge (dashed and dotted line) and the local minimum, the valley (dashed line). In a force-controlled probing experiment, the structure would undergo a snap-through instability and kinetic energy would be released. For probe displacements larger than the critical valley displacement, the probe force increases monotonically again. As the rotation is increased, the probe

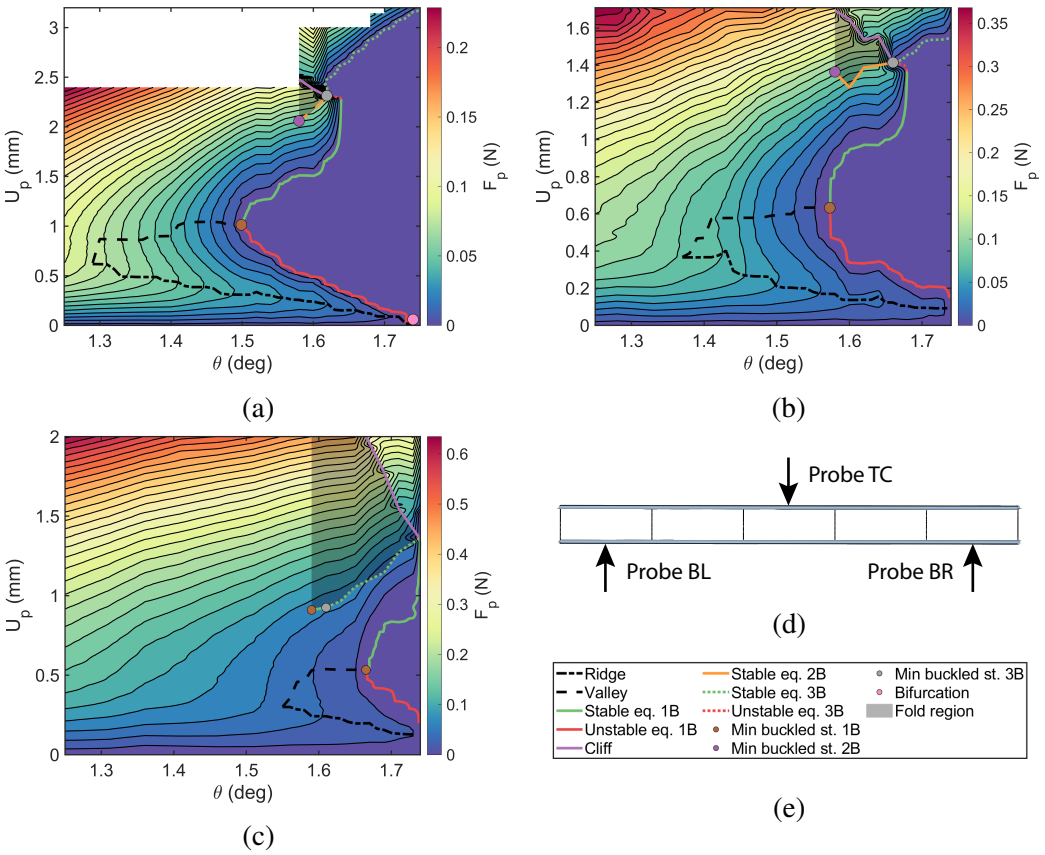

Figure 4.7: Stability landscapes for the (a) TC probe location, (b) BR probe location, (c) BL probe location, and (d) their common legend. (e) Schematic of the strip structure with the three probe locations.

force at the valley decreases until it reaches 0 N for $\theta = 1.5$ deg. It corresponds to the smallest value of rotation at which a local single buckle (labeled 1B) can be formed and remains in equilibrium at the probe location. This value is referred to as the single-buckle minimal buckling rotation and corresponds to the minimally buckled state found at the end of the valley. The ridge displacement decreases as the rotation increases until the ridge disappears at the point of spontaneous buckling (or bifurcation point), for $\theta_{cr} = 1.74$ deg. The stable (solid green) and unstable (solid red) single-buckle equilibrium contours, for which $F_p = 0$ N, stem from the single-buckle minimally buckled state. Above the minimal buckling rotation, the structure undergoes a snap-through instability when the probe displacement reaches the unstable equilibrium contour. At this point, the probe looses contact with the longeron and $F_p = 0$ N. Contact is restored when the probe displacement reaches the stable equilibrium contour. The region in which there is no contact between the probe and the longeron is referred to as the lake. If the probe was able to apply

tension in addition to compression, the landscape would feature negative probe forces in the lake.

Three types of equilibria appear during probing. These solutions are accessible if a disturbance provides enough energy to the structure. The energy barrier separating the unbuckled and buckled state can be computed by integrating the probe force as a function of the probe displacement, between the unbuckled state and the unstable equilibrium contour. An analysis of the energy barrier is presented in Section 4.4.4. For $U_p < 2.3$ mm and $\theta < 1.64$ deg, the single buckle equilibria are found (labeled 1B). However, for $1.58 < \theta < 1.62$ deg, the probed structure undergoes instabilities (fold region in Figure 4.7a) past the stable single dimple equilibrium contour. A probe characteristic featuring this instability is shown for $\theta = 1.6$ deg, in Figure 4.8a. This type of instability is called a cusp catastrophe [36]. When the probe reaches the cliff (in purple), the structure undergoes a snap-back and the probe force drops. The cliff corresponds to limit points at which the tangent to the probe characteristic is vertical. At this point, the probing path becomes unstable, folds, and eventually restabilizes at lower values of probe force. In the displacement-controlled probing experiment, the unstable portion of the path cannot be captured and the structure directly snaps to the lower (and stable) part of the fold. When retracted, the probe follows the entire stable path until the probe force reaches 0 N. The stable two buckles' (2B) equilibrium contour (shown in orange) is then found. On this contour, buckles appear at the TC and BR locations. If the probe displacement decreases further, the probe loses contact with the longeron and the two buckles remain in equilibrium. The shaded region represents the top view of the fold (or cusp). The smallest rotation at which the two buckles equilibria are found is $\theta = 1.58$ deg and is referred to as the two buckles minimal buckling rotation.

Finally, for $\theta > 1.62$ deg, equilibria featuring the full buckling pattern (3 buckles) are found. For a fixed rotation within the range $1.62 < \theta < 1.64$ deg, the TC buckle is created first. However, as the probe displacement is increased past the unstable three buckles (3B) equilibrium contour (dotted red), the structure experiences a snap-through and the probe looses contact with the longeron until it reached the stable three buckles equilibrium contour (dotted green). For $\theta > 1.64$ deg, any probing past the single-buckle equilibrium contour results in a direct snap-through to the three buckles equilibrium contour. If the stable single buckle is formed, and the rotation is increased without any probing, the structure will follow the single-buckle equilibrium contour until $\theta = 1.64$ deg, for which the three buckles pattern forms.

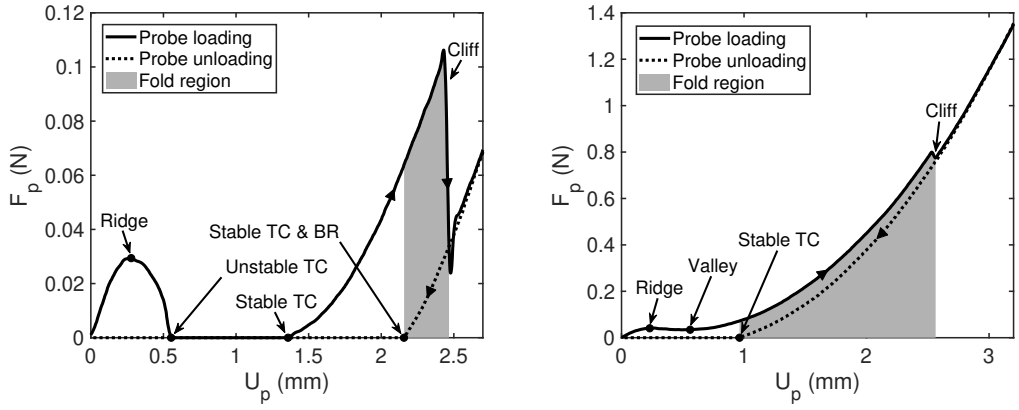

Figure 4.8: Loading and unloading probe force/displacement characteristic, for $\theta = 1.6$ deg, at the (a) TC probe location and the (b) BL probe location.

This rotation is referred to as the snaking rotation. This observation reveals that the snaking sequence is only composed of two folds corresponding to the buckling of the top longeron, followed by the buckling of the bottom longeron, even if the buckling pattern features three buckles.

Bottom edge right probing (BR)

The structure is unloaded and the probing experiment is repeated for the bottom edge right buckle location (BR). The results are shown in Figure 4.7b. The BR stability landscape exhibits the same features as the TC stability landscape. At $\theta = 1.37$ deg, the ridge and valley start. The valley vanishes at the single-buckle minimal buckling load for $\theta = 1.56$ deg, where the unstable and stable single-buckle equilibrium contours start. On these contours, a buckle at location BR is found in the structure. At the point of spontaneous buckling, for $\theta_{cr} = 1.74$ deg, the BR and TC probing behaviors differ. For the BR location, the ridge does not intercept the unbuckled state ($U_p = 0$ mm) and ends abruptly. The unstable single buckle contour is therefore offset from the unbuckled state. Such a buckling mode is often referred to as a broken away mode [23]. This important observation suggests that while the TC buckle can be formed at the bifurcation point, the BR buckle can only appear later in the snaking sequence, as far as the unperturbed structure is concerned. When perturbations are applied, the BR buckle can be triggered earlier, if the energy barrier separating the unbuckled state and the unstable single-buckle state is overcome. For $1.58 < \theta < 1.66$ deg, a two pattern can be formed in the unstable probing region (fold region). Similarly to the TC probing, once the probe

displacement exceeds the cliff, the probe characteristic follows a different path when retracted, and the two buckles equilibrium contour is found. It features the TC buckle in equilibrium with the BR buckle. Finally the three buckles pattern can be formed through large amplitude probing, for $1.66 < \theta < 1.68$ deg. Above the snacking rotation, for $\theta = 1.68$ deg, the structure experiences a snap-through to the stable three buckles contour as soon as the probe displacement exceeds the unstable single buckle contour.

Bottom edge left probing (BL)

Lastly, the probing experiment is repeated for the bottom edge left buckle location (BL), and the results are shown in Figure 4.7c. At this probing location, the ridge and valley appear at $\theta = 1.55$ deg, later than for the BR and TC probing. The single buckle minimal buckling rotation is found at $\theta = 1.67$ deg, close to the point of spontaneous buckling. Similar to the BR probing, the stability landscape appears truncated at the bifurcation rotation, an the unstable single-buckle equilibrium contour is disconnected from the unbuckled state. It suggests that similar to the BR buckle, the BL buckle can only be formed through snaking or perturbation. For $1.59 < \theta < 1.74$ deg, the stability landscape features a cliff beyond which the probe snaps-back. Similar to the TC and BR probing locations, once the cliff displacement is exceeded, equilibria are found when the probe retracts. For $1.59 < \theta < 1.61$ deg, the TC buckle is found in equilibrium, without the BL buckle being present. The TC buckle quickly evolves to the fully formed buckling pattern above the three buckles minimal buckling rotation, $\theta = 1.61$ deg. Note that the three buckle equilibria can arise at rotations lower than the BL buckle minimal buckling rotation. Contrary to the two previous probing locations, once the stable single BL buckle is formed and the structure follows its stable equilibrium contour, the fully formed buckling pattern will not appear prior to reaching the point of spontaneous buckling.

Energy barriers and early formation of buckling patterns

The stability landscapes revealed that the three buckles belonging to the main post-buckling mode can appear in the structure before the bifurcation point is reached. These equilibria are attained if a perturbation is applied to the structure, as long as it provides enough energy to overcome a critical threshold, the energy barrier. The purpose of this subsection is to compute the energy barrier for the three probing locations (TC, BR and BL), and for all the buckle combinations identified in the previous subsection. For a fixed rotation, the work done by the probe is found

by integrating the probe force as a function of the probe displacement. The energy barrier to form a specific combination of dimples corresponds to the maximum value of probe work found between the unbuckled state ($U_p = 0$ N) and the corresponding buckled equilibria. The energy barriers for the three probing locations are shown in Figure 4.9.

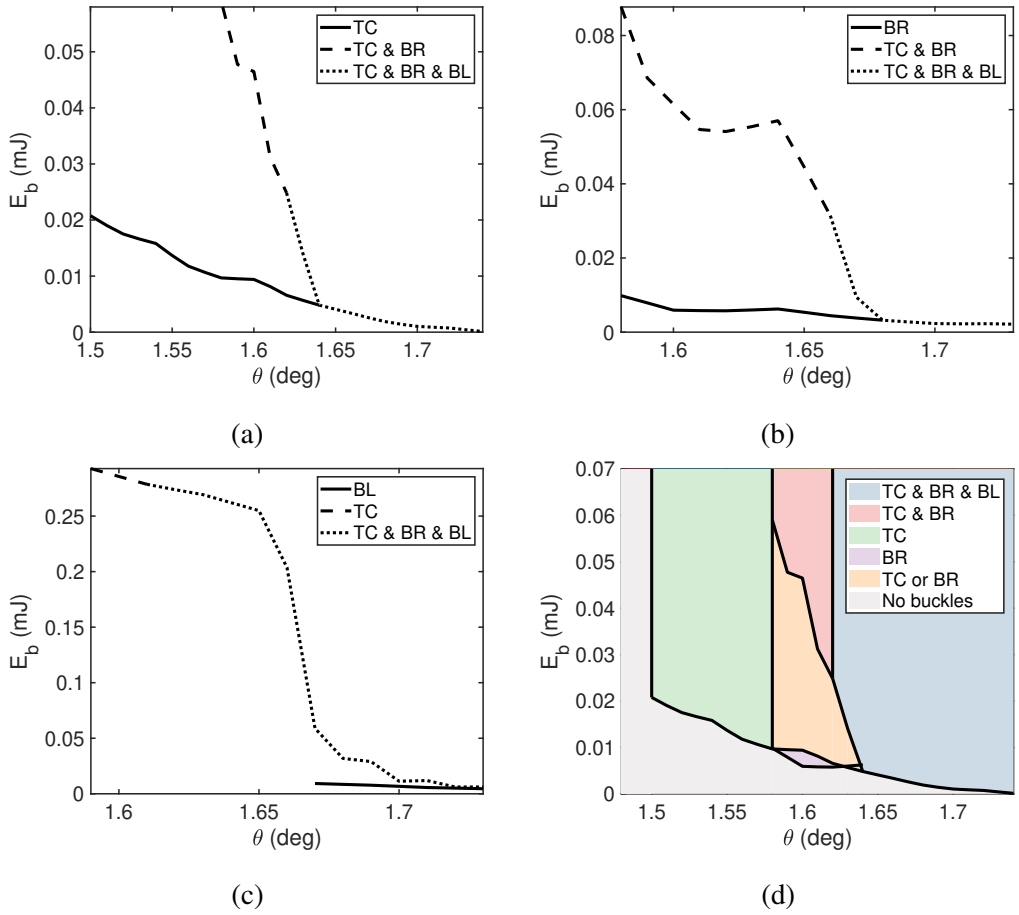

Figure 4.9: Energy barriers required to form specific combinations of buckles before the bifurcation point, for (a) TC probing, (b) BR probing, and (c) BL probing. These energy barrier plots are combined in a (d) transition diagram, giving a more global representation of the structure's meta-stability.

We first focus on the energy barriers computed for the TC probing location, shown in Figure 4.9a. For $1.5 < \theta < 1.64$ deg, forming the TC buckle requires the smallest amount of energy. However if more energy is brought to the structure, the TC & BR buckle configuration can be found, which transitions to the full buckling pattern above the three buckles minimal buckling rotation, $\theta = 1.62$ deg. Above the snaking rotation, $\theta = 1.64$ deg, probing past the unstable TC equilibrium always results in the three buckles pattern formation. The energy barrier decreases continuously until

reaching 0 mJ at the bifurcation point, confirming that the TC buckle appears first in the snaking sequence.

A similar energy barrier distribution is observed at the BR probing location, as shown in Figure 4.9b. The lowest energy barrier branch corresponds to the single BR buckle formation which transitions to the full buckling pattern above the snacking rotation, $\theta = 1.68$ deg. The highest energy barrier branch corresponds to the same buckle combinations found for the TC probing location. The TC & BR buckle disappear to form the full buckling pattern for $\theta = 1.66$ deg. In theory, this rotation should coincide with the three buckles minimal buckling rotation found for the TC probing. In practice, the relative difference between the two rotations is less than 2%, and the small discrepancy can be due to small variations in the structure's initial configuration for the two probing experiments. It should also be noted that the small amplitude of the BL buckle makes its detection difficult. When the rotation increases, the three buckles energy barrier decreases slowly and plateaus without reaching the 0 mJ threshold. It confirms that the BR buckle cannot be formed through a fundamental path bifurcation, and is indeed a broken-away mode.

Finally, the BL probing energy barriers are shown in Figure 4.9c. Two energy barrier branches are found. The lowest energy barrier branch starts at the single buckle minimal buckling load and ends at the bifurcation point, corresponding to the formation of the single BL buckle. Contrary to the TC and BL probing, no full buckling pattern snaking is observed on this energy barrier branch. As previously observed, the energy barrier does not fall to 0 mJ at the bifurcation point, and the single BL buckle is broken away from the unbuckled state. The high energy barrier branch starting at $\theta = 1.49$ deg forms the single TC buckle, which evolves to the full buckling pattern at the three buckles minimal buckling rotation, $\theta = 1.61$ deg. Note that as mentioned before, this specific rotation is in theory identical for the three probing schemes, and here agrees well with the three buckles minimal buckling rotation found for the TC probing location.

The energy barriers for the three probing locations are combined to create the transition diagram of Figure 4.9d. It defines regions in the (E_b-θ) plane, for which the boundaries are given by the minimum energy barrier required to create critical buckle configurations. For a given rotation and energy barrier level, the critical buckle configuration corresponds to the largest set of buckles that can remain in equilibrium. For instance, for $\theta = 1.7$ deg, the single BL buckle has a higher energy barrier than the TC & BR & BL buckle configuration. Since it also belongs

to this larger set found at a lower energy barrier, the single BL buckle is not a critical configuration. In this representation, the probing location is abstracted, and therefore, the energy barrier should be interpreted as a lower bound on the energy required from any perturbation to trigger buckling, regardless of where it is applied on the structure. Above the single TC minimal buckling rotation (θ = 1.5 deg), and below the TC snaking rotation (θ = 1.64 deg), single buckle configurations (TC or BR) always corresponds to the lowest energy barrier. Above the TC snaking rotation, the three buckle configuration (TC & BR & BL) is the easiest to trigger.

4.5 Probing alternate post-buckling modes

The search for critical buckling locations

The previous section focused on studying the main post-buckling mode. For this study, the probing locations were determined after a first buckling test was performed, and the location of local peak displacement marked. This approach requires the structure to buckle in order to determine the probing locations. For the present structure, it is not an issue since the post-buckling regime is stable and the structure remains in its elastic domain after buckling. However, for other types of structure, such as cylindrical shells, buckling can be more dramatic, damaging the structure and causing it to fail [82]. Note that if the locations of localized deformations can be determined beforehand, specific probing methodologies allow prediction of the structure's bifurcation point and minimal buckling load/rotation without triggering any buckling. Recent work on cylindrical shells showed that probing can be used to track the stability landscape's ridge and by extrapolation, find the bifurcation point [1] without ever exceeding it. It is also envisioned that a similar approach can be used to track the stability landscape's valley and by extrapolation, the minimal buckling load [81]. However these techniques face the same challenge: determining the location at which localized buckling will first appear. In recent experiments, a defect was introduced in a soda can to actively control the location of buckling [1] and therefore the location of probing. Even if the introduced imperfection has a small amplitude, altering the structure may not be acceptable for engineering components such as rocket fuel tanks [29] or other aerospace systems. Further analysis showed that probing away from the dominant imperfection can lead to inaccurate buckling load predictions [85].

In the present chapter, a different approach is taken, and probing is used to search for the locations where buckling modes localize. It is used as a tool to navigate spatial chaos without prior knowledge of the expected post-buckling shape. This technique

uses an important observation specific to our problem: the location of maximum compressive stress in any given cross-section is known, and corresponds to the longeron edge. For an axisymmetric cylindrical shell, the search for the critical buckling location would be two dimensional, whereas our problem reduces to one dimension. The longeron's edge in compression is discretized into 17 regularly spaced probe locations, and probing is carried out for at fixed rotations, under the point of spontaneous buckling. In the rest of this section, the results of this analysis are discussed. A schematic of the experiment can be found in Figure 4.10a.

Probing along the longeron's edge and broken-away modes

The experiment is repeated for a small set of rotations, ranging from $\theta = 1.5$ deg to $\theta = 1.7$ deg. For each probe location, the maximum probe displacement is set to $U_{p-max} = 3$ mm. Results for the bottom longeron probing and for $\theta = 1.65$ deg are shown in Figure 4.10b. The probe force is displayed as a function of the probe displacement and the probe location. The interval between probe locations is 36 mm and the probe force is interpolated between measurement points to construct the corresponding probing contour map. In this representation, the maximum probe displacement is limited to 1.5 mm. For larger displacements, global deformations of the structure are induced by probing, and motion of the vertical linear bearing is observed for probe locations over 625 mm. Due to physical constraints (size of the probing stage), the first and last probing locations are offset from the strip ends by half a batten spacing. For visualization purposes, the maximum probe force is capped at 0.45 N and all dark red regions in Figure 4.10b correspond to probe forces above this threshold. The schematic of the strip in Figure 4.10a is aligned with Figure 4.10b such that the probe coordinate directly corresponds to its physical location on the strip.

A periodic pattern of alternating local probe force maxima and minima is observed. The maxima are attained at the locations for which the probe is aligned with a batten. From this simple observation, we can postulate that there can only be a single buckle forming per batten spacing, at a location close to (or at) the midpoint between the two battens. The search problem is then reduced to a discreet set of 10 probe locations (5 for each longeron). A local buckle in equilibrium is found when the probe force falls to 0 N (for a non-zero U_p). Even when the probe force does not reach this critical threshold, a non-monotonic probe force profile indicates the potential for a buckle to form at higher rotations. On the bottom longeron, two of the probe locations have already been studied and correspond to buckle BR and BL of

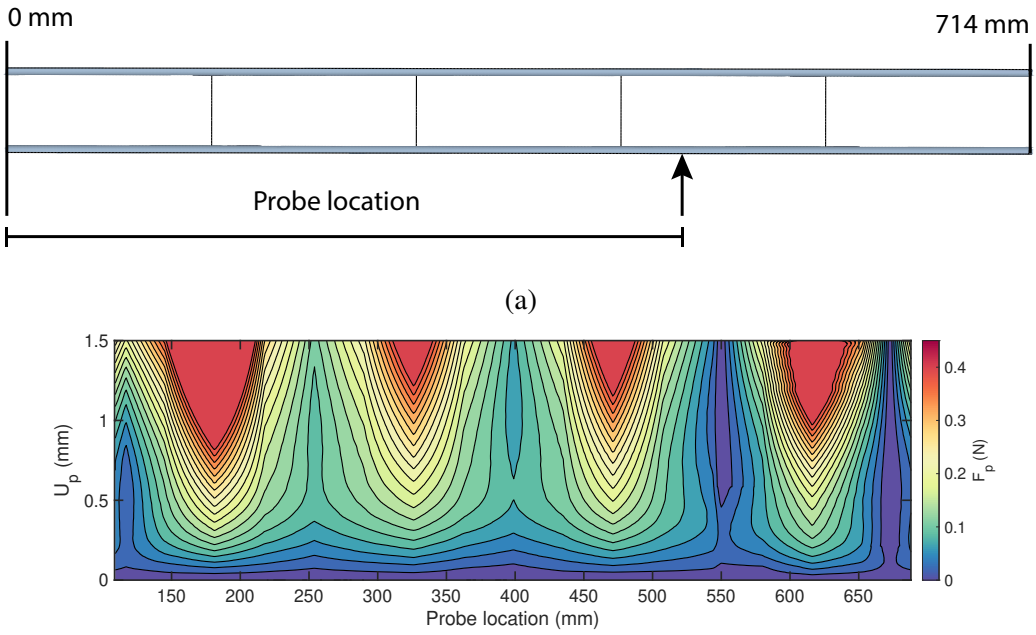

Figure 4.10: (a) Schematic of the edge probing experiment and (b) probe force as a function of the probe displacement and probe location, for $\theta = 1.65$ deg.

Section 4.4. A buckled equilibrium is detected at location BR as found previously, and a local minimum approaching 0 N is found at location BL. As explained before, both buckles are forming through the main snaking sequence, stemming from the TC buckle formation at the bifurcation point.

However, competing buckling locations are revealed. In particular, a buckled equilibrium is located at a probe location of 550 mm. This buckle does not appear in the main snaking sequence, and therefore is not connected to the fundamental path. It is a broken-away mode which can only be triggered if a disturbance is applied on the structure. An important observation is that the location of this mode corresponds to the buckles observed in Figure 4.6d, when the first eigenmode imperfection is seeded in the simulation. This alternate buckle may be the trigger of an alternate snaking sequence, competing with the one observed without perturbations. At a probe location of 250 mm, the probe force profile features a local minimum. However, the minimum probe force is relatively large. Probing at higher rotations indicates that the probe force does not fall to 0 N at this location, before the spontaneous buckling is reached. Finally, the probe force profile at the 400 mm location features a low, but positive minimum. It is also a broken-away mode but corresponds to the

same snaking sequence studied in Section 4.4, when top and bottom longerons are swapped. While in the simulation top and bottom longerons are interchangeable, gravity may bias the structure in the experiment towards the formation of TC rather than its bottom longeron counterpart.

Repeating the experiment on the top longeron yields an almost identical contour map. Local buckling equilibria are found at the probe location TC (as expected from Section 4.4) and at 250 mm, similar to the alternate mode discussed above. Broken away modes are found for the left and right probe locations (counterpart of BL and BR on the top longeron) and belong to the snaking sequence triggered by the bottom central buckle, mentioned in the previous paragraph.

Here, the spacing between probe locations is rather coarse, but adequate for this specific structure. The experiment should be seen as a proof of concept, but other structures may require a thinner discretization. Simulations can be harnessed to compute the probing region of influence and thus determine an appropriate spacing. We can also envision refining the density of probe locations to regions of interest as the test progresses. A more systematic approach to finding buckling locations through probing will be the subject of future work.

Triggering the alternate buckling modes

The previous experiment revealed two alternate locations at which buckling can be triggered. One was found on the bottom longeron, at a probe location of 550 mm, and another one on the top longeron, at a probe location of 250 mm. For the rest of this section, these two probe locations are called BA (Bottom edge Alternate) and TA (Top edge Alternate). In the following, probing is conducted at these two locations for $1.2 < \theta < 2$ deg. The initial rotation increment is 0.05 deg, and is then refined to 0.02 deg above $\theta = 1.55$ deg. The corresponding stability landscapes are shown in Figure 4.11.

We first focus on the BA probe location for which the landscape is shown in Figure 4.7a. For rotations below the point of spontaneous buckling, the stability landscape is similar to the ones found for the TC, BL, and BR probe locations. It features a ridge and a valley both starting at $\theta = 1.31$ deg. The minimal buckling load to sustain the BA buckle in equilibrium is $\theta = 1.59$ deg. The minimally buckled state marks the start of the single-buckle stable and unstable equilibrium contours. At the structure's bifurcation point, at $\theta = 1.74$ deg, there is still a significant hill of probe force separating the unbuckled state and the unstable equilibrium contour. At

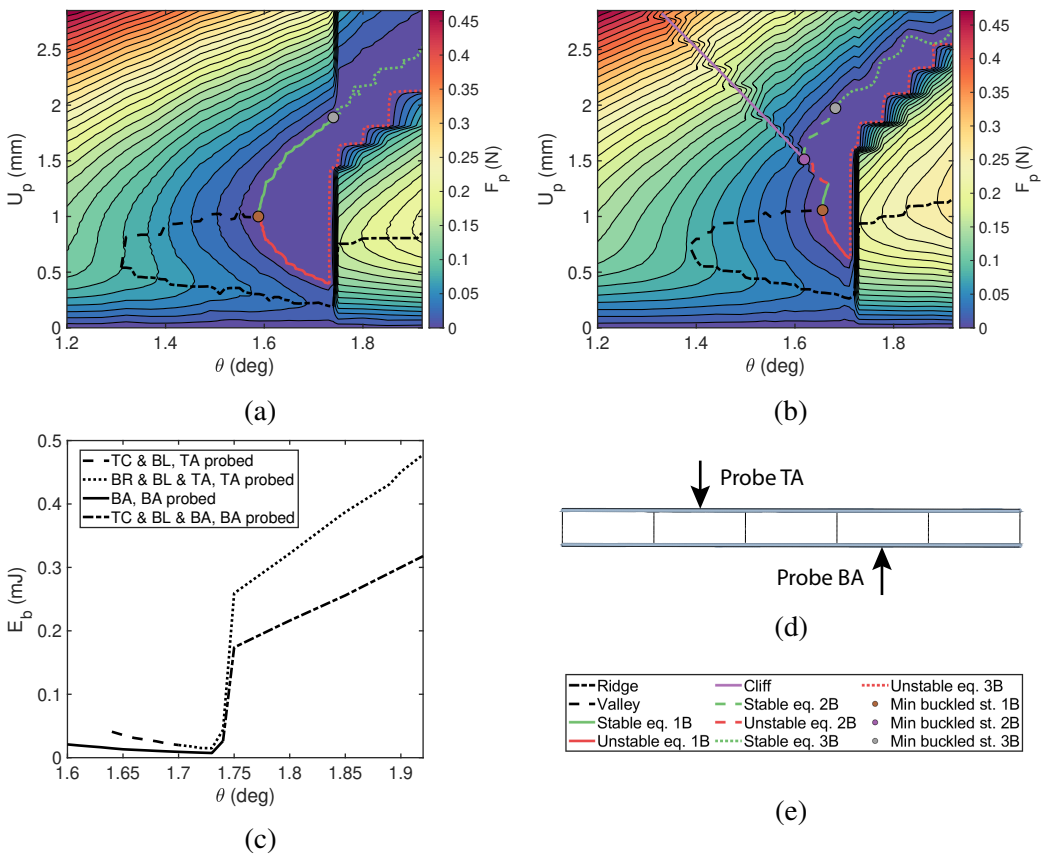

Figure 4.11: Stability landscapes for the (a) BA probe location, (b) TA probe location, and (e) their common legend. (c) Energy barriers for the BA and TA probe locations and (d) schematic of the strip structure with the two probe locations.

this critical rotation, and in the absence of the BA buckle, the structure's main post-buckling mode forms, as seen in Figure 4.6e. For $\theta > 1.74$ deg, $U_p = 0$ mm does not correspond to the unbuckled state anymore, but to the end of the main post-buckling snaking sequence, and probing is applied to the buckled structure. For these large rotations, the probing behavior changes significantly. The initial probe characteristic is steeper and creates a large offset of the ridge to $U_p = 0.8$ mm, and an extensive region of higher probe force magnitude. When the probe displacement increases further, the structure experiences a snap-back and the unstable three buckles (BA & BL & TA) equilibria are found. This new landscape topology can be explained as follows. Once the structure takes the shape of its main post-buckling mode, the formation of buckle BA requires buckle BR to disappear, which requires large probe forces to be applied at the probe location. Notice that if the BA buckle is formed before the bifurcation point, the buckled equilibrium evolves to the three buckles (BA & BL & TA) configuration for $\theta > 1.74$ deg.

The TA probe location is then considered and the corresponding landscape is shown in Figure 4.7b. It features a ridge and a valley that both start at $\theta = 1.39$ deg and a single buckle minimal buckling rotation at $\theta = 1.66$ deg. The TA buckle is also a broken away mode and at the bifurcation point, the unstable equilibrium contour is farther away from the unbuckled state than it was for the BA buckle. It suggests that the TA buckle is harder to trigger. At higher rotations, the behavior is similar to what was observed at the BA location. A large region of high magnitude probe forces is encountered between the unbuckled state and the unstable equilibrium contour. It physically corresponds to the probe force required for the TC buckle to disappear and subsequently form the TA buckle. The TC buckle has the largest amplitude among the three buckles found in the main post-buckling mode and therefore, more probe work needs to be supplied to the structure to close it. It explains that at the TA probe location, the region of high probe forces extends to larger probe displacements. The main difference between the BA and TA probe locations is the nature of the stable equilibria encountered while probing. At the BA location, only the formation of the BA buckle was observed whereas, three buckle configurations can be triggered from probing at the TA location. For $\theta < 1.62$ deg, the probe characteristic features a cliff, similar to the TC, BR, and BL landscapes (Section 4.4). When the cliff is reached, the structure experiences a snap-back caused by a fold (cusp catastrophe), and the bottom left buckle (BL) is triggered. However no equilibrium solution is found for the BL buckle when retracting the probe. The cliff converges to the two buckles minimally buckled state, found for $\theta = 1.62$ deg. It marks the start of the two buckles stable and unstable equilibrium contours on which the TC and BL buckles can coexist. The stable single buckle and unstable two buckles equilibrium contours meet at the snaking rotation, $\theta = 1.67$ deg. Finally the two buckles equilibra evolve to the three buckles equilibria (TA, BR, and BL) for $\theta > 1.68$ deg.

Similarly to the analysis of Section 4.4, the probe force/displacement characteristic is integrated to compute the energy barrier for the various buckle configurations. The results are shown in Figure 4.11c. For both probing locations, the energy barrier features two regimes. Under the bifurcation rotation, the energy barrier is low ($E_b < 0.05$ mJ). After the main post-buckling mode forms, the energy barrier increases by almost an order of magnitude. As explained previously, this increase can be explained by the extra amount of energy that needs to be provided to the structure to make the BR and TC buckle disappear. For the entire range of rotations, probing at BA yields a lower energy barrier. Therefore, it is the critical alternate mode, and the most likely to appear first if a perturbation is applied to the structure.

Note that in the energy barrier plot for the TA probing, the energy barrier for the single TA buckle is not reported since it only corresponds to a very short range of rotations (0.01 deg). The present analysis highlights that it is possible to form alternate modes, disconnected from the unbuckled state, and that switching between paths in the post-buckling regime is achievable, but requires significantly more energy. The energy barriers for the TA and BA probe locations are compared to the energy barrier found for the TC probe location, in Figure 4.12a. As a reminder, TC is the critical buckle for the main post-buckling mode, as it requires the least amount of energy to be formed. The energy required to form the BA buckle is about twice the energy required to form the TC buckle, and can only be formed above $\theta = 1.6$ deg, whereas the TC buckle can be formed above $\theta = 1.5$ deg.

Similarly to Section 4.4, the energy barriers of Figure 4.11c can be combined to create the transition diagram of Figure 4.12b. As previously explained, boundaries in the (E_b-θ) plane are given by the minimum energy barrier required to create the critical buckle configurations. For a given rotation, they correspond to sets of dimples that can remain in equilibrium in the structure. For the alternate probing locations, the diagram features three regions. The two regions found for higher energy barriers correspond to the buckles triggered while probing at the TA location. The critical alternate mode BA, encloses these two regions, and is reached for lower values of energy barrier. The alternate transition diagram is superimposed on the main post-buckling transition diagram (doted lines) of Figure 4.9d. The resulting plot is a valuable tool to represent the competition between buckle configurations, characteristic of the structure's meta-stable state close to the spontaneous buckling rotation. It reveals for instance that the alternate buckles mostly compete with the early formation of the main three-buckle mode (BR, BL, and TC), but that they require more disturbance to be triggered.

Alternate buckling sequence and large rotations

In this subsection, we explore the structure's post-buckling response for large rotations. In Section 4.3, we saw that the strip's main post-buckling path is stable and that the structure is able to withstand bending moments larger than its spontaneous buckling moment. Of particular interest is the maximum load-bearing capacity of the structure before failure. Here failure means that the structure reaches a stiffness of 0 and corresponds to a horizontal tangent in the moment/rotation characteristic.

Without any disturbance applied to the structure, the main post-buckling mode

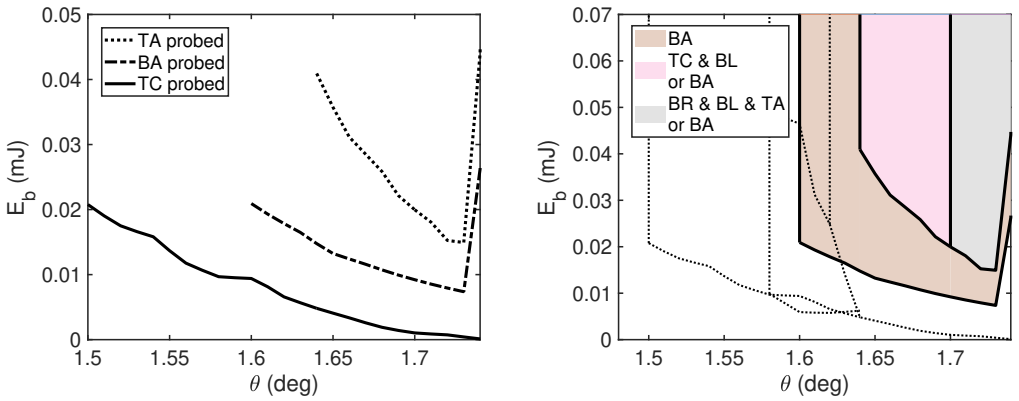

(a) (b)

Figure 4.12: (a) Energy barrier comparison between the TC, BA, and TA probe locations and (b) transition diagram characterizing the formation of the alternate buckling modes. The transition diagram for the main post-buckling mode is shown in dotted lines.

appears when the spontaneous buckling rotation is exceeded. It consists of local buckles at location BR, BL, and TC, as seen in Section 4.3. The full main post-buckling response is shown in Figure 4.13a, as a solid line. As the rotation increases after buckling, the amplitude of each buckle increases progressively, and a global in-plane bending of the strip is observed. The maximum moment, $M_{max} = 2.35$ Nm, is reached at $\theta = 8.7$ deg. Beyond this critical rotation, the structure experiences a snap-back. It physically corresponds to a large increase in the TC buckle amplitude, which makes the cross-section almost flat locally. Note that this specific mode of failure has been observed previously for similar structures [69]. The deformed shape obtained at the end of the bending experiment is shown in Figure 4.13b.

Next, we consider a small perturbation applied to the structure. Probing is conducted at the BA probe location such that the critical alternate buckle is formed right before the spontaneous buckling rotation. We wish to understand the consequences of the alternate buckle formation on the full post-buckling regime. The previous subsection demonstrated that the BA buckle can be sustained in equilibrium in the structure. It is important to understand whether this specific buckle can be the start of an entire alternate snaking sequence, similar to the role of the TC buckle in triggering the main snaking sequence. In other words, we aim to determine if the competition between two local buckles, TC and BA, can yield significant differences in the structure's global response. After the point of spontaneous buckling is passed, additional buckles form simultaneously at location BL and TA, and buckle BA remains. The

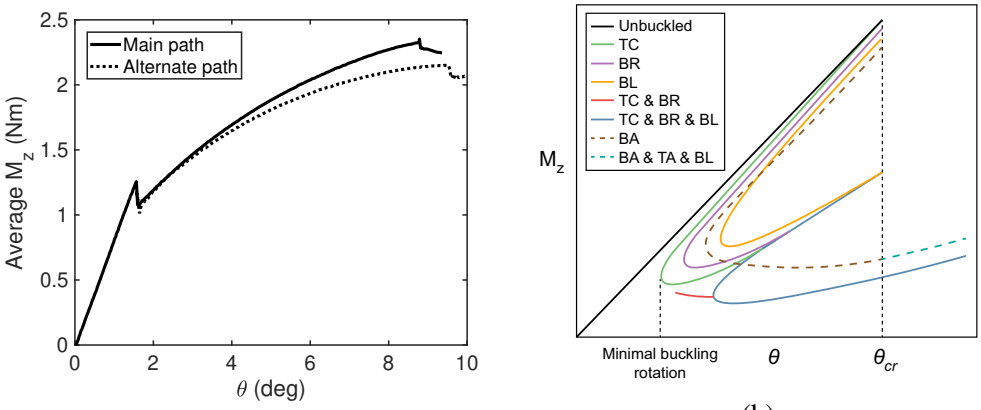

(a) (b)

(c)

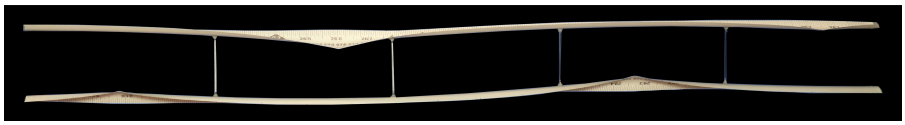

(d)

Figure 4.13: (a) Full post-buckling response obtained for the main (connected by bifurcation) post-buckling path, and for the alternate (broken away) post-buckling path. (b) Schematic of the paths leading to the main and alternate post-buckling deformed shapes. (c) Main post-buckling deformed shape and (d) alternate post-buckling deformed shape.

rotation is increased to trace the entire post-buckling characteristic, shown in Figure 4.13a, as a dotted line. The main and alternate post-buckling paths are similar until $\theta = 2.6$ deg. At this rotation, an additional buckle forms on the top longeron, in the middle of the rightmost batten spacing. After this rotation is exceeded, the main and alternate post-buckling responses diverge, and the alternate post-buckling path shows a decreased stiffness. It ultimately yields a lower value of maximum moment, $M_{max} = 2.15$ Nm, reached for a higher value of rotation, $\theta = 9.5$ deg. The deformed shape obtained at the end of the alternate post-buckling path is shown in Figure 4.13c. At $\theta = 9.5$ deg, the structure experiences a snap-back corresponding to the sudden increase in the TA buckle's amplitude. Similar to the main post-buckling deformed shape, the cross-section becomes locally flat. For the main deformed

shape, two alternating buckles are separated by a double batten spacing wavelength, whereas the interval between buckles goes from a double batten spacing in the middle to a single batten spacing on the sides in the alternate deformed shape.

These experiments highlighted two competing post-buckling sequences, stemming from the TC and BA buckles. From the stability landscapes and energy barriers found in Section 4.4 and 4.5, the multiple post-buckling paths leading to these two sequences are illustrated in Figure 4.13b. Here, a possible arrangement of these paths is drawn qualitatively. With the current experimental setup, it is possible to record the bending moment while probing, and therefore locate these paths exactly in the moment/rotation plane. This will be the subject of future work. From a global response point of view, we saw that if a small amount of energy disturbs the structure and triggers the BA buckle, the maximum moment decreases by 9% and a lower bending stiffness is achieved above $\theta = 1.6$ deg. It also yields different deformed shapes. While both characteristics are stable and the difference in behavior can be seen as minor, it will not necessarily be the case in all structures, and a competition between local buckles could cause dramatic differences in post-buckling response and stability.

4.6 Conclusion

Bending experiments were conducted on a specific kind of thin-shell structure, consisting of an assembly of open cross-section tape springs connected transversely by thin rods. Similar structures are used in large deployable spacecraft [18, 19]. One of the most important characteristic they feature is a stable post-buckling regime under bending, and they can therefore carry a load even after they first buckle. This characteristic opens new design possibilities in which these structures are used closer than ever to their buckling load, and even in their post-buckling regime. By doing so, their mass efficiency can be dramatically improved by relaxing stringent safety factors often applied to the buckling load.

The study used an experimental probing method to characterize the structure's meta-stability close to the buckling load. By locally displacing the longeron's edge in compression, and recording the probe force for various values of rotation, stability landscapes were constructed and used to characterize the stability of each of the local buckles forming the experimentally observed post-buckling mode. Of particular interest was the determination of the minimum rotation at which these buckles can appear in the structure, and the level of disturbance that the structure

required to form these buckles early. A transition diagram was derived from these experiments and defined regions in the (E_b-θ) plane for which specific combinations of buckles can appear. If buckling is to be avoided, the transition diagram can serve as a tool to derive a tighter lower bound on the actual buckling rotation, found in a real environment in which perturbations and imperfections are present. A minimum value of energy barrier, and maximum number of buckles can also serve as buckling criterion, and a critical rotation can then be determined from the diagram.

The methodology was then extended to probe the longeron's entire edge. It allowed the detection of two broken-away modes. They are disconnected from the structure's fundamental path, but accessible if a disturbance is applied to the structure. They directly compete with the main post-buckling mode. For the specific test structure presented in this chapter, the energy barrier required to trigger the alternate modes is about twice the one required to create the main critical buckle. However, additional tests on other samples revealed that the two energy barriers can sometimes be almost identical, and that these alternate modes cannot be neglected. Probing these modes yielded an alternate transition diagram than can be superimposed on the main buckling transition diagram, and gave a complete picture of the structure's meta-stability close to buckling. The analysis also showed that the alternate buckles can also be triggered after the main post-buckling mode appears, but it requires more energy. Finally, large rotation experiments were performed and showed that the formation of the critical alternate buckle triggers a full snaking sequence featuring four buckles, as opposed to three for the main post-buckling snaking sequence. The two competing responses yielded different maximum moments and bending stiffnesses for large rotations. It highlighted that characterizing the structure's response for all possible buckling modes is crucial, if the structure were to be used in its post-buckling regime.

Finally, this study emphasized that in order to design and operate thin-shell structures near their buckling point, and in their post-buckling regime, finite element simulations are helpful but not sufficient to characterize all the possible responses. The finite element analysis of Section 4.2 did in fact predict the two competing post-buckling shapes observed in experiment. However, while the lowest bifurcation and therefore the connected path is in theory obtained for the first eigenmode imperfection, the solution obtained for the second eigenmode imperfection was in fact observed in experiment. Intrinsic imperfections in the real geometry biased the structure to behave dominantly following its second eigenmode. In the framework

developed here, the engineer would consider the whole set of theoretical post-buckling solutions and for each of them focus on characterizing their stability and the energy needed to form them. This approach paves the way to highly optimized buckling criteria tailored to specific applications. Imperfection insensitive structures have been seen as an alternative approach to reducing buckling uncertainty. Such designs have been explored for particular structures such as cylindrical and spherical shells [59, 60], and the probing methodology could serve as an efficient tool to enable more complex imperfection insensitive structures to be built.

Chapter 5

ULTRALIGHT LADDER-TYPE COILABLE SPACE STRUCTURES

Nomenclature

A: total area of strip
A_{BL}: area of longeron webs and battens
b: batten cross-section width
d: longeron cross-section web width
h: batten cross-section height
L: strip length
P: pressure applied on area A
P_{AB}: pressure applied on area A_{BL}
P_{cr}: non-linear buckling pressure
P_{cr-lin}: linear buckling pressure
P_M: Minimum post-buckling pressure
P_{max}: Maximum post-buckling pressure
r: longeron cross-section radius
s: batten spacing
t: longeron flange thickness
W: strip width
Z: probe location along strip axis
θ: longeron cross-section opening angle

Terminology

Brief descriptions of the key terminology used in the chapter are provided here.

- **Linear buckling eigenvalue/load**: buckling eigenvalue estimate obtained by solving the buckling eigenvalue problem for the undeformed structure.
- **Non-linear buckling eigenvalue/load**: buckling eigenvalue estimate obtained by iteratively solving the buckling eigenvalue problem as the structure is loaded. A first buckling eigenvalue prediction is performed without any pre-load. This first estimate gives the linear buckling eigenvalue. The structure is

then pre-loaded under the linear buckling eigenvalue and a second buckling eigenvalue prediction is performed. This step is repeated until the pre-load converges to the buckling eigenvalue estimate, to give the non-linear buckling eigenvalue. The associated mode shape is denoted as the non-linear buckling mode.

- **Minimum post-buckling load**: load at which a specific post-buckling path restabilizes. This is the lowest load reached on the post-buckling path, unless no stable paths exist in the post-buckling regime. Note that the structure can reach lower load values if there exist bifurcations on the stable post-buckling path. In this case, one will associate one minimal post-buckling load with each bifurcation.

- **Maximum post-buckling load**: ultimate load that can be sustained by a structure before it loses its overall stiffness.

5.1 Introduction

Thin-shell structures have been used extensively for aerospace applications as they enable lightweight vehicles. Since the early 1920s, discrepancies between shell buckling experiments and theoretical buckling predictions based on linear bifurcation analysis based on perfect shell geometries were observed. The experimental buckling loads were lower than the analytical predictions and the discrepancy was later linked to the presence of initial imperfections in the shell geometry [13, 44, 82]. Considerable efforts were made to find safe lower bounds for the buckling load of these structures, which led to the NASA space vehicle design criteria for the buckling of thin-walled circular cylinders (NASA SP-8007) [62].

Today, these empirical buckling criteria are still used but are seen as very conservative, and have some inherent limitations. To address these shortcomings, the NASA's Shell Buckling Knockdown Factor (SBKF) Project was established in 2007 to develop less-conservative, robust shell buckling design factors by testing shells with known imperfections, as well as non-uniformities in loading and boundary conditions [29]. The introduction of precisely engineered imperfections in spherical shells showed that buckling could be accurately predicted if the initial geometry is known accurately [51]. However, in many applications, measuring the shape of the structure before use can be both expensive and difficult. The traditional buckling and post-buckling prediction method uses a linear combination of the first buckling modes as imperfection [66, 68] and showed increased accuracy compared to the

classical linear bifurcation approach. The importance of local deformations at the onset of buckling was linked to localization effects that cannot be described as a combination of eigenmodes [65].

In particular, post-buckling paths exhibiting localization are found in cylindrical and spherical shells. In most cases, these paths are broken away from the fundamental path but approach it asymptotically, and can be reached before the first eigenvalue is attained if a small amount of disturbing energy is input into the structure [32, 34]. For these early buckling routes, the structure exhibits a single-dimple localized deformation and sits on a ridge of total potential energy separating the pre-buckling energy well and a lower energy, localized post-buckling well. This mode of deformation is thus called mountain pass point and it has been shown that the single dimple corresponds in fact to the cylindrical shell lowest mountain pass point [32], i.e. the post-buckling solution that can be reached with a minimal energy barrier. An experimental procedure to determine the fundamental path meta-stability was proposed in 2013 [76] and has been used experimentally [81]. Comparisons with earlier work showed that the onset of meta-stability often referred to as "shock sensitivity" [76] gives an accurate lower bound for experimental buckling loads [20, 23].

The objective of the present chapter is to apply these recent breakthroughs in understanding cylindrical and spherical shell buckling to more complex thin-shell structures made of composite materials. In particular, the present authors are currently investigating structural architectures for ultralight, coilable space structures for large, deployable, flat spacecraft [3]. In the deployed configuration, each spacecraft measures up to 60 m $\times$ 60 m in size and is composed of ultralight ladder-type coilable strips of equal width, arranged to form a square, and each strip supports many photovoltaic and power transmission tiles. This structure is described in a previous paper [71] and is shown in Figure 5.1. Scaled laboratory prototypes of this structural concept have been built and tested [18, 19].

A ladder-type structure consists of two triangular rollable and collapsible (TRAC) [57] longerons, connected transversely by rods (battens), and will be referred to as a *strip* in this chapter. In the proposed spacecraft architecture, the strips are simply supported at the ends with boundary conditions that do not allow any tension to be applied. For the specific strip considered in the present study, the battens are rectangular cross-section carbon fiber rods and the longerons are thin composite shells. In orbit, the main loading is solar pressure, and hence a static pressure is the

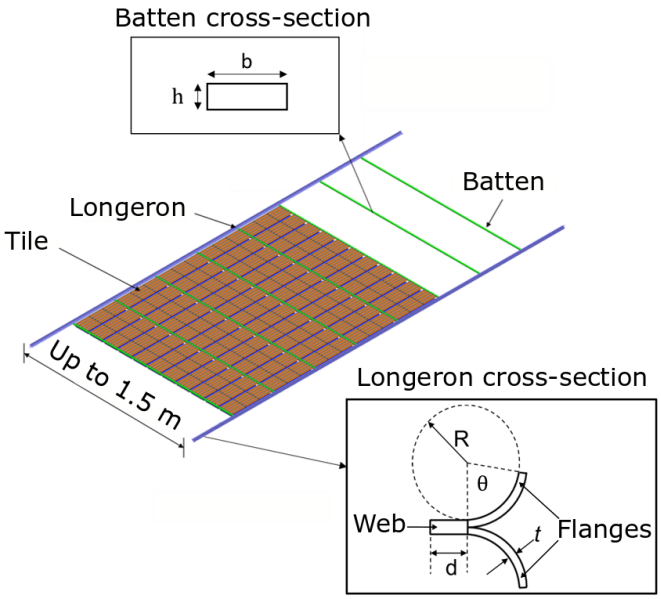

Figure 5.1: Overview of the ladder-type structure for the Space-based Solar Power Project.

main loading condition that will be considered.

The purpose of the present study is to understand and quantify the buckling and post-buckling behavior of a strip, and explore the sensitivity of its transition to buckling, considering the effects of disturbances and imperfections. Recent work studied the longeron's deployed behavior and showed that localized buckles form under transverse bending, and that the post-buckling regime immediately after the first bifurcation restabilizes quickly. The studies focused on replicating experimental results using non-linear buckling and post-buckling simulations [8, 48, 49, 56], and further work used non-linear buckling load computations coupled with modern machine learning techniques to design optimized longeron geometries [10].

The present study takes a different approach. The stability of the pre-buckling (fundamental) path is assessed, and insights into early transitions into the post-buckling regime are gained by using localized probing to apply a perturbation to the structure. The probing technique is then generalized to higher order bifurcations arising from the post-buckling path. Low energy escape paths into buckling that cannot be predicted by a classical eigenvalue problem are identified.

The chapter is structured as follows. Section 2 highlights some experimental observations on the buckling of a strip, and Section 3 reviews the concept of stability landscape for thin shell buckling, which is used in the rest of the chapter. Section 4 presents the numerical computation of stability landscapes for a specific strip structure, and Section 5 extends the use of these landscapes to the post-buckling regime. In Section 6 the effect of the strip length on the stability landscape is investigated. Section 7 generalizes the probing to the entire structure, unveiling the existence of low energy escape paths into buckling, similar to the low energy paths observed for the cylinder and the sphere. Finally, Section 8 presents a preliminary analysis of the effect of geometrical imperfections on the strip stability landscape.

5.2 Experimental observations on strip buckling

A 0.8 m long strip prototype with 3 battens spaced at 0.2 m was built and tested in the cantilever configuration shown in Figure 5.2b. The longeron end cross-sections at one end of the structure were built into a stiff plate and the cross-sections at the other end were attached to a stiff composite rod. These boundary conditions did not allow the end cross sections to deform. Two load cells mounted on an acrylic beam were attached to a translation stage, and were placed in direct contact with the two longerons ends (using steel balls). When actuated, the linear stage displaced the two longeron ends and the reaction force at each end was measured. The end displacements of the longerons were also measured, using laser displacement gauges.

The results of this experiment are shown in Figure 5.2a and the buckles that were observed are shown in Figure 5.2b. It can be seen that longeron 2 is 10% softer than longeron 1, due to a slightly smaller cross-section introduced by the manufacturing process. The two longerons exhibit different buckling behaviors. A local buckle at the location of the first batten connection appears (buckle 1 in Figure 5.2b) in longeron 2 for a tip deflection of 1.5 mm. As the tip deflection is increased, a gradual softening of longeron 2 is observed which physically corresponds to the growth of buckle 1. No other buckles appear in longeron 2. For longeron 1, the linear regime extends to a tip deflection of 2.5 mm, then the first buckle (buckle 2) appears close to the cantilever base. Unlike longeron 2, the behavior of longeron 1 after the appearance of buckle 2 is linear. A second buckle (buckle 3) appears 0.5 m away from the cantilever base, for a tip deflection of 8.5 mm. The postbuckling regime of longeron 1 after the formation of buckle 3 is also linear. Finally, unstable buckling of longeron 1 occurs for a tip deflection of 17.5 mm (buckle 4). At this

point buckle 3 disappears. This ultimate buckling is of a different type and consists of a doubly-curved S-shaped flange deformation, which creates a localized region of very high curvature and leads to the formation of a crack at this location. Since the two longerons are connected at the tip by a carbon fiber tube, the drop in reaction force in longeron 1 is accompanied by a sudden increase of reaction force in longeron 2.

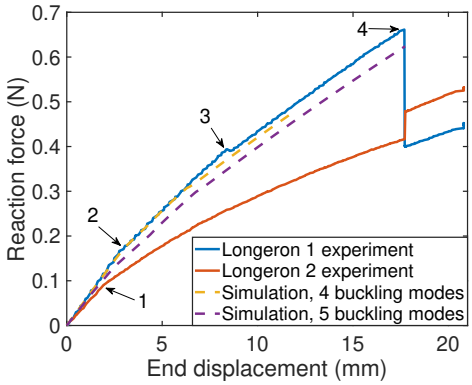

(a)

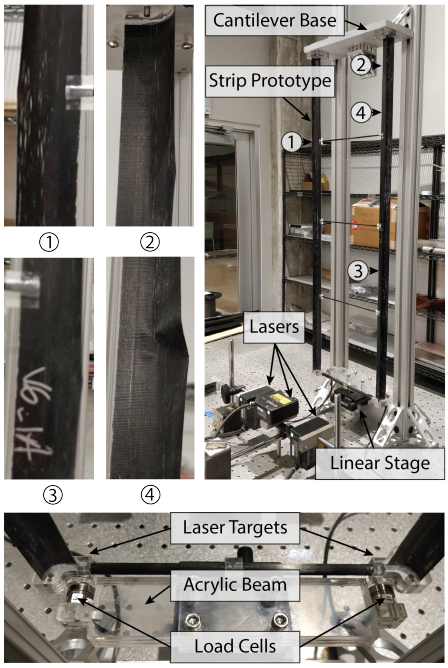

(b)

Figure 5.2: (a) Evolution of longeron reaction forces as a function of longeron tip displacements. The simulation results are for longeron 1. (b) Experimental setup and local buckles on the longerons. Each buckle location is indicated by its number in (a).

Based on this experiment, the following observations can be made regarding the behavior of the tested structure:

- Both longerons exhibited a long and stable post-buckling regime, until ultimate buckling occurred for a rather large tip deflection of 17.5 mm. For longeron 1, the ultimate buckling reaction force was 4.8 times larger than the first buckling reaction force, and 5 times larger for longeron 2. Each buckling event was quasi-static.

- The buckles forming in the longerons were very localized and consisted of a single wave. Therefore, local deformation played a key role in the buckling of the test structure, in analogy to the previously observed subcritical buckling behavior observed in spherical and cylindrical thin shells.
- Imperfections and deviations from the nominal geometry played a key role in the longeron behavior. Since more local variations in the shape of longeron 2 were observed, these imperfections were the likely origin of the gradual softening behavior observed in the experiment, as opposed to the sudden change of slope observed for longeron 1 (which has smaller shape deviations).

A finite element analysis was carried out to numerically reproduce some aspects of the experiment. A classical post-buckling approach was used, which consisted in seeding a linear combination of buckling modes into the longerons initial geometry to resolve the bifurcations and their post-buckling branches. Two attempts are shown in Figure 5.2a, respectively using the first 4 and the first 5 non-linear buckling modes as imperfection. The total imperfection amplitude in the second attempt was about twice that used in the first attempt. The results shown refer to longeron 1. Qualitatively, the first attempt captured well the first buckling of longeron 1, but the the second post-buckling transition occurred much earlier than in the experiment. Convergence could no longer be achieved after a displacement of about 12 mm. Numerical convergence up to ultimate buckling was achieved, but the imperfections needed to resolve all buckling events degrade the initial pre-buckling path, causing an early transition into the first post-buckling regime. These observations qualitatively highlight the difficulties encountered while trying to model a series of subsequent buckling events using seeded imperfections into the initial geometry [28].

This discussion indicates that it is important to quantify the post-buckling regime of strip structures, as significant load-carrying reserves may be available beyond the first buckling. Regarding the applicability of the present results to more general cases, it should be noted that the bending moment distribution for the strip in this experiment is non-uniform, which may influence the localization behavior and the extent of the post-buckling regime.

5.3 General stability landscape approach to thin shell buckling

Recent work on thin cylindrical and spherical shell buckling has focused on the stability of the buckling phenomenon and its sensitivity to disturbances. Rather than seeing buckling purely as a bifurcation problem, these new contributions have

studied in more detail the meta-stability of a structure's fundamental path and the early transition into adjacent post-buckling paths requiring small energy barriers to be overcome. A review of these recent advances has been presented by Groh et al. [23].

Following these developments, the approach to shell buckling that is adopted in this chapter uses the buckling stability landscape, a recently developed tool to study these phenomena. The notion of a stability landscape was introduced by Virot et al. [81] as a way to characterize the meta-stable nature of cylindrical thin-shell buckling. Virot et al. imposed a local radial displacement on a compressed cylinder, using a small ball probe (called a "poker" in [81]) which creates a localized single dimple. The stability landscape is the surface created when the probe force is plotted as a function of the probe displacement for various levels of the main loading parameter (axial compression or end-shortening of the cylinder). It provides a useful way to quantify the impact of probing on the buckling behavior and a general way to study buckling sensitivity of a structure to disturbances.

Even though the stability landscape was introduced for thin cylindrical shells, a similar landscape can be found for other types of shell buckling problems. A thin shell buckling stability landscape is sketched in Figure 5.3a. For the specific scenario shown here, there exists a range of prescribed loads for which stable equilibrium solutions exists. This is not always the case. The features of this landscape and their significance, described in [81], are briefly summarized next.

- **Point of spontaneous buckling**. This point corresponds to a zero probe displacement and the associated load is the non-linear buckling load. No disturbance is needed for the structure to transition into its post-buckling regime from this point.
- **Minimally buckled state**. The minimally buckled state corresponds to the load below which no buckles can form in the structure, whereas buckled states can exist above this load. This load corresponds to the load for which the probe force first falls to zero for a non-zero probe displacement. Below this load, the probe force does not drop to zero even for large probing displacements. Thus, the minimally buckled state represents the onset of metastability. This load can serve as an accurate bound for experimental buckling loads [20, 23].
- **Buckled equilibria solutions**. For loads above the minimally buckled state, there exist two states of equilibrium on the contour of probe force vs. probe

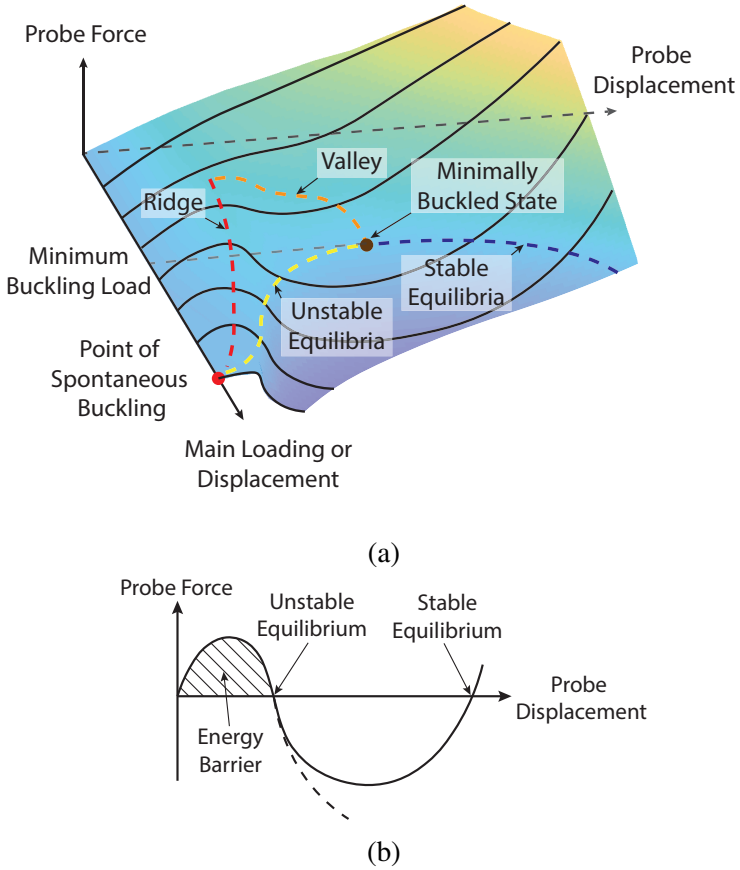

Figure 5.3: (a) Schematic of thin-shell buckling stability landscape, inspired from [81]. The x-axis represents either a prescribed load or a prescribed end-displacement. (b) Energy barrier between pre-buckled and post-buckled states, at a given level of loading. If no stable buckled equilibrium solutions exist, the probe force vs. probing displacement curve will follow the dashed line.

displacement where the probe force is zero for a non-zero probe displacement: an unstable state and a stable state. These two states are connected via the contour plotted in Figure 5.3a. The two states coalesce at the load associated with the minimally buckled state. In a probing experiment where the probe is not glued to the structure, the structure will dynamically snap to the stable equilibrium state as soon as the probe attains the unstable equilibrium state. It is important to realize that the details of the stable buckled equilibrium state, and even its existence, depend on whether the overall loading applied to the structure is load-controlled or displacement-controlled (or some combination in between). For example, a spherical shell buckling under external pressure has a stable buckled state when loaded under volume-control but has no stable

buckled state (other than complete collapse) under pressure control. Note that the unstable equilibrium contour intersects the fundamental path at the point of spontaneous buckling in Figure 5.3a. In some situations, offset post-buckling paths exist for which the unstable equilibrium contour never intersect the fundamental path. Such situations are discussed in Section 5.7.

- **Valley**. At loads below those associated with the minimally buckled state, a valley in the stability landscape is associated with the local minima of the probe force. This contour of positive local minima terminates at the minimally buckled state.

- **Ridge**. The ridge is the locus of local maxima of the probe force. Each local maximum in the probe force is associated with an energy barrier between the stable unbuckled state and the unstable buckled state, as indicated in Figure 5.3b. For any applied load, the energy barrier is the minimum energy that must be imparted to the structure by a disturbance to cause buckling. The energy barrier as a function of the applied load is directly related to the buckling sensitivity or "shock-sensitivity" [76] of the structure to disturbances. Note that the point of intersection between ridge and valley marks the appearance of a negative probing stiffness. At loads above this level, kinetic energy (snapping) would be released in a load-controlled probing experiment.

5.4 Computation of strip stability landscape

Finite element model

A finite element model (FEM) of a strip, composed of two longerons of length L in the range 1.8 m to 4.2 m, was developed. The geometry of the structure is described in Figure 5.1. The cross-section has an opening angle of $\theta = 100$ deg, radius $r = 12.2$ mm, thickness $t = 98$ μm, and web length $d = 8$ mm. The two longerons are connected by regularly spaced transverse rods, called battens, at spacing $s = 0.3$ m. The batten length is approximately equal to the width of the strip, $W = 0.2$ m, and its rectangular cross-section has width $b = 3$ mm and height $h = 0.6$ mm. The longeron flanges are made of a [±45 GFPW / 0 CF /±45 GFPW] laminate, known as FlexLam [64], where GFPW refers to glass fiber plain weave and CF refers to unidirectional carbon fiber. The two flanges are connected with a ply of glass fiber plain weave at the web.

The FEM was built using the Abaqus 2019 commercial software. The longerons were modeled with 4 node reduced integration shell elements (S4R) and the battens

with linear 3D beam elements (B31). The element size is 2 mm and is chosen such that the eigenvalues and eigenmodes of Figure 5.5a have converged to their mesh independent value.

Finite element analysis

The strip structure was held in a simply-supported condition, as shown in Figure 5.4. The outer web edge (highlighted in orange) on one of the longeron cross-sections was prevented from translating in any direction while the web edges of all other end cross-sections were constrained in a way that allows the projections of the strip length and width onto the (xz) plane to vary. Details on these boundary conditions are provided in Figure 5.4.

A uniform pressure was applied on the longeron webs and on the battens' top faces. The total area loaded by pressure in the numerical model is A_{BL} (where BL denotes battens and longerons), and the associated buckling pressure is called P_{cr-AB} (were AB denotes Abaqus). However, in an actual structure, a thin membrane would be attached to the edges of the longerons and hence the loading (solar pressure) would act on the entire area $A = L \times W$ spanned by the structure. In order to emphasize the practical significance of the present study, all results are presented in terms of P, although P_{AB} is actually used in the analysis. The two pressure values are related by $P \times A = P_{AB} \times A_{BL}$.

For each value of P, the top edge of the longerons was probed by applying a transverse nodal displacement U_{xp} at $Z = Z_p$, and the probe reaction force was extracted. The two independent control parameters to construct the stability landscape are therefore the pressure and the probe displacement.

All the analyses were performed using the Abaqus implicit solver, in a static mode. The pressure was applied as a load, whereas the probes were modeled as displacement boundary conditions. An automated step size was used for both pressure loading and probing, and no automatic stabilization was used.

The last important consideration is the choice of the probe locations. In a classical buckling and post-buckling analysis, one would compute non-linear buckling eigenmodes and seed a linear combination of these modes into the structure's initial geometry [66]. The use of an arclength solver coupled with the imperfect geometry enables tracing the first bifurcation branch. The early transition into such a branch, governed by the structure's non-linear eigenmodes, was studied first. Therefore, the probing location was first chosen as the location at which the peak deformation for

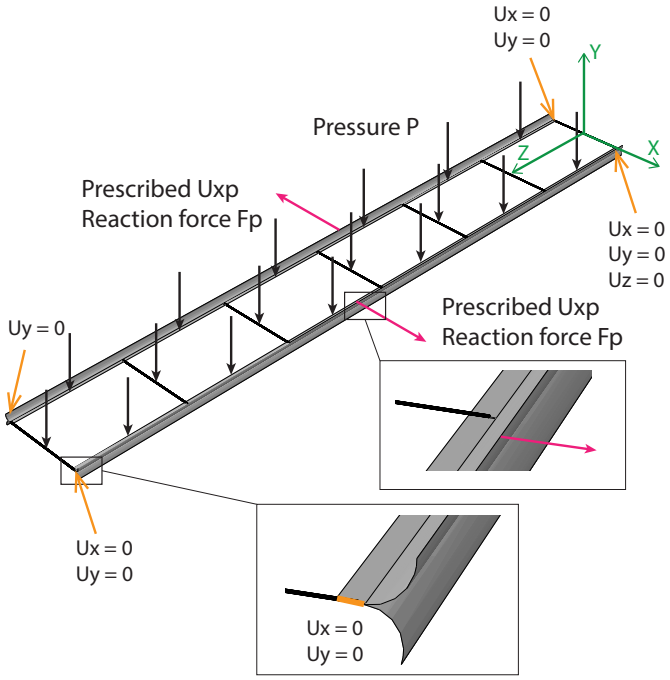

Figure 5.4: Schematic of FEM for strip loaded by pressure.

the first eigenmodes is reached.

The first non-linear eigenmodes were obtained using the following iterative scheme. First, a buckling mode prediction was performed for the undeformed structure to obtain the linear buckling load P_{cr-lin}. Next, a pressure of $0.5P_{cr-lin}$ was applied on the strip. A buckling prediction was then performed on the prestressed strip and a new value of the critical buckling load was then computed. This process was repeated until the pressure applied before the buckling prediction step had converged, thus obtaining the non-linear buckling pressure. This procedure led to the four closely spaced eigenmodes shown in Figure 5.5a, which consist of single dimples localized on both sides of the central batten. The highly localized nature of these eigenmodes could be explained by the pressure loading causing a non-uniform bending moment along the strip length, which reaches a maximum magnitude at the center of the structure. In order to study early post-buckling branches associated with such modes, the probe location was chosen as the location of maximum displacement for these modes.

Two probing schemes were considered in the present study, as shown in Figure 5.5b. The antisymmetric probing scheme uses one probe per longeron. The location of this probe matches the peak displacement of the first buckling mode for each longeron. The symmetric probing scheme uses two probes on each longeron, and

the probe displacements are all equal. The probe locations are given by the location of peak displacement for the first two buckling modes. In both probing schemes, the probes are displaced in the x-direction, in an outward sense. Note that the computed modes are combinations of inward and outward flange deflections. By conducting a conventional numerical post-buckling analysis based on a linear combination of these modes seeded in the perfect geometry, it was observed that the deformed shape obtained from the first bifurcation branch featured only outward buckles. This motivated the choice of the outward probing scheme, but it should be noted that restricting the chosen probing scheme to these modes, has the effect of restricting the scope of the meta-stability study. There is no guarantee that this approach yields the lowest transition into buckling, and a more complete set of probing schemes would be needed to have a full picture of the complex buckling behavior of such a structure. A more general approach, that does not use the eigenmodes to choose the probing location, is presented in Section 5.7.

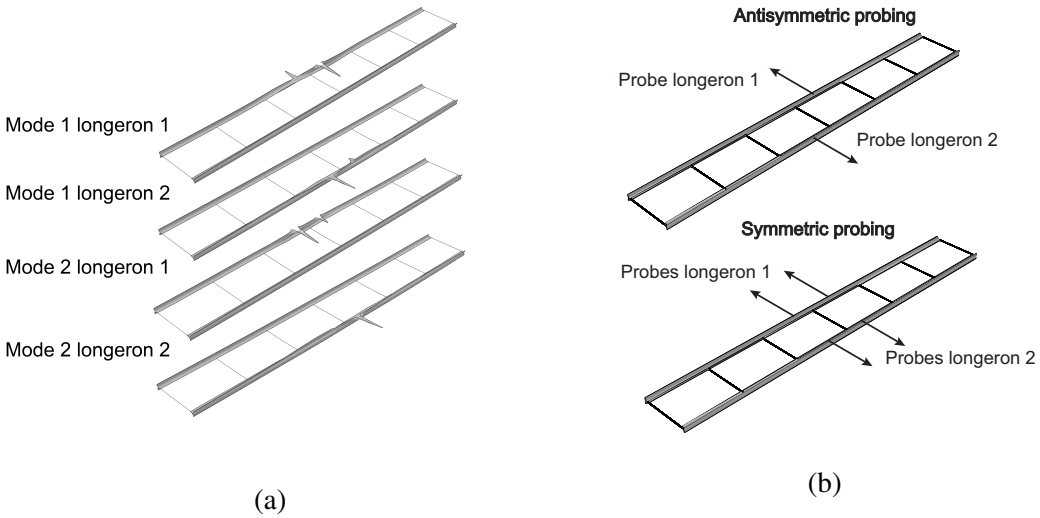

(a) (b)

Figure 5.5: (a) First 4 non-linear buckling modes for L = 1.8 m. (b) Symmetric and antisymmetric probing schemes derived from these modes.

Stability landscape

Plotting of the reaction force as a function of the probe displacement for several values of the applied pressure load generates the stability landscape for the strip. This section focuses on a 3 m long strip for which the stability landscape for antisymmetric probing is shown in Figure 5.6, and the landscape for symmetric probing is similar. All the features described in the introduction and Section 5.3 can be seen here. The obtained minimum post-buckling load for this specific strip

length is $P_M = 0.86$ Pa. The ridge, fundamental path, and unstable equilibrium contour intersect at the non-linear buckling load $P_{cr} = 1.45$ Pa.

It is interesting to note that the values of critical probe displacement obtained in the present study are similar to the values obtained for industrial cylindrical cans [81]. However, in the present study the open cross-section of the longerons lowers the ridge probe force magnitude about two orders of magnitude beneath the cylindrical cans [81], where ridge forces of about 1 N were found just above the minimum post-buckling load.

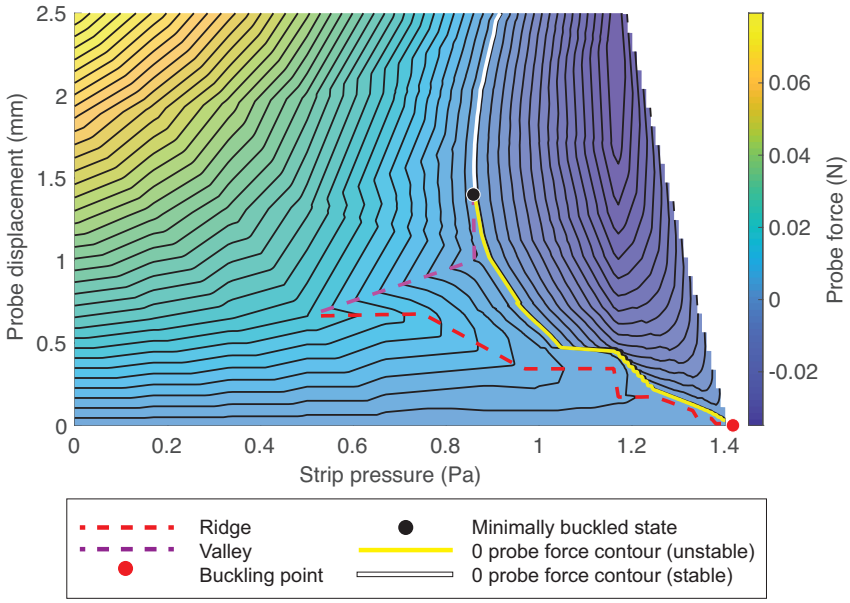

Figure 5.6: Stability landscape for 3 m long strip structure, for antisymmetric probing.

Probing instabilities

The previous subsection has presented the stability landscape for antisymmetric probing of a strip with $L = 3$ m. In the nominal probing scheme, the structure remains straight and planar and the two probe forces are equal, such that there is no net force resultant on the structure (although there is a moment resultant for the antisymmetric probing scheme).

Bifurcations were encountered on the main probing path, in the immediate vicinity of the unstable equilibrium point (first appearance of 0 probe force). They are reported in Figure 5.7 with their corresponding mode shapes, for an applied pressure $P = 1.17$ Pa. Two types of instabilities can be seen. The first one is linked to the first and

second eigenvalues, and involves an interaction between local flange instabilities at the probe location, and in-plane bending of the entire structure. This type of interaction arises from the low in-plane bending of the strip structure. The second type of instability is purely local and is triggered by the third and fourth eigenvalues. In the case of the first and third eigenmode, a local symmetry breaking bifurcation occurs locally, as the single wave dimple at the probe location transforms into an antisymmetric mode shape. This type of bifurcation has been observed before in other structures, such as an elastic arch under normal concentrated force. A classification of bifurcations and obstacles to a probing sequence has been provided by Thompson, Hutchinson, and Sieber [77].

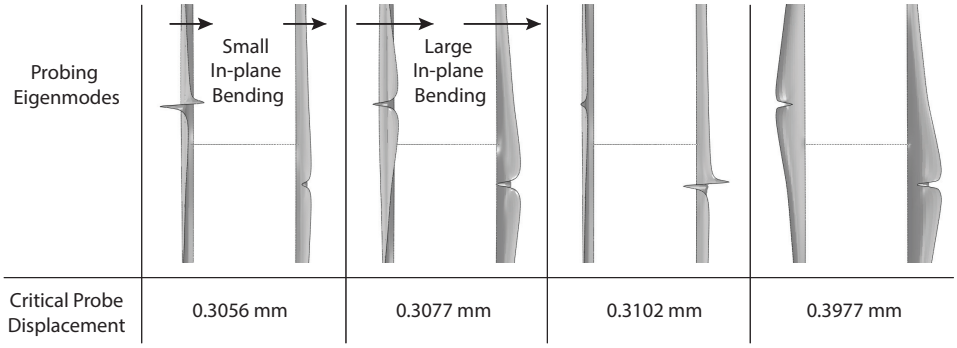

Figure 5.7: Eigenvalues encountered during a probing sequence at P = 1.17 Pa.

The cluster of eigenvalues near an unstable equilibrium solution gives rise to multiple probing paths. Two of these paths are highlighted in Figure 5.8a. The deformed shapes following the dashed path are shown in Figure 5.8b, for 4 different probe displacements. One can observe that the behaviors of longeron 1 and 2 are identical until bifurcations are reached. In this initial probing regime, the buckle amplitude of both longerons grows, and the probe force increases and then decreases towards the unstable equilibrium solution. Past the bifurcation, the behavior of longerons 1 and 2 are different. The structure starts bending in plane, as previously described, which results in an increase in the buckle amplitude for longeron 1 while longeron 2 deforms globally in bending. The paths shown by solid lines in the figure are essentially delayed version of the dashed paths, for which bifurcations occur in the range of negative probe forces. Once the bifurcation has been passed, the deformed shapes obtained for the solid-line paths are similar to the ones for the dashed paths. These two sets of paths illustrate the local/global interaction that can disturb a probing sequence, but many other paths exist.

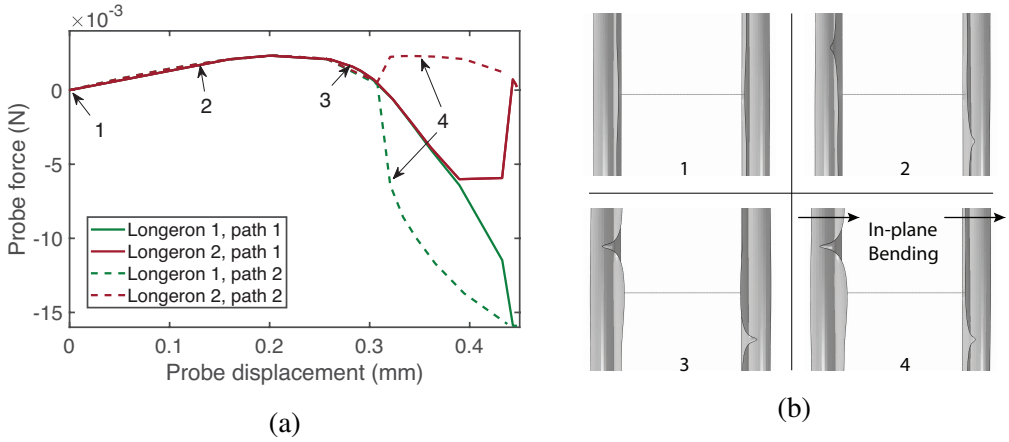

(a) (b)

Figure 5.8: (a) Two sets of probing paths for longeron 1 and 2 after encountering a bifurcations, for $P = 1.17$ Pa. (b) Deformed shapes at various points of the probing paths shown in (a).

These instabilities can be seen as limitations to the probing analysis, but in fact they highlight a powerful approach to selecting appropriate sets of constraints and boundary conditions for a given structure. In other words, these instabilities can be avoided by the judicious implementation of additional boundary conditions.

5.5 Generalization of stability landscape to post-buckling regime

Iterative construction of stability landscapes

The focus of this section is the ultimate pressure that can be carried by the strip structure which requires a study of the post-buckling response of the structure using stability landscapes. Knowledge of the structure's post-buckling behavior is the key to understanding whether buckling is benign or catastrophic.

Consider the stability landscape shown in Figure 5.3. The unstable equilibrium solutions, defined by the yellow contour, determine the critical probe displacements needed to reach the yellow contour. Past this critical displacement, the probe can be released and the structure will naturally snap into the stable equilibrium solutions, defined by the white contour. Once the stable equilibrium contour has been reached, the structure has transitioned into its post-buckling path.

This transition can be implemented easily in the finite element analysis. Note that it differs from the classical approach, which consists in seeding imperfections in the structure's undeformed geometry, and using an arc-length solver to force the bifurcation into a specific branch. While the classical methodology is useful to obtain a rough idea of the structure's post-buckling behavior, it can be quite difficult

to implement, as shown in Section 5.2, because one does not have control over when the imperfect structure will bifurcate, and the post-buckling path is approximate since the structure's geometry has been changed. For imperfection sensitive structures (which include thin shell structures), these two effects are particularly pronounced, and it becomes difficult to resolve higher-order bifurcation paths (i.e., bifurcations from the primary post-buckling branch) since the imperfections needed to resolve the higher-order bifurcations can modify the structure's behavior for earlier bifurcations. Path-following methods [25] are extremely powerful in this respect, as they allow the exact post-buckling path for a structure to be traced. However these methods are available only in research finite element codes. An advantage of using the probing method adopted here is that it gives insights into the stability of the fundamental and post-buckling paths and their resilience to disturbances, while allowing resolution of the strip behavior after multiple bifurcations, and thus up to the ultimate failure pressure. It can also be implemented in experiments, which is of course a major advantage.

Once the structure starts following its first post-buckling path, its behavior can be be computed uniquely until a new bifurcation is encountered. At this point, a non-linear eigenvalue computation can be performed, and the probing process can be repeated using the maximum amplitude location of these new eigenmodes to determine the new probing location. Note that once the $n-1$ buckle is fully formed, there is no more need to continue probing at its location, and the $n-1$ probe can be released when the n probe is activated. This iterative process is repeated until the maximum pressure is found.

This process is illustrated in Figure 5.9, corresponding to the antisymmetric probing of Figure 5.11a. A specific post-buckling path is shown but there exist infinite possible paths. Each path is associated with a specific level of disturbance and the associated energy barriers are reported in Figure 5.9b. However, while the pressure at which probing is started sets the point at which the transition into buckling occurs, it does not affect the behavior of the structure after it reaches the stable equilibrium path. Therefore, for a specific probing scheme, the maximum pressure will be independent of the path chosen. Also, once a buckle is fully formed and the probe is released, the peak displacement of the buckle can still be tracked.

The peak displacements of the three buckles are shown by black curves in Figure 5.9a, and the deformed shapes at points I, II, and III are shown in Figure 5.10. Note that buckle 1 yields the largest deformation. Also note that global failure of

the strip occurs when buckle 1 reaches a maximum value of outward displacement, at P_{max}. At this point, a localized fold forms at the center of the structure while the amplitudes of buckle 2 and 3 decrease, and the strip starts folding.

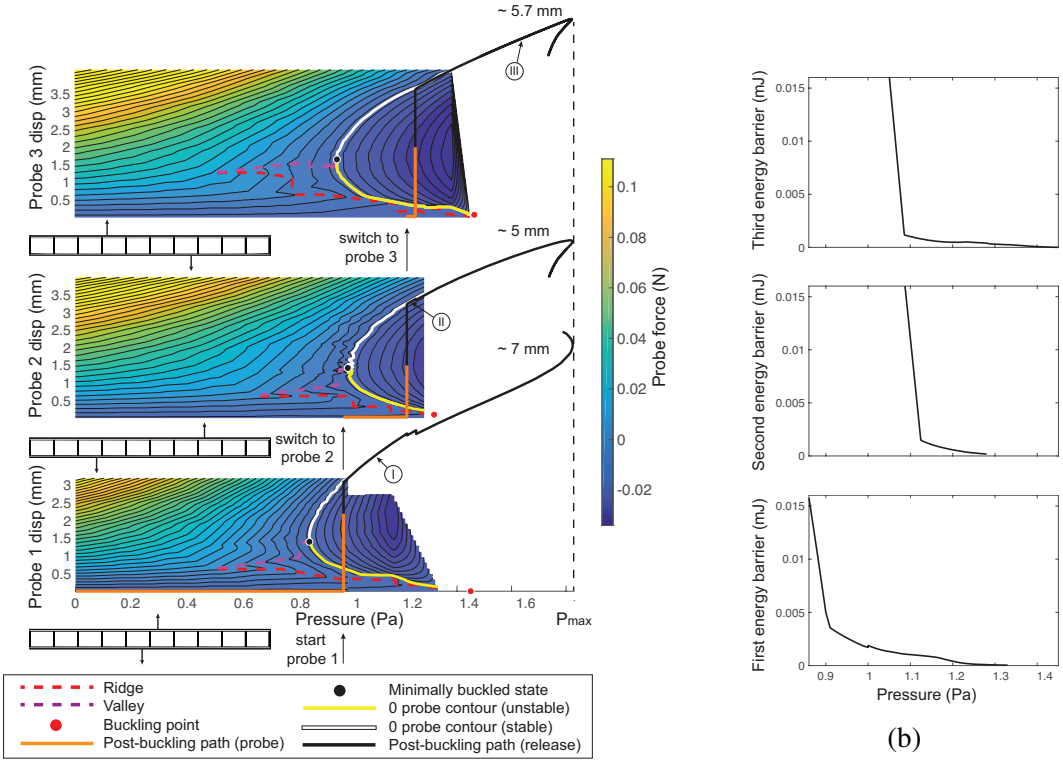

(a) (b)

Figure 5.9: (a) Stability landscapes obtained for the first, second and third sets of probing. The labels I, II, and III refer to particular points at which the deformed shape of the structure is shown in Figure 5.10. (b) Energy barriers between pre-buckled and post-buckled states for each of the 3 buckling transitions.

Post-buckling response for symmetric and anti-symmetric probing

The method described in the previous subsection was used to trace the structure's post-buckling response for symmetric and anti-symmetric probing. The antisymmetric probing starts as shown in Figure 5.5b. The subsequent probes 2 and 3 are determined using the iterative method described earlier, by considering only the first eigenmode for each longeron. Similarly, the symmetric probing starts as shown in Figure 5.5b and uses the first two eigenmodes to choose the probe locations, which results in using 4 probes at a time. These two probing schemes are shown in Figure 5.11a.

The probing approach allows one to trace the full post-buckling response shown in

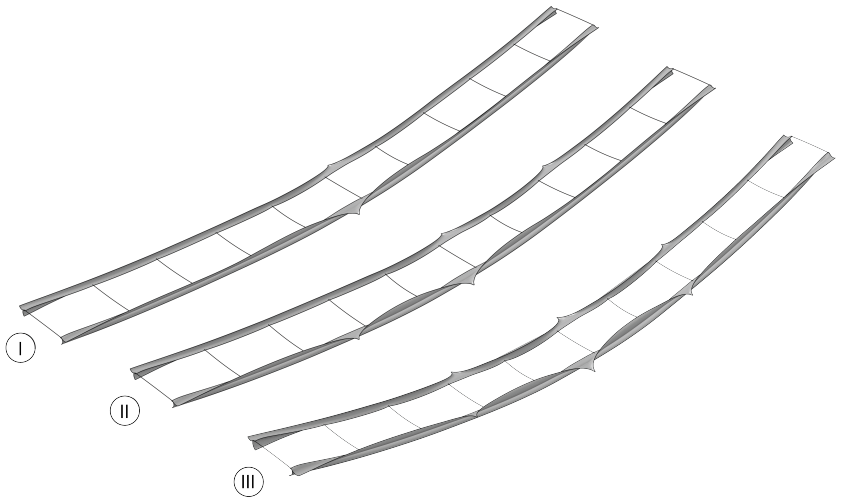

Figure 5.10: Deformed shapes corresponding to points I, II, and III of Figure 5.9a.

Figure 5.11b. The x-axis corresponds to the displacement extracted in the middle of the longeron (1.5 m from the end), at the cross-section centroid. The previously described failure of the structure appears as a horizontal tangent in this plot, which highlights the loss of stiffness at the maximum value of pressure. The deformed shapes, just before failure and for both types of probing, are shown in Figure 5.12. Note that the antisymmetric probing scheme yields a softer post-buckling regime and a lower value of the maximum pressure. Thus, the antisymmetric probing scheme is the one to be considered when determining safe bounds on the structure's operational range.

In addition to the probing method, an attempt was made to compute the full antisymmetric post-buckling response using the "traditional" method, which consists in seeding the buckling mode shapes into the initial geometry. The result is shown by a black dashed line in Figure 5.11b, for a total imperfection amplitude of 2% of the shell thickness. The probing and "traditional" techniques give essentially the same result for the first post-buckling branch. However, this simulation was not successful in going past the first post-buckling regime. Due to the structure's high imperfection sensitivity, seeding the second buckling modes in the initial geometry (even for an imperfection amplitude of less than 0.5% of the shell thickness) degrades the pre-buckling response and first bifurcation can no longer be resolved. Finally, the numerical probing technique presented in this chapter allows the structure to transition from its fundamental path directly to the stable post-buckling branch while the applied pressure is kept constant. Such a scheme, while numerically efficient, does

not detect any potential bifurcations arising from the unstable post-buckling branch, as highlighted by Pirrera et al. [63]. Such bifurcations could give rise to different stable post-buckling branches.

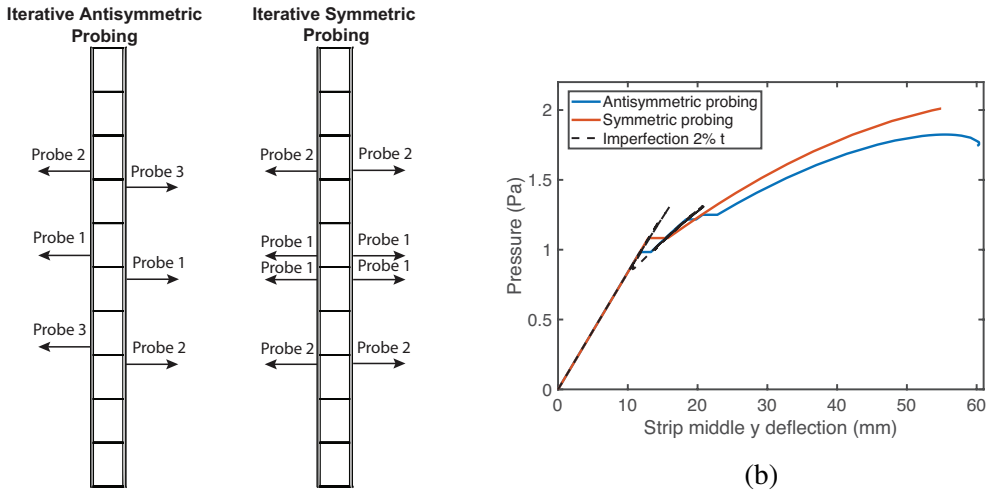

(a) (b)

Figure 5.11: (a) Probing schemes for higher-order stability landscapes. (b) Full post-buckling response for the symmetric and antisymmetric probing scheme.

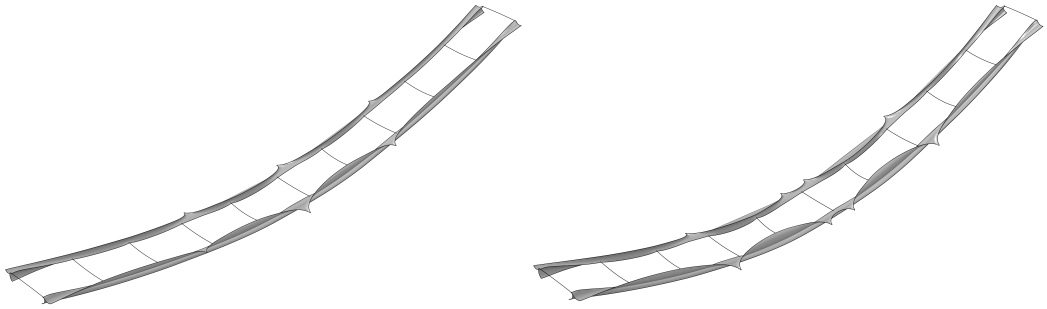

(a) (b)

Figure 5.12: Deformed shape for (a) antisymmetric and (b) symmetric probing.

To overcome this limitation, two approaches are taken. The first one consists in checking the eigenvalues of the tangent stiffness matrix, as the structure is probed. Any intersection with a new stable post-buckling branch will be detected in this way, and the probing scheme can then be changed following the eigenmodes of this new bifurcation, before reaching the stable equilibrium contour of the previously determined bifurcation branching from the fundamental path. However, this approach is unable to detect unstable paths that do not restabilize since they do not intersect the probing path. The second approach consists in releasing the probe right before

reaching the unstable equilibrium contour. The full unstable and stable branch can then be resolved using an arclength solver, and one can directly check for negative eigenvalues on the unstable post-buckling branch. This second technique has been used successfully for different types of structure. For the ladder-type coilable structure, no negative eigenvalues were detected while probing, and the preliminary experiment discussed in Section 5.2 suggests that there are no fully unstable paths leading to early failure before the ultimate pressure is reached.

5.6 Effects of strip length on buckling energy barrier and characteristic loads

The analysis described in Section 5.4.2 was repeated for lengths of 1.8 m, 4.2 m, 5.4 m, and 6.6 m. The first quantity that has a direct impact on the early buckling of the structure is the minimum post-buckling pressure which was computed it for all of the considered strip lengths. The evolution of the linear and non-linear buckling pressures was also tracked. Finally, by computing the full post-buckling response of the structure, the maximum post-buckling load was determined.

The evolution of these four quantities as a function of L is shown in Figure 5.13a. This figure shows that the linear and non-linear buckling pressures decrease as the strip length increases, with the linear buckling pressure (eigenvalue problem for the undeformed structure) slowly converging to the non-linear buckling pressure and the eigenmodes also become very similar. While the first non-linear eigenmodes localize on a side of the central batten, the linear eigenmodes are symmetric with respect to the central batten. As the length of the strip increases, the non-linear buckling modes become less localized and more symmetric with respect to the central batten, as shown in Figure 5.14.

By comparing the non-linear eigenmodes in Figure 5.14 with the post-buckling deformed shapes in Figure 5.10, it can be noted that the non-linear eigenmode has multiple peaks of decreasing amplitude, whereas the deformed shape I in Figure 5.10 features only a single buckle. This type of localization has been studied for various problems, including elastic beams on an elastic foundation [83] and spherical shells [4].

A second observation is that the ultimate buckling pressure decreases as L increases. When looking at the formation of local buckles in the post-buckling regime, it is observed that the longer the strip, the more buckles are formed before reaching the ultimate buckling load. Since the formation of a buckle in the structure is associated with a decrease in stiffness, the structure will reach a zero value of stiffness earlier

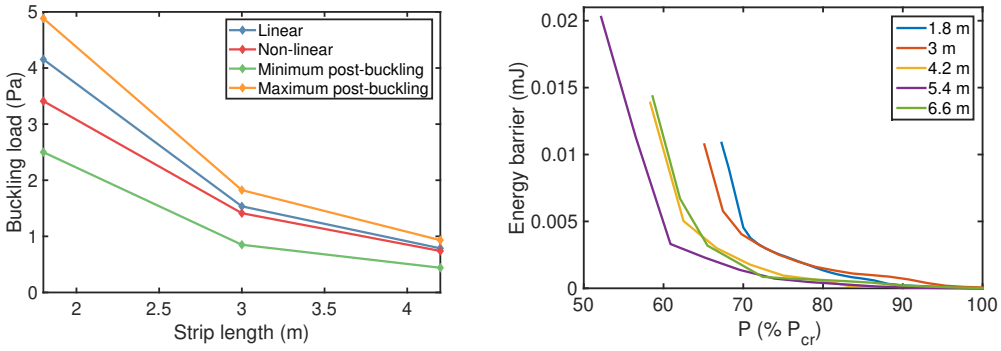

Figure 5.13: Evolution of (a) critical loads and (b) energy barrier as a function of L.

if more buckles can form, since the minimum buckling pressure for higher-order buckles does not increase significantly (see Section 5.5.2). The ultimate buckling load is about 1.39% greater than the non-linear buckling load for $L = 1.8$ m and only 1.26% greater for $L = 4.2$ m.

As L increases, a similar decrease in the minimum post-buckling pressure is observed. Notice that the ultimate buckling load converges faster to the non-linear buckling load than the minimum post-buckling pressure.

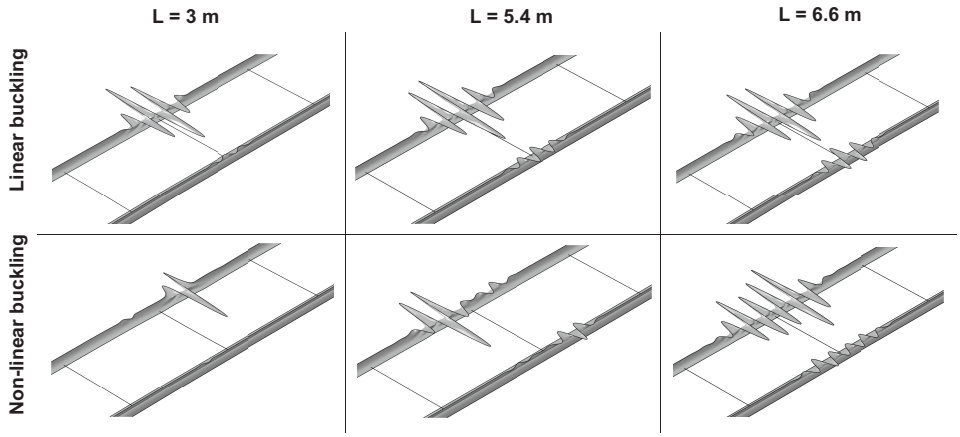

Figure 5.14: Comparison between linear and non-linear buckling mode shapes for 3 different lengths.

The energy barrier against the buckling transition into the antisymmetric first mode at $P < P_{cr}$ has been plotted in Figure 5.13b for the various strip lengths considered. The shape of the barrier is consistent across the different lengths and follows qualitatively the same trend as the minimum post-buckling pressure. A rather surprising effect is that, whereas the minimum post-buckling pressure and energy barrier decrease

when L is increased up to $L = 5.4$ mm, the opposite trend is observed when L is increased further to 6.6 m. This result indicates that the minimum post-buckling pressure and the energy barrier are not monotonic with respect to the strip length.

The results obtained in this section can be linked to the spacecraft design application described in the introduction. In Figure 5.15, the linear buckling pressure for a range of strip lengths and widths has been compared to the value of 9×10^{-6} Pa, which corresponds to the solar radiation pressure on a spacecraft orbiting the earth (denoted as 1 astronomical unit, or 1 au). For narrow strips ($W < 0.6$ m), buckling takes the form of a localized longeron buckling, as previously described. In wider strips ($W > 0.6$ m) the battens are longer and tend to buckle before the longerons, which gives rise to a plateau in the linear buckling pressure for shorter strips. The evolution of the linear buckling pressure for longer strips is consistent over the range of strip lengths. For $W = 1$ m and $L = 12$ m, the linear buckling pressure is 2215 times greater than the solar pressure, for $L = 30$ m it is 434 times greater, and for $L = 60$ m it is 333 times greater. These results indicate that the risk of buckling under solar pressure is very small for all lengths considered. However, for these longer strips, the linear buckling mode takes the form of a global strip twisting along its axis and the non-linear localization effects may possibly yield significantly lower non-linear buckling loads.

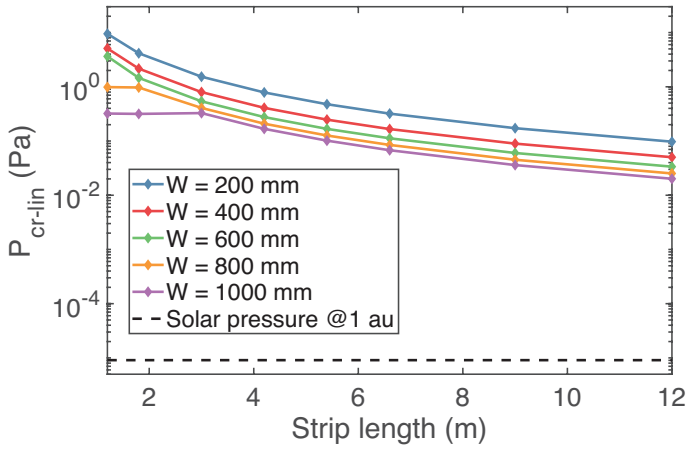

Figure 5.15: Linear buckling pressure as a function of strip length and strip width.

5.7 Low-energy escape paths

The previous part of this study has analyzed early transitions into post-buckling, corresponding to the first non-linear buckling modes. However, while these modes give rise to a meta-stable fundamental path above the minimum post-buckling pres-

sure, there may exist additional meta-stable paths in the immediate vicinity of the fundamental path that are also associated with a very low energy barrier, and which would yield an earlier transition into the post-buckling regime. Such *broken-away* paths were recently studied for the case of the cylindrical shell under axial compression and for the spherical shell under pressure [38, 40, 78]. In the case of the cylinder, the corresponding mode shapes take the form of a localized dimple.

Broken-away paths run close to the fundamental path without ever intersecting it, and therefore cannot be predicted by a bifurcation analysis [37]. The points forming such paths are referred to as *mountain pass points*, because they correspond to the top of a ridge in the total potential energy map. This ridge separates the fundamental well from a lower potential well corresponding to a localized buckling mode, and the mountain pass points correspond to an unstable equilibrium contour in the probe force stability landscape. The mountain pass point requiring the least amount of energy to be reached is called the lowest mountain pass point, and for the cylinder it has been shown that the single dimple solution is indeed the lowest mountain pass point [32].

In order to search for broken away paths and mountain pass points for the strip structure, the finite element analysis described in Section 5.2.2 was extended to multiple probe locations. For $L = 3$ m, 39 different probe locations (one probe location every 75 mm) were defined along the top edge of each longeron, with the Z-coordinate defining their position. Both longerons were probed in the same outward anti-symmetric fashion described in Section 5.4.2, but the probe location Z was increased for each new analysis. The probe force for each probe location and for different values of the applied pressure was obtained from the analysis, and the energy barrier was computed as described in Section 5.3. Figure 5.16a is a plot of the energy barrier as a function of the probe location Z and the applied pressure.

Focusing first on pressures close to the non-linear buckling pressure ($P = 1.1 - 1.3$ Pa), three plots of the energy barriers for varying Z are shown in Figure 5.16b. The local minima occur for $Z = 1,423, \quad 1,579$ mm, corresponding to the first buckling modes. For $P = 1.33$ Pa, there exist two more local minima further away from the center of the strip, at $Z = 1,120$ and $1,880$ mm. These local minima are relatively high compared to the buckling mode minima for $P = 1.167$ Pa, but they quickly drop to comparable values for $P = 1.33$ Pa. This result indicates that buckling could occur also at these locations for a small disturbance, instead of the main disturbances near the center of the strip. However, note that for this range of

pressures, the disturbances corresponding to the buckling modes still correspond the lowest energy barrier.

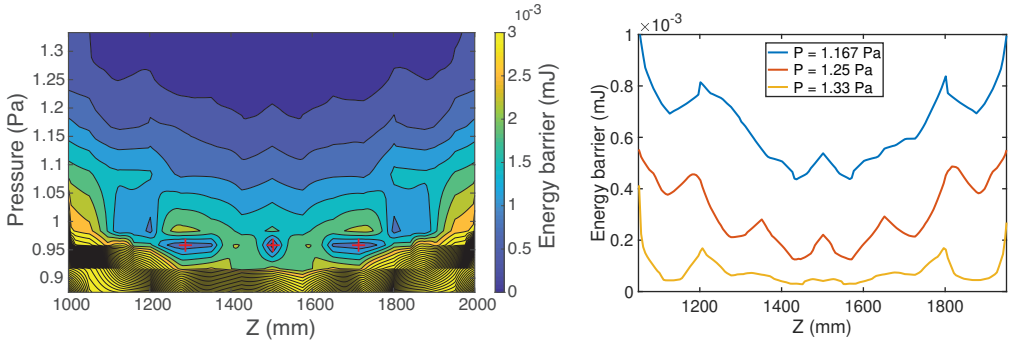

(a) (b)

Figure 5.16: (a) Contours of energy barrier for varying z location of probe and pressure. (b) Detail of 3 high-pressure energy barriers.

The situation changes if lower values of the pressure are considered, in Figure 5.16a. For $P = 0.96$ Pa, there is a global minimum for the energy barrier at the center of the strip ($Z = 1,500$ mm) surrounded by two local minima at $Z = 1,282$ mm and $Z = 1,722$ mm. The global minimum changes location rapidly, and for $P = 0.98$ Pa the global minima are at locations $Z = 1,202$ mm and $Z = 1,802$ mm, marked with a + in the figure. Note that the pressure at which these local minima occur is above the minimum post-buckling pressure for the strip structure.

The present analysis has shown that buckled equilibrium solutions exist for probing at these alternative locations, which cannot be determined by solving the classical buckling eigenvalue problem. An important observation is that the location of the lowest mountain pass points for the strip structure depends on the value of the pressure. Finally, although only antisymmetric probing was considered here, similar results can be expected if only one longeron is probed locally.

5.8 Effect of initial imperfections on strip stability landscape

It is well known that thin shells are highly sensitive to geometric imperfections, and a natural question regards the sensitivity of the stability landscape to imperfections in the undeformed geometry. A preliminary investigation was carried out for the case $L = 1.8$ m, with imperfections based on the first eigenmode for longerons 1 and 2, as shown in Figure 5.5a.

The imperfect structure was probed using the outward antisymmetric probing scheme at the location of the peak buckling mode displacement. In this specific case,

the probing location also corresponds to the location of the maximum imperfection amplitude. The stability landscapes obtained for this specific probing scheme and for imperfection amplitudes ranging from 0% t to 50% t are shown in Figure 5.17a. This figure shows that the imperfection has a significant impact on the structure's buckling load, which corresponds to the pressure above which the stability landscape can no longer be computed (the solver encounters the first bifurcation). For the perfect geometry, the buckling pressure is $P_{cr} = 3.3$ Pa which decreases to 2.9 Pa (88% of P_{cr}) for an imperfection amplitude of 10% t, 2.48 Pa (75% of P_{cr}) for an imperfection amplitude of 30% t, and finally reaches 2.08 Pa (63% of P_{cr}) for an imperfection amplitude of 50% t.

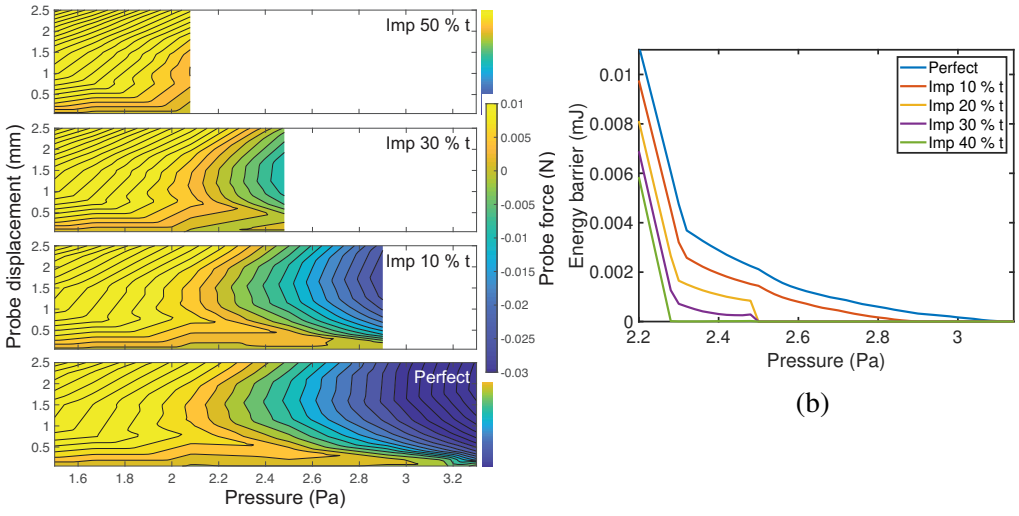

(a) (b)

Figure 5.17: (a) Evolution of the 1.8 m strip stability landscape for antisymmetric probing with growing geometrical imperfections. (b) Evolution of the first buckling energy barrier for the 1.8 m strip with growing geometrical imperfections.

An important observation is that the minimum post-buckling pressure is barely affected by the imperfection for amplitudes under 40% t. For the perfect geometry, the minimum post-buckling pressure is $P_M = 2.26$ Pa. This value does not change for an imperfection of 10% t and decreases only slightly, to 2.22 Pa and 2.2 Pa for imperfection amplitudes of 30% t and 40% t, respectively. For a critical value of imperfection amplitude, between 40% t and 50% t, the buckling load equals the minimum post-buckling pressure, and past this value of imperfection, the structure

is no longer meta-stable.

A final observation is that the energy barrier required to reach early buckling for the imperfect structure, shown in Figure 5.17b, decreases when the imperfection amplitude increases, and there is a sudden drop for imperfection amplitudes above 10% t.

5.9 Conclusion

This chapter has presented a numerical study of the buckling and post-buckling behavior of structures of interest for large coilable solar arrays. The specific structure that has been studied is a ladder-type strip structure consisting of two coilable thin-shell longerons connected by transverse battens. Its transition into buckled configurations has been captured by plotting its stability landscape. This landscape is a three-dimensional plot of three independent quantities, the force and displacement of a localized lateral disturbance, introduced on the strip using a probe, and the main loading parameter. In the present case, the stability landscape of a strip structure is a plot of probe force vs. probe displacement and vs. transverse pressure.

It has been shown that the stability landscape for a pressure-loaded strip is similar to the landscape for classical shells, such as the axially-loaded cylinder and the pressure-loaded sphere. Similarly to classical shells, the stability landscape for the strip shows that an early transition of the strip into buckling can be triggered by small disturbances, whose amplitude decreases when the main loading is increased. Key differences between the strip structure and the classical thin shells have been highlighted. Specifically, while the classical shell structures buckle catastrophically, the strip structure features a large stable post-buckling range. Therefore, the maximum post-buckling load that can be sustained by strip structures is significantly higher than the first buckling load.

The same probing technique used to derive the stability landscape for the strip to form its first buckle has also provided an effective way to both investigate its post-buckling response and to gain insight into the meta-stability of the post-buckling path. This approach is especially useful when multiple successive buckles are encountered, as the level of disturbance needed to form a specific series of buckles can be determined.

The probing of the structure's longerons was applied at multiple locations, and this analysis showed the existence of broken-away paths (mountain pass points) corresponding to the single dimple in the cylinder and the sphere. The mode shapes

for these specific early buckling paths localize at different locations than the ones predicted by a classical eigenvalue problem. An important take-away from this problem is that the location of the lowest mountain pass point (minimum energy barrier to transition into buckling) is a function of the pressure applied to the strip.

The effect of imperfections, based on the first buckling mode, on the strip stability landscape has been assessed. While imperfections significantly degrade the buckling load and also erode the energy barrier separating pre-buckled from post-bucked states, it has been found that they have little impact on the minimum post-buckling pressure. It was also found that for a sufficiently large imperfection amplitude, the buckling load becomes as low as the minimum post-buckling pressure, and the structure loses its meta-stability.

Regarding the practical design of strip structures, the present extension of the probing approach to more complex thin-shell structures enables different design strategies. For applications in which buckling is to be altogether avoided, the structure can be designed such that it never exceeds the minimum post-buckling pressure. If upper bounds on the disturbance amplitude during operation and manufacturing deviations are known, the structure could be operated above its minimum post-buckling pressure by using the energy barrier of the worst imperfect structure as the main design limit. Finally, in the case of a stable post-buckling regime and if small buckles during operation are acceptable, the ultimate failure load can be derived efficiently, numerically or experimentally, using the probing technique and can be used as a design criterion.

Last, for the specific strip structures that are of current interest [18], it has been shown that 0.2 m wide strips with lengths ranging from 1.5 m to 4.2 m have critical pressures from 5 Pa to 1 Pa, respectively. Under these loads, the structures will elastically collapse by folding around the center. The corresponding minimum post-buckling pressures range from 2.5 Pa to 0.5 Pa. For spacecraft applications it should be noted that these values are several orders of magnitude larger than solar pressure loading. For longer strips, knowledge of the strip stability landscape will be a crucial tool, and the methods presented in this chapter will play a key role in enabling the design of such structures.

Chapter 6

CONCLUSION

6.1 Summary and contributions

The work presented in this thesis has made several contributions to the field of shell buckling and in particular, its application to spacecraft structures. The overarching goal was to extend the newly developed probing methodology to more complex thin-shell structures. This methodology was first used in 2016 to characterize the meta-stable behavior of cylindrical and hemispherical shells close to buckling. Even if these experimental studies showed that in theory, the methodology could be used to derive less conservative buckling criteria, their scope was restricted to canonical problems and suffered some limitations. In fact, probing was only ever applied to the two problems mentioned above, and was only used experimentally a handful of times. The present work extended probing to real engineering structures and loading, and demonstrated that it can be used in practice as part of the structure's design process. It paves the way to the development of more efficient concepts, in which structures are used closer to their buckling load than ever before, and even in their post-buckling regime. It would allow for lighter structures to be built and has the potential to enable new applications, such as extremely large aperture space solar power satellites. In order to fulfill the main research goal, the work has been divided into four parts, and contributions of each of these steps are highlighted next.

In a first research effort, simulations have been conducted to explore the use of probing for an open section thin shell structure under bending. This specific structure and loading depart significantly from the two canonical problems studied before. For cylindrical and spherical shells, it has been shown that imperfection sensitivity and localization play a crucial role in the shell's buckling behavior. In addition, close to the buckling load, the shell's behavior can be characterized by a so-called stability landscape of shell buckling, which represents the probe force as a function of the probe displacement and the main loading. In the present research, we showed that for the more complex open-section structure and bending loading, imperfection sensitivity and localization are also dominant, and that buckling follows the same stability landscape of shell buckling. Even if previously, probing was restricted to the study of a single buckle, the framework was extended to probe the entire

structure, and new unstable probing scenarios revealed buckling phenomena specific to assembly of thin shells and open sections, never observed before. This initial work proved that probing can be used to navigate the complex multiplicity of post-buckling solutions know as spatial chaos, for real engineering structures. It also served as the basis for the experimental work of this thesis.

Motivated by the previous computational study, our next research work focused on developing a new experimental setup to conduct probing on a real open-section thin-shell structure under bending. This experiment required an important apparatus, capable of applying bending to the test sample. Initial bending experiments were conducted on classical bending machines commonly used to test engineering structures. However, these machines have proven to be inadequate for the problem at hand since they introduce prestress during testing and therefore worsen the structure's imperfection sensitivity. Even an undetectable misalignment (on the order of one arc-minute) between the test structure's ends had a significant impact on its buckling behavior, and masked the phenomena observed in simulation. To address this major challenge, we designed and implemented a new bending machine suitable for testing extremely imperfection-sensitive structures. It uses a combination of pressurized air bearings and counterweights to provide statically determinate boundary conditions to the structure. Its isostatic nature guarantees that no prestress can develop during the test, and therefore that the experimental setup does not introduce any parasitic effects which would influence the buckling behavior. The new machine's performance has been validated with experiments on linear and highly nonlinear structures. This type of bending apparatus has never been realized before, and it is the only machine found in literature that is capable of applying a strict pure bending moment in a general structure.

Next, probing experiments were conducted on the open-section thin-shell structure, and were made possible by the new bending machine. A probing apparatus was designed and added to the experimental setup. The experiment revealed an extremely rich buckling behavior. Experimental stability landscapes have been obtained and showed that multiple buckled equilibria are competing. The landscapes also revealed interactions between local buckles and gave insights into their sequential formation (snaking), which was never experimentally studied before. A new representation of the structure's pre-buckling meta-stability has been developed, and displayed transitions between buckled states as a function of the bending rotation and the energy required by a perturbation to trigger buckling. Probing was then extended to

the whole structure and used to search for alternate buckling modes, disconnected from the structure's unbuckled state. It revealed experimentally for the first time that such modes exist. They can appear in a real environment where disturbances are present and have a significant impact on the structure's post-buckling response.

Finally, we focused on real composite space structures used in the Space Solar Power Project at Caltech. On orbit, these structures are loaded by solar pressure and inertial forces. Probing simulations were presented for the analysis of these particular open-section thin-shell structures, and extended the methodology to non-uniform bending moments. It has been shown that these structures feature a long stable post-buckling regime, which can be used during operations. The use of probing stability landscapes appeared to be powerful to numerically identify the multiple post-buckling paths the structure can follow. These solutions were only possible to determine using complex path-following algorithms before, but could easily be found here using probing in a commercially available finite element software. The methodology was also used to study the stability landscape variations with length and geometric imperfections, and showed that efficient buckling criteria can be found for such structures.

6.2 Probing for the design of more efficient structures

The following subsection aims to give a broader perspective on the use of probing for the design of lightweight structures. The ultimate goal is to use this technique to increase the operational range of structures, while guaranteeing their safety. This objective can be divided into two scenarios. In the first scenario, buckling is to be avoided and therefore, probing would be used to determine a tight buckling criterion. This scenario corresponds for instance to structures for which the post-buckling response is fully unstable. In the second scenario, localized buckles are allowed to form in the structure as long as it is still capable of bearing a load. This scenario corresponds to the type of structures analyzed throughout the dissertation, for which the post-buckling path quickly restabilizes, and the maximum load is higher than the first buckling load. In this case, probing would be used to determine the range of possible post-buckling responses and determine a maximum load criterion. The use of probing for these two scenarios is detailed here:

- **Operate structure below buckling:** simulations can be used in the early phase of the design process. By conducting probing in finite element analyses on a perfect structure, a critical buckling mechanism can be identified. The load at which a localized buckle can first be sustained in the structure can

be determined, and used as an efficient buckling criterion. This specific load called minimal buckling load, was shown in Chapter 5 to be insensitive to imperfections, as long as the imperfection amplitude is under a specific threshold (40% of the shell thickness for the ladder-type structure of Chapter 5). Later in the design process, probing can be carried out in experiments on structural prototypes. It is possible to test these prototypes non-destructively by tracking the ridge and the valley of the experimental stability landscape. Ridge-tracking enables the determination of the exact buckling load for the unperturbed structure, while valley-tracking yields the exact minimal buckling load. If an upper bound on the energy brought by potential disturbances during operations is determined, experimental probing can be used to derive a tighter buckling criterion, based on the energy barrier required to trigger buckling.

- **Operate structure up to its maximum load:** probing can be extended to the post-buckling regime through simulations. It enables the determination of all possible post-buckling responses, with or without the presence of disturbances. If multiple buckling events occur, stability landscapes can be used iteratively to trace the full post-buckling responses, and a tight lower bound on the structure's maximum load can be determined. Using the maximum load criterion, instead of a buckling criterion, can dramatically increase the range of operation for the structure. Probing can then be used experimentally to validate prototypes. An experimental disturbance diagram can be created and the various post-buckling responses stemming from competing buckling sequences can be determined. It enables the refinement of the maximum load criterion determined through simulation.

6.3 Future work

The work presented in the thesis can serve as the basis for tackling more complex studies and applications. Here, promising avenues of research are grouped into two categories: advancing the probing methodology and extending its use in engineering structures.

Improvements to the probing methodology can be made. In the experiment presented in chapter 3, probing was used to find the critical locations at which buckling occurs. To do so, the structure's edge in compression was discretized into several probe locations. A more systematic and efficient approach could be developed to carry this search. For instance, one could think about having an initially coarse spacing

between probe locations, which subsequently get refined in specific regions, based on metrics computed during probing. The ridge probe force could for example be used for such a metric. The modified method would then be the experimental analog to mesh refinement, commonly used in simulation.

The current experimental setup only allows the probe to apply a compressive force on the structure. The use of a bilateral probe presents significant advantages and could be used in the future. First, it would allow to capture the negative probe forces in the "lake" of the stability landscape. By integrating them, the kinetic energy released during buckling can be measured, without triggering any snap-through of the structure. This information can then serve as an additional criterion to assess the risk associated to buckling. This is especially important for space structures since they usually feature a very low damping on orbit, and kinetic energy release could significantly affect the dynamic of the entire spacecraft. Second, a bilateral probe would also allow probing in both directions, and the complex buckling scenarios highlighted in chapter 2 can be explored experimentally.

One important output of the probing methodology is the energy barrier required to trigger buckling. While this specific quantity can serve as a lower bound on the energy needed for a general disturbance to cause buckling, the link between the two quantities is not obvious. Additional work would be required to assess the local effect of a global disturbance applied on the structure. Of particular interest is the interaction between quasi-static probing and dynamic disturbances. This can be investigated for instance by focusing on the coupling between vibration and buckling, and the link between the probing energy barrier and the energy contained in a specific vibration mode.

The methodology presented in the thesis can be extended to new applications. Probing experiments can be conducted on the space solar power strip structure, an alternate design can be built based on the probing buckling criteria. One could also use probing as a tool to design imperfection-insensitive structures of arbitrary geometry. Finally, we saw in the experiment that multiple buckled configurations can be triggered by only probing at a single location. If the structure is engineered with precise imperfections, we could envision building thin shell multi-stable structures, in which a local probe actuator would make the structure switch between buckled configurations. Probing would then have a double role. It would be used to construct the stability landscapes needed during the design process, and would also be used as the main actuator during operations.

BIBLIOGRAPHY

[1] A. Abramian et al. “Nondestructive Prediction of the Buckling Load of Imperfect Shells”. In: *Phys. Rev. Lett.* (2020). DOI: 10.1103/PhysRevLett.125.225504.

[2] G. Arnold et al. “A pure bending machine to identify the mechanical behaviour of thin sheets”. In: *6th. International ESAFORM Conference on Material Forming, Salerno, Italy*. 2003.

[3] M. Arya, N. Lee, and S. Pellegrino. “Ultralight Structures for Space Solar Power Satellites, 3rd AIAA Spacecraft Structures Conference”. In: 2016. DOI: 10.2514/6.2016-1950.

[4] B. Audoly and J. W. Hutchinson. “Localization in spherical shell buckling”. In: *Journal of the Mechanics and Physics of Solids* 136 (2020), p. 103720. DOI: https://doi.org/10.1016/j.jmps.2019.103720.

[5] Davide B. *Extremely Deformable Structures*. CISM International Centre for Mechanical Sciences, Springer, 2015.

[6] C. D. Babcock. “The Buckling of Cylindrical Shells with An Initial Imperfection under Axial Compression Loading”. PhD thesis. California Institute of Technology, 1962.

[7] J. Banik et al. “On-orbit validation of the roll-out solar array”. In: *2018 IEEE Aerospace Conference* (2018). DOI: 10.1109/AERO.2018.8396390.

[8] J. A. Banik and T. W. Murphey. “Performance validation of the triangular rollable and collapsible mast”. In: *24th Annual AIAA/USU Conference on Small Satellites, Logan, UT: AIAA/ASU* (2010).

[9] T. Ben Zineb, A. Sedrakian, and J. L. Billoet. “An original pure bending device with large displacements and rotations for static and fatigue tests of composite structures”. In: *Composites Part B: Engineering* 34.5 (2003), pp. 447–458. DOI: https://doi.org/10.1016/S1359-8368(03)00017-9.

[10] M.A. Bessa and S. Pellegrino. “Design of ultra-thin shell structures in the stochastic post-buckling range using Bayesian machine learning and optimization”. In: *International Journal of Solids and Structures* 139-140 (2018), pp. 174–188. ISSN: 0020-7683. DOI: https://doi.org/10.1016/j.ijsolstr.2018.01.035.

[11] S.H.A. Boers, M.G.D. Geers, and V.G. Kouznetsova. “Contactless and frictionless pure bending - principles, equipment and experimental opportunities”. In: *Experimental Mechanics* 50.6 (2010), pp. 683–693. DOI: https://doi.org/10.1007/s11340-009-9257-2.

[12] D. O. Brush and B. O. Almroth. “Buckling of Bars, Plates, and Shells”. In: *McGraw-Hill, New York* (1975).

[13] L. H. Donnell and C. C. Wan. "Effect of imperfections on buckling of thin cylinders and columns under axial compression." In: *Journal of Applied Mechanics* 17.1 (1950), pp. 73–83.

[14] M. Elchalakani, X.L. Zhao, and R.H. Grzebieta. "Concrete-filled circular steel tubes subjected to pure bending". In: *Journal of Constructional Steel Research* 57.11 (2001), pp. 1141–1168. DOI: https://doi.org/10.1016/S0143-974X(01)00035-9.

[15] M. S. Ellison and E. Corona. "Buckling of T-beams under cyclic bending". In: *International Journal of Mechanical Sciences* 40.9 (1998), pp. 835–855. DOI: https://doi.org/10.1016/S0020-7403(97)00126-4.

[16] J. M. Fernandez and T. W. Murphey. "A Simple Test Method for Large Deformation Bending of Thin High Strain Composite Flexures". In: *2018 AIAA Spacecraft Structures Conference*. DOI: 10.2514/6.2018-0942.

[17] E. Gdoutos et al. "Ultralight Deployable Space Structure Prototype". In: *AIAA Scitech 2020 Forum*. 2020. DOI: 10.2514/6.2020-0692.

[18] E. Gdoutos et al. "Ultralight Deployable Space Structure Prototype, AIAA Scitech 2020 Forum". In: 2020. DOI: 10.2514/6.2020-0692.

[19] E. Gdoutos et al. "Ultralight Spacecraft Structure Prototype, AIAA Scitech 2019 Forum". In: 2019. DOI: 10.2514/6.2019-1749.

[20] S. Gerasimidis et al. "On Establishing Buckling Knockdowns for Imperfection-Sensitive Shell Structures". In: *Journal of Applied Mechanics* 85.9 (June 2018). DOI: 10.1115/1.4040455.

[21] S. Gerasimidis et al. "On Establishing Buckling Knockdowns for Imperfection-sensitive Shell Structures". In: *Journal of Applied Mechanics* (2018). DOI: https://doi.org/10.1115/1.4040455.

[22] A. Goel, N. Lee, and S. Pellegrino. "Trajectory design of formation flying constellation for space-based solar power, 2017 IEEE Aerospace Conference". In: 2017, pp. 1–11. DOI: 10.1109/AERO.2017.7943711.

[23] R. M. J. Groh and A. Pirrera. "On the role of localizations in buckling of axially compressed cylinders". In: *Proceedings of the Royal Society A: Mathematical, Physical and Engineering Sciences* 475.2224 (2019), p. 20190006. DOI: 10.1098/rspa.2019.0006.

[24] R. M. J. Groh and A. Pirrera. "Spatial chaos as a governing factor for imperfection sensitivity in shell buckling". In: *Phys. Rev. E* (2019). DOI: 10.1103/PhysRevE.100.032205.

[25] R.M.J. Groh, D. Avitabile, and A. Pirrera. "Generalised path-following for well-behaved nonlinear structures". In: *Computer Methods in Applied Mechanics and Engineering* 331 (2018), pp. 394–426. DOI: https://doi.org/10.1016/j.cma.2017.12.001.

[26] Larry L. H. *Compliant mechanisms*. Wiley, 2001.

[27] A. D. Hasanyan, C. Leclerc, and S. Pellegrino. "Interface Failure Analysis of Triangular Rollable and Collapsible (TRAC) Booms". In: *AIAA Scitech 2020 Forum*. 2020. DOI: 10.2514/6.2020-0694.

[28] T. J. Healey. "Why bifurcation: a study of a reticulated dome". In: *American Society of Civil Engineers, Structures Congress '89, Sessions related to design, analysis and testing. San Francisco, California* (1989).

[29] M. Hilburger. "Developing the Next Generation Shell Buckling Design Factors and Technologies". In: *53rd AIAA/ASME/ASCE/AHS/ASC Structures, Structural Dynamics and Materials Conference.* (2012). DOI: 10.2514/6.2012-1686.

[30] R. G. Hill and E. J. Zapel. *Pure bending test machine*. US patent Nº 3,026,720. 1959.

[31] J. P. M. Hoefnagels, C. A. Buizer, and M. G. D. Geers. "A miniaturized contactless pure-bending device for in-situ SEM failure analysis". In: *Experimental and Applied Mechanics, Volume 6*. Springer New York, 2011, pp. 587–596.

[32] J. Horák, G. J. Lord, and M. A. Peletier. "Cylinder Buckling: The Mountain Pass as an Organizing Center". In: *SIAM Journal on Applied Mathematics* 66.5 (2006), pp. 1793–1824. DOI: 10.1137/050635778.

[33] N. Hu and R. Burgueño. "Buckling-induced smart applications: recent advances and trends". In: *Smart Materials and Structures* 24.6 (2015), p. 063001. DOI: 10.1088/0964-1726/24/6/063001.

[34] G. W. Hunt and E. L. Neto. "Maxwell Critical Loads for Axially Loaded Cylindrical Shells". In: *Journal of Applied Mechanics* (1993). DOI: 10.1115/1.2900861.

[35] G.W. Hunt, G.J. Lord, and A.R. Champneys. "Homoclinic and heteroclinic orbits underlying the post-buckling of axially-compressed cylindrical shells". In: *Computer Methods in Applied Mechanics and Engineering* 170.3 (1999), pp. 239–251. ISSN: 0045-7825. DOI: https://doi.org/10.1016/S0045-7825(98)00197-2.

[36] G.W. Hunt and E.Lucena Neto. "Localized buckling in long axially-loaded cylindrical shells". In: *Journal of the Mechanics and Physics of Solids* 39.7 (1991), pp. 881–894. DOI: https://doi.org/10.1016/0022-5096(91)90010-L.

[37] G.W. Hunt et al. "Cellular buckling in long structures". In: *Nonlinear Dynamics* (2000). DOI: 10.1023/A:1008398006403.

[38] J. W. Hutchinson. "Buckling of spherical shells revisited". In: *Proceedings of the Royal Society A: Mathematical, Physical and Engineering Sciences* 472.2195 (2016), p. 20160577. DOI: 10.1098/rspa.2016.0577.

[39] J. W. Hutchinson and W. T. Koiter. “Postbuckling theory”. In: *Applied Mechanics Reviews* 23 (1970), pp. 1353–1366.

[40] J. W. Hutchinson and J. M. T. Thompson. “Nonlinear buckling behaviour of spherical shells: barriers and symmetry-breaking dimples”. In: *Philosophical Transactions of the Royal Society A: Mathematical, Physical and Engineering Sciences* 375.2093 (2017), p. 20160154. DOI: 10.1098/rsta.2016.0154.

[41] J. W. Hutchinson and J. M. T. Thompson. “Nonlinear Buckling Interaction for Spherical Shells Subject to Pressure and Probing Forces”. In: *Journal of Applied Mechanics* 84.6 (Apr. 2017). DOI: 10.1115/1.4036355.

[42] *ISO, Kinematic diagrams – graphical symbols*. ISO 3952-1. 1981.

[43] R. M. Jones. *Buckling of Bars, Plates, and Shells*. Bull Ridge, Blacksburg, 2006.

[44] W. T. Koiter. “On the Stability of Elastic Equilibrium.” In: Amsterdam, Holland.: H. J. Paris, 1945. Chap. 8, pp. 201–213.

[45] T. Kreilos and T. M. Schneider. “Fully localized post-buckling states of cylindrical shells under axial compression”. In: *Proceedings of the Royal Society A: Mathematical, Physical and Engineering Sciences* 473.2205 (2017), p. 20170177. DOI: 10.1098/rspa.2017.0177.

[46] S. Kyriakides and P. K. Shaw. “Inelastic Buckling of Tubes Under Cyclic Bending.” In: *ASME. J. Pressure Vessel Technol.* 109.2 (1987), pp. 169–178. DOI: https://doi.org/10.1115/1.3264891.

[47] E.R. Lancaster, C.R. Calladine, and S.C. Palmer. “Paradoxical buckling behaviour of a thin cylindrical shell under axial compression”. In: *International Journal of Mechanical Sciences* 42.5 (2000), pp. 843–865. DOI: https://doi.org/10.1016/S0020-7403(99)00030-2.

[48] C. Leclerc and S. Pellegrino. “Nonlinear elastic buckling of ultra-thin coilable booms”. In: *International Journal of Solids and Structures* 203 (2020), pp. 46–56. DOI: https://doi.org/10.1016/j.ijsolstr.2020.06.042.

[49] C. Leclerc et al. “Characterization of Ultra-Thin Composite Triangular Rollable and Collapsible Booms”. In: *4th AIAA Spacecraft Structures Conference*. DOI: 10.2514/6.2017-0172.

[50] Christophe Leclerc. “Mechanics of Ultra-Thin Composite Coilable Structures”. PhD thesis. Caltech, 2020.

[51] A. Lee et al. “The Geometric Role of Precisely Engineered Imperfections on the Critical Buckling Load of Spherical Elastic Shells.” In: *Journal of Applied Mechanics* 83.11 (Sept. 2016). DOI: 10.1115/1.4034431.

[52] HMYC Mallikarachchi and Sergio Pellegrino. “Failure criterion for two-ply plain-weave CFRP laminates”. In: *Journal of Composite Materials* 47.11 (2013), pp. 1357–1375. DOI: 10.1177/0021998312447208.

[53] J. Marthelot et al. “Buckling of a Pressurized Hemispherical Shell Subjected to a Probing Force”. In: *Journal of Applied Mechanics* 84.12 (Oct. 2017). DOI: 10.1115/1.4038063.

[54] E. Medina et al. “Navigating the landscape of nonlinear mechanical metamaterials for advanced programmability”. In: *Phys. Rev. B* 101 (6 2020), p. 064101. DOI: 10.1103/PhysRevB.101.064101.

[55] J. M. Muñoz-Guijosa et al. “Simple Testing System for Pure Bending Tests with Large Deflections”. In: *Experimental Mechanics* 52 (2012), pp. 679–692. DOI: https://doi.org/10.1007/s11340-011-9535-7.

[56] T. W. Murphey, M. E. Peterson, and M. M. Grigoriev. “Large Strain Four-Point Bending of Thin Unidirectional Composites”. In: *Journal of Spacecraft and Rockets* 52.3 (2015), pp. 882–895. DOI: 10.2514/1.A32841.

[57] T.W. Murphey and J. Banik. “Triangular rollable and collapsible boom, U.S. Patent 7,895,79”. In: 2011.

[58] X. Ning. “Imperfection Insensitive Thin Shells”. PhD thesis. Caltech, 2015.

[59] X. Ning and S. Pellegrino. “Imperfection-insensitive axially loaded thin cylindrical shells”. In: *International Journal of Solids and Structures* (2015). DOI: https://doi.org/10.1016/j.ijsolstr.2014.12.030.

[60] X. Ning and S. Pellegrino. “Searching for imperfection insensitive externally pressurized near-spherical thin shells”. In: *Journal of the Mechanics and Physics of Solids* (2018). DOI: https://doi.org/10.1016/j.jmps.2018.06.008.

[61] A.B. Perduijn and S.M. Hoogenboom. “The pure bending of sheet”. In: *Journal of Materials Processing Technology* 51.1 (1995), pp. 274–295. DOI: https://doi.org/10.1016/0924-0136(94)01596-S.

[62] J. P. Peterson, P. Seide, and V. I. Weingarten. *Buckling of thin-walled circular cylinders. NASA Space Vehicle Design Criteria, NASA SP-8007. (Revised 1968).* Tech. rep. NASA, 1965.

[63] A. Pirrera, D. Avitabile, and P.M. Weaver. “Bistable plates for morphing structures: A refined analytical approach with high-order polynomials”. In: *International Journal of Solids and Structures* 47.25 (2010), pp. 3412–3425. ISSN: 0020-7683. DOI: https://doi.org/10.1016/j.ijsolstr.2010.08.019.

[64] E. Pollard and T. Murphey. “Development of Deployable Elastic Composite Shape Memory Alloy Reinforced (DECSMAR) Structures”. In: *47th AIAA/ASME/ASCE/AHS/ASC Structures, Structural Dynamics, and Materials Conference* (2006). DOI: 10.2514/6.2006-1681.

[65] M. Potier-Ferry. “Amplitude modulation, phase modulation and localization of buckle patterns”. In: *COLLAPSE: the buckling of structures in theory and practise (eds JMT Thompson, GW Hunt). Cambridge, UK: Cambridge University Press* (1983).

[66] T. Rahman and E.L. Jansen. “Finite element based coupled mode initial post-buckling analysis of a composite cylindrical shell”. In: *Thin-Walled Structures* 48.1 (2010), pp. 25–32. DOI: https://doi.org/10.1016/j.tws.2009.08.003.

[67] P. M. Reis. “A Perspective on the Revival of Structural (In)Stability With Novel Opportunities for Function: From Buckliphobia to Buckliphilia”. In: *Journal of Applied Mechanics* (2015). DOI: 10.1115/1.4031456.

[68] E. Riks. “An incremental approach to the solution of snapping and buckling problems”. In: *International Journal of Solids and Structures* 15.7 (1979), pp. 529–551. DOI: 10.1016/0020-7683(79)90081-7.

[69] F. Royer and S. Pellegrino. “Buckling of Ultralight Ladder-type Coilable Space Structures”. In: *AIAA Scitech 2020 Forum*. 2020. DOI: 10.2514/6.2020-1437.

[70] F. Royer and S. Pellegrino. “Buckling of Ultralight Ladder-type Coilable Space Structures”. In: *AIAA Scitech 2020 Forum*. DOI: 10.2514/6.2020-1437.

[71] F. Royer and S. Pellegrino. “Ultralight Ladder-type Coilable Space Structures”. In: *AIAA Spacecraft Structures Conference* (2018). DOI: 10.2514/6.2018-1200.

[72] K. A. Seffen and S. Pellegrino. “Deployment dynamics of tape springs”. In: *Proceedings of the Royal Society of London. Series A: Mathematical, Physical and Engineering Sciences* 455.1983 (1999), pp. 1003–1048. DOI: 10.1098/rspa.1999.0347.

[73] K. A. Seffen and S. Pellegrino. *Deployment of a rigid panel by tape-springs*. Technical Report CUED/D-STRUCT/TR168 Department of Engineering, University of Cambridge. 1997.

[74] J. Singer, J. Arbocz, and T. Weller. *Buckling Experiments: Experimental Methods in Buckling of Thin-Walled Structures: Vol. 1*. Wiley, New York, 2002.

[75] J. M. T. Thompson. “Advances in Shell Buckling: Theory and Experiments”. In: *International Journal of Bifurcation and Chaos* 25.01 (2015), p. 1530001. DOI: 10.1142/S0218127415300013.

[76] J. M. T. Thompson and G. H. M. van der Heijden. “Quantified "Shock-Sensitivity" Above the Maxwell Load”. In: *International Journal of Bifurcation and Chaos* 24.03 (2014), p. 1430009. DOI: 10.1142/S0218127414300092.

[77] J. M. T. Thompson, J. W. Hutchinson, and J. Sieber. "Probing Shells Against Buckling: A Nondestructive Technique for Laboratory Testing". In: *International Journal of Bifurcation and Chaos* 27.14 (2017), p. 1730048. DOI: 10.1142/S0218127417300488.

[78] J. M. T. Thompson, J. W. Hutchinson, and J. Sieber. "Probing Shells Against Buckling: A Nondestructive Technique for Laboratory Testing". In: *International Journal of Bifurcation and Chaos* 27.14 (2017), p. 1730048. DOI: 10.1142/S0218127417300488.

[79] J. M. T. Thompson and J. Sieber. "Shock-Sensitivity in Shell-Like Structures: With Simulations of Spherical Shell Buckling". In: *International Journal of Bifurcation and Chaos* 26.02 (2016), p. 1630003. DOI: 10.1142/S0218127416300032.

[80] J.M.T. Thompson and L.N. Virgin. "Spatial chaos and localization phenomena in nonlinear elasticity". In: *Physics Letters A* 126.8 (1988), pp. 491–496. DOI: https://doi.org/10.1016/0375-9601(88)90045-X.

[81] E. Virot et al. "Stability Landscape of Shell Buckling". In: *Phys. Rev. Lett.* 119 (22 Nov. 2017), p. 224101. DOI: 10.1103/PhysRevLett.119.224101.

[82] T. Von Karman and H. S. Tsien. "The Buckling of Thin Cylindrical Shells Under Axial Compression". In: *Journal of the Aeronautical Sciences* 8.8 (1941), pp. 303–312. DOI: 10.2514/8.10722.

[83] M. K. Wadee, G. W. Hunt, and A. I. M. Whiting. "Asymptotic and Rayleigh-Ritz routes to localized buckling solutions in an elastic instability problem". In: *Proceedings of the Royal Society of London. Series A: Mathematical, Physical and Engineering Sciences* 453.1965 (1997), pp. 2085–2107. DOI: 10.1098/rspa.1997.0112.

[84] L. Wilson, E. E. Gdoutos, and S. Pellegrino. "Tension-Stabilized Coiling of Isotropic Tape Springs". In: *International Journal of Solids and Structures* 188-189 (2020), pp. 103–117. DOI: https://doi.org/10.1016/j.ijsolstr.2019.09.010.

[85] K. K. Yadav et al. "A Nondestructive Technique for the Evaluation of Thin Cylindrical Shells' Axial Buckling Capacity". In: *Journal of Applied Mechanics* (2021). DOI: 10.1115/1.4049806.

[86] J.C.H. Yee and S. Pellegrino. "Folding of woven composite structures". In: *Composites Part A: Applied Science and Manufacturing* 36.2 (2005). 7th International Conference on the Deformation and Fracture of Composites (DFC-7), pp. 273–278. DOI: https://doi.org/10.1016/j.compositesa.2004.06.017.

[87] F. Yoshida, M. Urabe, and V.V. Toropov. "Identification of material parameters in constitutive model for sheet metals from cyclic bending tests". In: *International Journal of Mechanical Sciences* 40.2 (1998), pp. 237–249. DOI: https://doi.org/10.1016/S0020-7403(97)00052-0.

[88] A. Zareei, B. Deng, and K. Bertoldi. “Harnessing transition waves to realize deployable structures”. In: *Proceedings of the National Academy of Sciences* 117.8 (2020), pp. 4015–4020. ISSN: 0027-8424. DOI: 10.1073/pnas.1917887117.